Optimization of Non–Planar Wing Aircraft Configurations

Accounting for low speed mission segments

B.M. Verhagen

Delft University of Technology

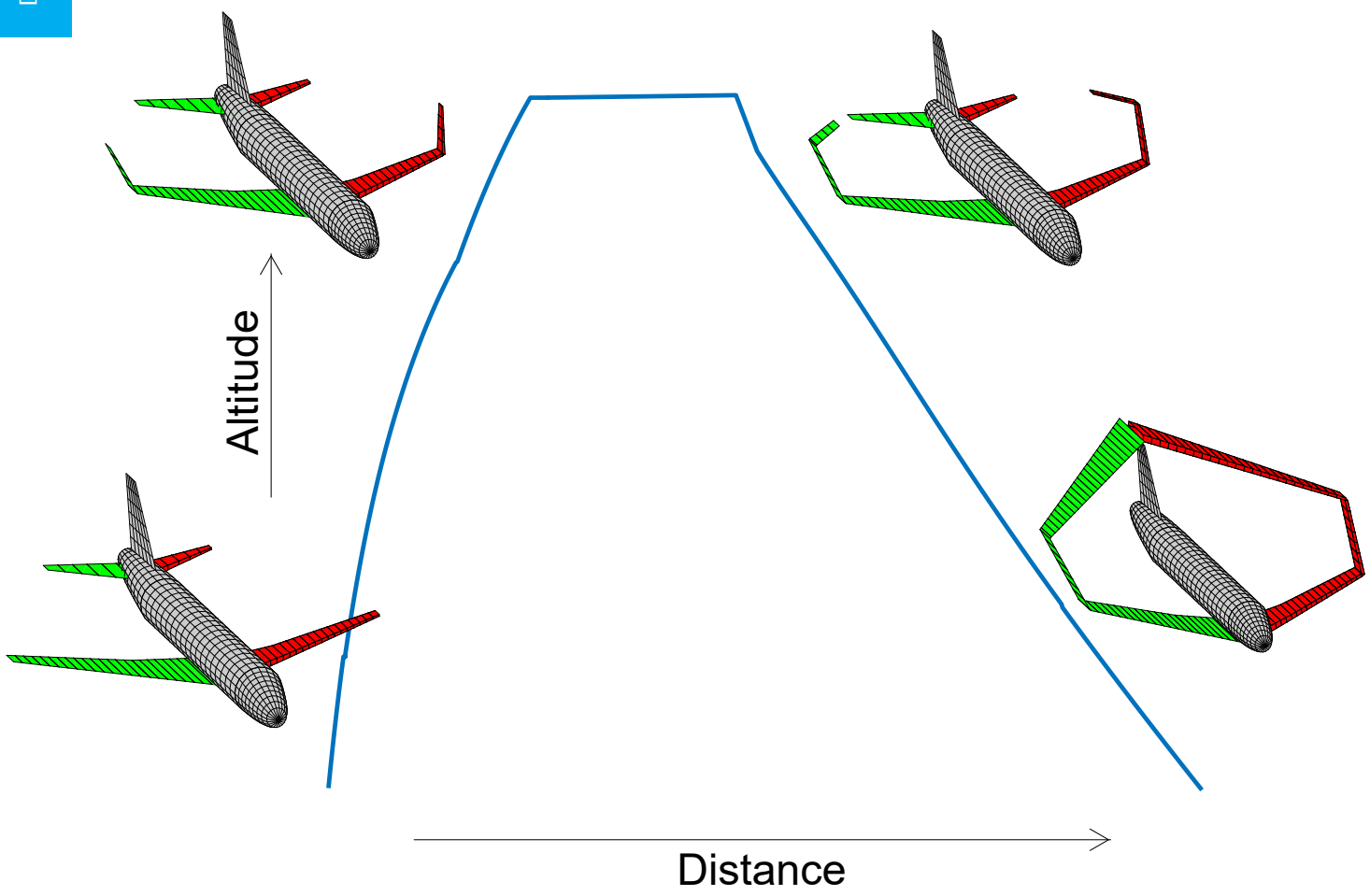

TU Delft Delft University of Technology

Challenge the future

Optimization of Non–Planar Wing Aircraft Configurations

Accounting for low speed mission segments

by

B.M. Verhagen

in partial fulfillment of the requirements for the degree of

Master of Science
in Aerospace Engineering

at the Delft University of Technology,
to be defended publicly on Tuesday March 28, 2017 at 10:30 AM.

Supervisor:	Prof. dr. ir. L. M. Veldhuis	
Thesis committee:	Dr. ir. M. Voskuijl,	TU Delft
	Dr. ir. H. G. Visser,	TU Delft
	Dr. ir. J. Vankan	NLR

This thesis is confidential and cannot be made public until March 28, 2017.
Thesis registration number: 151#17#*MT*#*FPP*

An electronic version of this thesis is available at http://repository.tudelft.nl/.

TU Delft Delft University of Technology

ABSTRACT

Air traffic is expected to double in the next two decades; as result global fuel consumption will increase as well. With increasing oil prices, fuel will have a more significant impact on the total aircraft operating costs. In addition, aircraft fuel consumption leads to an increase in greenhouse gases, such as carbon dioxide and nitrogen oxides. The International Air Transport Action Group has set a goal of achieving carbon-neutral growth in air travel by 2020, making aircraft fuel consumption an important topic. These economic pressures and environmental concerns demand a reduction in the fuel consumption.

Reducing the drag of an aircraft is one way to reduce the overall fuel consumption at given flight conditions and given aircraft weight. Non-planar wing aircraft configurations may offer a solution to reduce the drag while maintaining the performance of today's aircraft. Previous work on this subject was mainly focused on the optimization of the non-planar lifting surfaces, while the main wing remains unaffected. Further, the aerodynamic performance is often evaluated at cruise conditions. The aim of this study is to identify the effect of using different climb and descent strategies on the planform optimization of non-planar wing configurations in order to reduce overall fuel consumption, therefore reducing aircraft operating costs. In order to analyze these effects, a generic aero-structural aircraft model combined with a mission analysis model was developed to assess the aircrafts performance over an entire mission profile.

In the structural model that was developed, a Finite Element Method was applied to optimize the wing box structural thickness distribution in order to accomplish the minimum wing weight, that complies with the critical load conditions, as certified in CS25. The aerodynamic model combines a Vortex Lattice Method, with airfoil lift drag polars, to account for both the induced and parasitic drag. A mission model was created that simulates the climb and descent phases using two segments of constant equivalent airspeed and a segment of constant Mach number. The resulting block fuel, or block time, are used as an objective function within the optimization.

In this study, an Airbus A320 was used as baseline aircraft; the fuselage properties remain constant, and non-planar wing surfaces are retrofitted on this aircraft. Four types of aircraft configurations were considered: a planar configuration, a wing with winglet configuration, a C-wing configuration, and a box wing configuration. For each of the configurations types, the entire wing geometry is defined by the design variables. Using a gradient-based optimization method, the configurations were optimized for minimum fuel consumption over an entire mission profile. Two mission profiles were considered: a fuel economy mission profile, the mission that results in the minimum fuel consumption, and a minimum time mission profile, which results in the minimum block time. To clearly identify the effects of variation in the low speed mission segments, a short mission range of 600km was considered. In this short range mission, the climb and descent phases are a significant part of the total mission, so variations in these phases will have a larger effect on the optimal wing configurations.

In the fuel economy mission profile, the flight speeds in the climb and descent phases are lower compared to the speeds in the minimum time mission profile. Lower flight speeds result in higher induced drag in these phases. Therefore, the configurations optimized for the fuel economy mission profile utilize a higher aspect ratio wing, which results in an lower induced drag. On the other hand, the configurations optimized for the minimum time mission profile have higher sweep angles to reduce the wave drag, which becomes more significant at higher flight speeds.

The optimized wing with winglet and box wing configurations offer fuel reductions up to 2% with respect to the planar configuration, while the C-wing results in a higher fuel consumption. The non-planar configurations show a reduction in induced drag at the cost of higher parasitic drag. For the winglet and C-wing, the addition of the non-planar surfaces results in higher lift over drag ratios. The lift over drag ratio at cruise conditions of the box wing is slightly higher compared to that of the planar configuration, but is significantly lower in the low speed mission segments; however, the box wing offers a low wing mass compensating for the

poor aerodynamic performance and resulting in a lower fuel consumption. The opposite effect is true for the C-wing; it requires a heavier wing structure, which negates its better aerodynamic performance. Therefore, the C-wing results in a higher fuel consumption for the considered mission range. By increasing the mission range, the aerodynamic performance in the cruise phase becomes more important. Therefore the non-planar configurations become more fuel efficient with increasing mission length.

B.M. Verhagen
Delft, March 2017

ACKNOWLEDGEMENTS

This research has been performed at the Dutch Aerospace Center (NLR) to obtain my Master's degree in Aerospace Engineering at the Delft University of Technology. I would like to thank my supervisors, Mark Voskuijl (TU Delft) and Jos Vankan (NLR), for their guidance and support during this research project. I would also like to thank Huub Timmermans (NLR) for his support with Nastran. Furthermore, I would like to thank the other members of my committee, prof. dr. ir. Leo Veldhuis and dr. ir. Dries Visser for their time and effect in assessing this thesis. Finally, I would like to take this opportunity to thank my friends, my family, and especially my parents for their unconditional support during my entire study.

B.M. Verhagen
Delft, March 2017

CONTENTS

List of Figures

NOMENCLATURE

Acronyms

AoA	Angle of Attack
DoE	Design of Experiments
DSM	Design Structure Matrix
EAS	Equivalent Air Speed
FEM	Finite Element Method
MTOW	Maximum take-off weight

Greek Symbols

α	Angle of attack	$^\circ$
ϵ	Twist	deg
γ	Flight path angle	$^\circ$
κ_A	Korn Factor	-
λ	Taper ratio	-
ν	Poisson ratio	-
ρ	Density	kg/m^3
ρ_0	Density at sea level	kg/m^3
σ	Stress	MPa
σ_y	Yield stress	MPa

Roman Symbols

b	Wing span	-
c	Chord length	m
c_f	Local friction coefficient	-
$c_{d,friction}$	Airfoil friction drag coefficient	-
$c_{d,wave}$	Airfoil wave drag coefficient	-
c_{d_0}	Airfoil interpolation constant	-
c_{d_1}	Airfoil interpolation constant	-
c_{d_2}	Airfoil interpolation constant	-
c_d	Airfoil drag coefficient	-

c_l	Airfoil lift coefficient	-
e	Oswald factor	-
f	Fuel flow	kg/s
h	Altitude	m
m	Mass	kg
n_{max}	Critical load factor	-
q	Dynamic Pressure	Pa
t/c	Thickness over chord ratio	-
Γ	Throttle setting	-
A	Aspect ratio	-
C_D	Drag coefficient	-
C_f	Friction coefficient	-
C_L	Lift coefficient	-
C_r	Root chord	m
$C_{D_{fus}}$	Fuselage group drag coefficient	-
$C_{D_{h-tail}}$	Horizontal tail drag coefficient	-
$C_{D_{ind}}$	Induced drag coefficient	-
C_{D_p}	Profile drag coefficient	-
$C_{D_{wing}}$	Wing drag coefficient	-
$C_{L_{h-tail}}$	Horizontal tail lift coefficient	-
$C_{L_{wing}}$	Wing lift coefficient	-
D	Drag	N
D_f	Friction drag	N
E	E-modulus	MPa
FF	Fuel fraction	-
K_{acc}	Accuracy factor for the mission analysis	-
L	Lift	N
M	Mach number	–
M	Mach number	-
M_{cr}	Critical Mach number	-
M_{DD}	Drag divergence Mach number	-
M_{MO}	Maximum operating Mach number	-
PS	Power Setting	–
R	Gas constant of air	J/(kg K)

Re	Reynolds number	-
S	Wing reference area	m^2
S_{wetted}	Wetted wing area	m^2
S_{xy}	Reference area in the xy plane	m^2
SFC	Specific Fuel Consumption	$kg/(Ns)$
T	Temperature	K
T	Thrust	N
V	Velocity	m/s
V_{MO}	Maximum operating speed	m/s
$W_{blockfuel}$	Block fuel weight	N
W_{fuel}	Fuel weight	N
$W_{fuselage}$	Fuselage weight	N
W_{fus}	Fuselage group weight	N
W_{PL}	Payload weight	N
W_{TO}	Take-off weight	N

1

INTRODUCTION

Air traffic is expected to grow over the next few decades [1]; as result global fuel consumption will increase as well. With increasing oil prices [2], fuel will have a more significant impact on the total aircraft operating costs. In addition, aircraft fuel consumption leads to an increase in greenhouse gases, such as carbon dioxide and nitrogen oxides. The International Air Transport Action Group has set a goal of achieving carbon-neutral growth in air travel by 2020 [3], making aircraft fuel consumption an important topic. These economic pressures and environmental concerns demand a reduction in the fuel consumption.

Reducing the drag of an aircraft is one way to reduce the overall fuel consumption at given flight conditions and given aircraft weight. Unconventional configurations may be a solution to reduce the drag while maintaining the performance of today's aircraft. These unconventional aircraft configurations include blended-wing-bodies, truss-braced wing aircraft, and non-planar wing configurations. This study focuses on the non-planar wing configurations.

Previous work conducted on the optimization of non-planar wing configurations has limitations: most studies mainly focused on the optimization of the non-planar surfaces, while the main wing design remains unchanged. Additionally in these studies the aerodynamic performance has often only been evaluated at cruise conditions. Furthermore, with such a variety of research objectives requiring multitudes of specific models it can be difficult to gain insight in the multidisciplinary design choices of these non-planar configurations. This study aims to develop a generic model, with which every arbitrary non-planar wing configurations can be evaluated based on its aero-structural performance over an entire mission profile. The aerodynamic and structural models generated aim to model real aircraft behaviour. The next section describes the research objective of this study. Section 1.2 states the scope of the study and describes the main differences between this study and previous work on this subject.

1.1. RESEARCH OBJECTIVE

In spite of previous studies on non-planar wing configurations, there is still no definite consensus on which wing configurations are optimal in terms for fuel consumption [4] [5], as will be expanded upon in chapter 2. Most studies thus far have focused on minimizing the total drag at one specific flight condition. Recent studies by Jansen et al. [6] have made use of single point optimization at cruise conditions and have used the Breguet range equation to determine the required fuel for the entire mission [4]. The use of single point optimization at cruise conditions might result in inaccurate prediction of total aircraft fuel consumption. The constant L/D, SFC, and flight speed in the Breguet range equation are simplifications that do not reflect an actual aircraft mission, since their values vary during the mission [7]. Single-point optimization has the tendency to produce designs with optimal performance under the selected flight condition at the expense of performance degradation under off-design conditions [7]. Also, this inaccuracy is expected to grow for shorter missions, as the non-cruise segments become a more significant part of the entire mission.

Accurate calculations of the mission performance and fuel consumption estimation require more realistic

modelling of an aircraft mission [8], which can be achieved by dividing the mission profile into multiple segments. The fuel consumption at each segment can then be determined by numerically solving the equations of motion for symmetric flight [9].

In the non-cruise flight conditions (climb and descent), a significant part of the total mission fuel can be consumed, especially for short-range missions. In these take-off and final approach conditions, the induced drag typically accounts for 80-90% of the total drag [10]. However, in the second climb phase, the parasitic drag contributes to a larger percentage of the total drag compared to the cruise conditions due to the lower lift coefficient.

The recent study by Skinner et al. [5] indicated that the optimal configuration strongly depends on the relative importance of the parasitic drag w.r.t. the induced drag. Because the ratio between the drag components depends on the flight condition, optimizing for different flight conditions can result in different optimal designs. Therefore single point optimization may not result in the optimal configuration in terms of fuel consumption when an entire mission is considered. As Jansen et al. suggested, it would be interesting to optimize over the full mission profile [4], since any changes in the aircraft performance at these low speed conditions can drastically influence the whole design [11].

Thus, The main research question remains:

How does a full mission analysis affect the most fuel-efficient design of non-planar wing aircraft configurations considering the low fidelity aero-structural optimization during the preliminary design phase?

The following sub-questions have been formulated to address this question:

1. What is the effect of varying the climb and descent strategies on the most fuel efficient non-planar wing planform configurations?
2. What is the effect of the addition of non-planar wing surfaces on the fuel consumption considering a full mission analysis?
3. What is the effect of varying the cruise length and cruise Mach number on the fuel efficiency of the optimized non-planar wing configurations?

1.2. RESEARCH SCOPE

Although a full mission analysis is performed in this study, the focus lies on the climb and descent segments. The effect of different climb and descent profiles on the most optimal wing configurations is analyzed. In order to do this, mission profiles are optimized for the minimum block fuel or minimum block time, resulting in the fuel economy mission profile and the minimum time mission profile respectively. For these resulting mission profiles, the four different aircraft configurations are optimized.

The project goal is to perform a mission based planform optimization of non-planar wing configurations in order to obtain the highest fuel-efficiency. In the proposed study, the entire design space from planar wings, winglets, C-wings, and box wing configurations is considered. The aero-structural performance is evaluated at multiple points along the mission profile to determine actual fuel flow at each point. Integrating the fuel flow over the mission profile results in the total block fuel.

The goal of this proposed research is not to design a complete aircraft, as this requires a specific and complete design study. Altering the wing configuration may have a significant impact on the entire aircraft configuration, which is considered outside the scope of this study. Instead, the goal is to explore the multi-disciplinary considerations in the design of non-planar wing configurations and to show the importance of including the non-cruise phases in the optimization of non-planar wing aircraft configurations.

The main differences between this study and previous work on non-planar wing aircraft configurations include:

- The climb and descent phases are taken into account in the mission analysis.

- A detailed structural model is developed, in which the thickness distribution of the wing box is optimized for the minimum weight at the critical load condition, as defined in the CS25 regulations [12]. Previous studies used the root bending moment or equivalent beam model to estimate the wing weight [13, 14].
- The induced drag, parasitic drag, and wave drag components are taken into account . Previous studies often neglected the effect of the wave drag [14]. However, at cruise conditions, this may be a significant contribution to the total drag.
- The effect of the flight condition of the optimized non-planar wing configuration is analyzed. The aero-structural performance is evaluated at different flight conditions. Previous studies only considered the aero-structural performance at the cruise conditions [6, 13].
- The static longitudinal stability and controllability are taken into account. Altering the wing planform may also require changes to the horizontal stabilizer. By constraining the static margin, the static longitudinal stability of the aircraft is ensured.
- A mission based optimization is performed with the objective to minimize the block fuel. Most previous studies had the objective to minimize the total drag [13, 14]. Jansen et al. [6] studied maximizing the mission range of a non-planar wing configurations.

1.3. REPORT OUTLINE

This report is structured as follows: Chapter 2 provides an extensive overview of the background of non-planar wing configurations. The fundamentals of drag are discussed, followed by the physics behind non-planar wing configurations. In addition, previous studies on this subject are discussed and the models used in their studies are assessed. Also, an analysis of the fuel consumption in the low-speed mission segments is given for the A320, which is used as baseline aircraft in this study, to provide insight on the importance of these segments. Chapter 3 provides a detailed overview of the developed model. The assumptions are stated and a schematic overview of the various modules is provided, followed by a detailed discussion of these modules. Chapter 4 discusses the optimization set-up. In this chapter, the non-planar configurations being considered in this study are discussed. Also, the optimization settings, including the design variables, bounds, and objective functions are discussed in this chapter. Chapter 5 presents the results of this study. The effect of the cost factor on the mission profile using a fixed wing planform is discussed. This is followed by a discussion of the optimized non-planar wing planforms. Lastly, the effect of the cruise characteristics on the efficiency of the non-planar wing configurations is analyzed. Chapter 6 provides the conclusions from this research. In chapter 7 recommendations for further research on this subject are presented.

2

BACKGROUND

This chapter presents the required background knowledge for the research performed on the non-planar wing configurations. The first section describes the fundamentals of drag. Sections 2.2 to 2.4 describe the physics behind non-planar wing configurations and how they are used to reduce the induced drag. Section 2.5 gives a brief overview of the previous research on non-planar wing configurations. Finally, section 2.6 analyzes the fuel consumption in the non-cruise phases of a typical flight, which is used to support the main purpose of this thesis as will be clarified in the next chapter.

2.1. FUNDAMENTALS OF DRAG

The aircraft drag typically consist of two components: the parasitic drag and the induced drag. The parasitic drag can be divided in the friction drag, interference drag, and the wave drag as can be seen in figure 2.1.

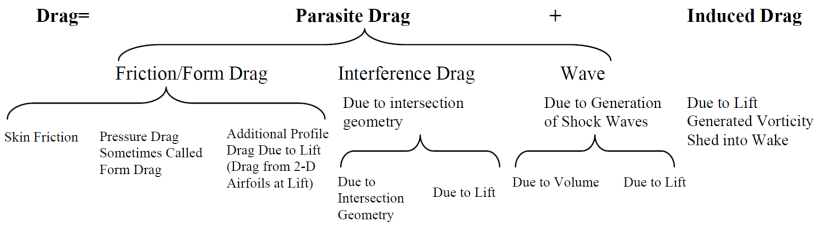

Figure 2.1: Components of drag [15]

The total drag can be written in dimensional form as shown in equation 2.1. The first term relates to the parasitic drag component and the second term relates to the induced drag component.

$$D = qSC_{D_p} + \frac{L^2}{q\pi b^2 e} \tag{2.1}$$

With

$$q = \frac{1}{2}\rho V^2 \tag{2.2}$$

Where C_{D_p} is the dimensionless parasitic drag coefficient, q is the dynamic pressure, S is the wing reference area, b is the wing span, L is the lift, and e is the Oswald factor. As can be seen from equations 2.1 and 2.2, the drag components are dependent on the flight speed. At low speeds the induced drag is dominant, while at high speeds the friction drag is dominant. This effect is illustrated in figure 2.2. At cruise conditions of commercial aircraft, the induced drag accounts for a large fraction (typically about 40%) of the total drag [10]. At take-off and climb conditions, the induced drag plays a even more important role. At these conditions, the induced drag typically account for 80% to 90% of the total drag [10].

The drag can be written in dimensionless form as follows:

$$C_D = C_{D_p} + \frac{C_L^2}{\pi A e} \tag{2.3}$$

Where C_{D_p} is the parasitic drag coefficient, C_L is the lift coefficient, and A is the wing aspect ratio.

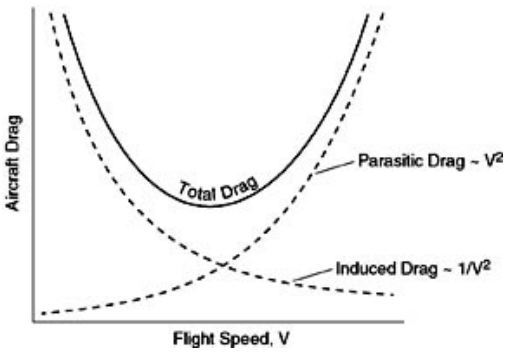

Figure 2.2: Components of drag as function of flight speed [16]

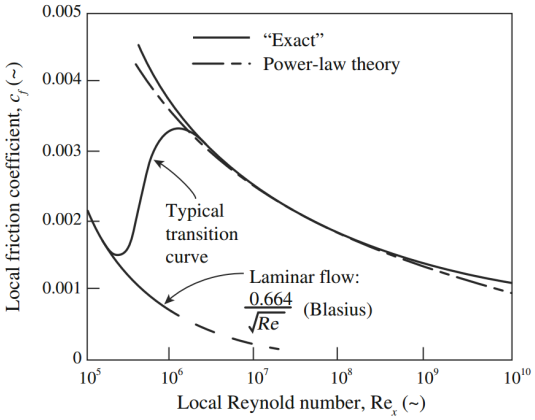

Figure 2.3: local friction coefficient as function of Reynolds number [17]

The parasitic drag is the sum of friction drag and pressure drag. For wings with an attached flow, friction drag is the most significant. Friction drag is the result of friction between the air molecules and the wing surfaces. Due to the viscosity of air, molecules that flow past the wing surface generate frictional forces. The molecules just above the wing surface are slowed down due to these frictional forces. By moving further away from the surface, less air is slowed down. The result is a thin layer of air near the wing surface in which the velocity changes from zero at the surface to the free stream value away from the surface. This layer is called the boundary layer.

The friction drag is dependent on the characteristics of the boundary layer. A turbulent boundary layer has a higher friction coefficient than a laminar boundary layer because more shear stress is generated at the surface. The friction coefficient of an airfoil can be determined using equation 2.4, where c_f is the local friction coefficient and c is the chord length. The local friction coefficient is a function of the Reynolds number [17]. Increasing the Reynolds number decreases the friction drag coefficient as shown in figure 2.3. The values in this figure correspond to the flow over a flat plate [17]. The friction drag can then be determined using equation 2.5. This equation shows that the friction drag of the wing is proportional to its wetted area.

$$C_f = \frac{1}{c}\int_0^c c_f dx \tag{2.4}$$

$$D_f = C_f q S_{wetted} \tag{2.5}$$

Induced drag arises due to pressure differences between the upper and lower surface of a wing. Due to the pressure differences, tip vortices induce a downwash over the wing. This effect is illustrated in figure 2.4. The downwash adds a vertical component to the free stream flow, which reduces the effective angle of attack of the wing. Since the lift of a wing acts perpendicular to the free stream flow, the lift vector is tilted backwards which induces a drag component as can be seen in figure 2.5.

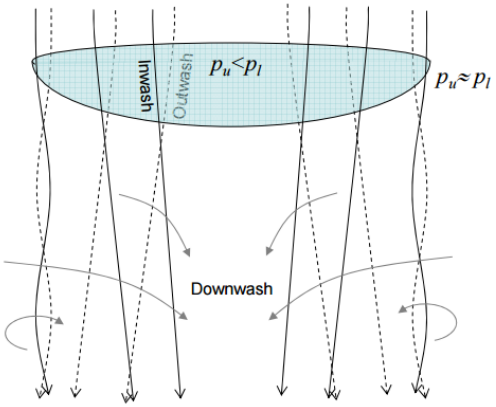

Figure 2.4: Illustration of the downwash created by tip vortices [18]

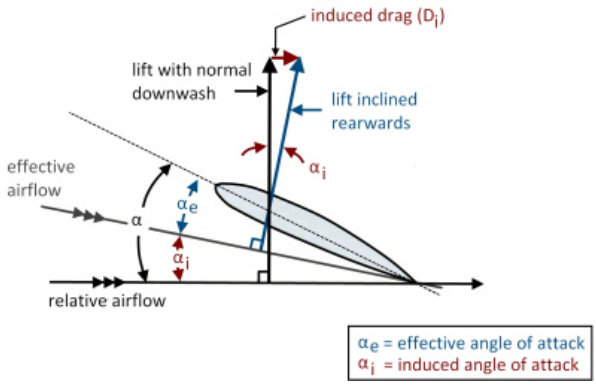

Figure 2.5: Change in free stream flow direction due to induced downwash on the wing [19]

2.2. INDUCED DRAG REDUCTION CONCEPTS

The efficiency of the wing in terms of induced drag, is often referred to as the span efficiency factor of the wing. The span efficiency indicates the variation of drag with lift. Munk concluded in 1921 [20] that the minimum induced drag is obtained if the downwash distribution is constant in the far wake field [11]. For planar wings, this condition is obtained at an elliptical lift distribution over the wing span. In this case the span efficiency factor has its maximum value of unity for planar wings.

According to equation 2.3, the induced drag can be reduced by increasing the aspect ratio or by increasing the span efficiency factor. A 10% increase in wing span can lead to 17% reduction in induced drag [11]. However the wing span is often constraint due to structural reasons. By increasing the span, the center of lift moves away from the root which increases the bending moments and thus the wing weight. Also due to airport requirements and aeroelastic effects such as an early flutter onset, increasing the wing span is not always a feasible option.

As mentioned before, a planar wing has a maximum span efficiency of unity. For non-planar configurations this factor can be increased, which could reduce the induced drag significantly compared to planar wings. Kroo [10, 11, 21] studied the effect of non-planar configurations on the induced drag extensively. Figure 2.6 shows possible configurations with their corresponding optimal span efficiency at a height over span ratio h/b of 0.2. Some of these concepts make use of end-plates or winglets, while other configurations have an increased aspect ratio for the individual wings by distributing the wing into multiple wings with equal span and the same total area [22]. Examples of this latter configurations include the biplanes. The closed box wing configuration has the highest theoretical span efficiency factor. This configuration originates from Prandtl's best wing system, as will be discussed in more detail in the next section. Figure 2.7 shows the effect of increasing the height over span ratio h/b. This allows for even higher span efficiencies due to reduced interference effects between the lifting surfaces [10].

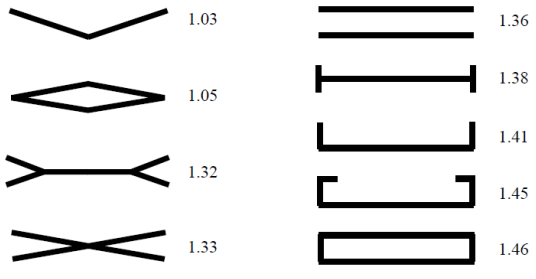

Figure 2.6: Nonplanar configurations with their span efficiency at h/b = 0.2 [11]

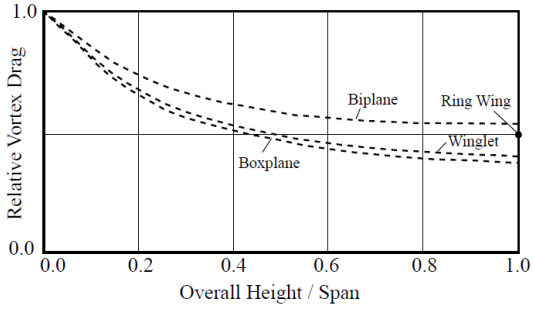

Figure 2.7: Effect of h/b ratio on the induced drag for nonplanar concepts [11]

2.3. PRANDTL'S BEST WING SYSTEM

The best wing system idea was presented in 1924 by Prandtl [23]. He studied the effect of induced drag on biplanes and triplanes. When the two wings have an equal span, the induced drag is reduced to a minimum [23]. The addition of end plates allows for a further reduction of the induced drag. He proposed a configuration where the tips of the biplane wings are connected, forming a closed box wing configuration as shown in figure 2.8.

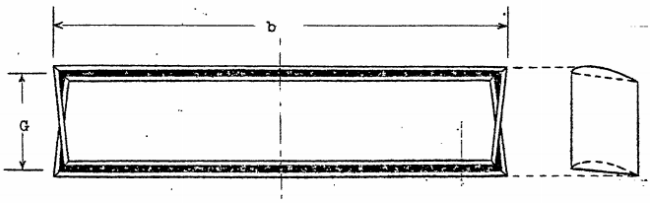

Figure 2.8: Prandtl's best wing system [23]

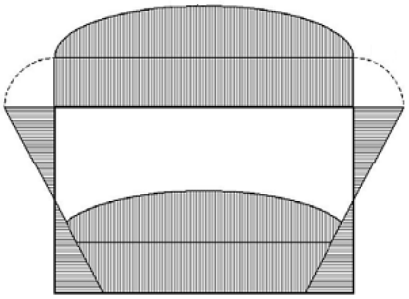

Figure 2.9: Best wing system optimal lift distribution. [24]

The best wing system has an identical lift distribution on each of the horizontal wings and a 'butterfly' shaped lift distribution on the vertical wing tips. The lift goes to zero at the center of the vertical wing tips [23]. This lift distribution is shown in figure 2.9. At these conditions the induced velocities are constant along the span, resulting in the minimum induced drag.

Munk studied how the interference drag on each surface varied as the longitudinal separation between the lifting surfaces was changed [20]. He found that if the circulation of each lifting surface remains constant, the total induced drag of the system remains unchanged. So the induced drag is independent of the longitudinal position of the lifting surfaces as long as the total circulation for each surface remains constant. This effect is known as Munk's stagger theorem [11]. By applying Munk's stagger theorem, it can be shown that stagger and sweep of the lifting surfaces does not affect the induced drag of the system if the lift distribution remains unchanged, see figure 2.10.

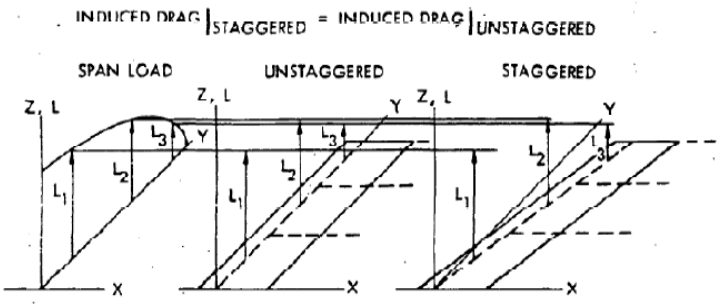

Figure 2.10: Application of Munk's stagger theorem [25]

2.4. PHYSICS OF NON-PLANAR CONFIGURATIONS

Gall [25] described the physical effect of placing an end-plate at the wing tip. In order to describe these effects, the following cases are analyzed:

- The induced drag by the wing itself
- The induced drag by the wing on the end plate
- The induced drag by the winglet itself

- The induced drag by the winglet on the wing

Figure 2.11 (a) shows the induced flows of the wing itself. Due to the pressure differences between the top and bottom of the wing, vortices originate at the wing tip that induce a downwash component w_w over the wing. This changes the direction of the free stream, which results in an aft tilted resultant vector F. This vector can be decomposed in the lift vector L and the induced drag D_i.

Figure 2.11 (b) shows the induced drag of the wing on the winglet. The vortices at the wing tips induce a cross flow v_w over the winglet. This changes the direction of the free stream, which results in resultant force F to be tilted forward. This vector can be decomposed into an inward force *S.F.* and an induced drag component D_i. Because the induced drag vector D_i is pointing forward, this drag component is actually a small thrust force.

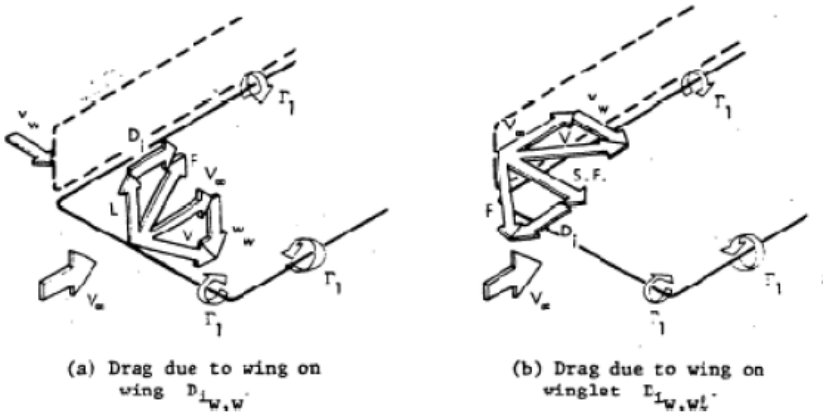

Figure 2.11: Induced drag due to the wing [25]

Figure 2.12 (c) shows the induced drag of the winglet itself. This effect is similar to the one depicted in figure 2.11 (a). The vortices created by the winglet induce a outward crossflow v_{wl} on itself. This results in an outward pointing freestream vector, resulting in the induced drag component D_i as shown in the figure.

Finally, figure 2.12 (d) shows the induced drag of the winglet on the wing. The vortex created at the 'root' side of the winglet induces a upwash on the wing w_{wl}. This rotates the resultant force acting on the wing forward. This effect also creates a small thrust force.

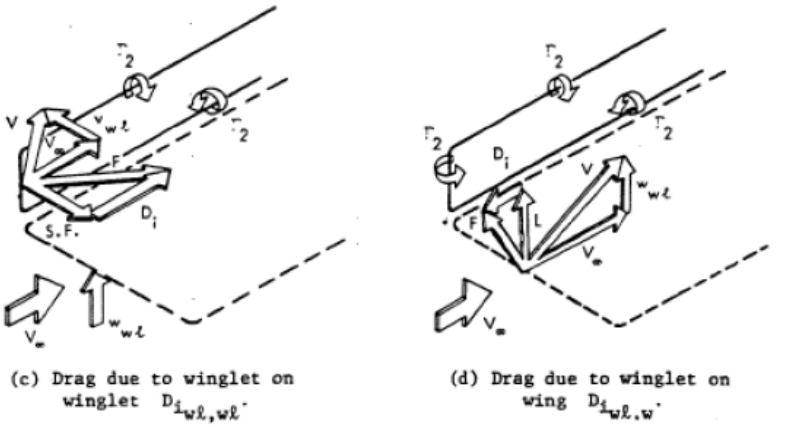

Figure 2.12: Induced drag due to the winglet [25]

The minimum induced drag of the system is obtained if the resultant sidewash on the winglet equals zero.

This is the case if the effects as described in figures 2.11 (b) and 2.12 (c) cancel each other. In this case, only a inward pointing force *S.F.* is acting on the winglet. On the wing, a part of the downwash w_w is cancelled by the upwash generated by the winglet w_{wl}. Therefore the resulting vector will be pointed less aft, reducing the induced drag. These effects are summarized in figure 2.13.

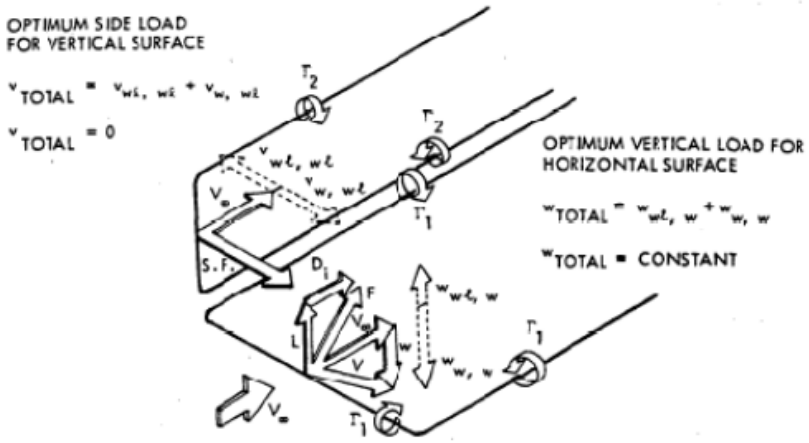

Figure 2.13: Combined induced drag effects on a wing-winglet configuration [25]

Prandtl's best wing system consists of two 'wing-winglet' configurations placed on top of each other. As described in section 2.3, the lift goes to zero at the point where the winglets meet. The optimal lift distribution of the box wing is obtained if both the horizontal wings carry the same amount of lift [23], as shown in figure 2.14 (f). Kroo [10] stated that a fixed circulation can be added to the system without changing the lift and induced drag. In this case, the lower wing carries all the required lift and the upper wing carries no or even negative lift. This makes the inner part of the upper surface redundant and it can be removed. This results in the C-wing geometry as shown in figure 2.14 (c)-(e). By removing the inner part of the upper wing, the wetted area is significantly reduced. Therefore the parasitic drag component of this configuration is expected to be lower compared to the box wing configuration. However, the span efficiency of a C-wing approximates the box wing value as shown in the figure.

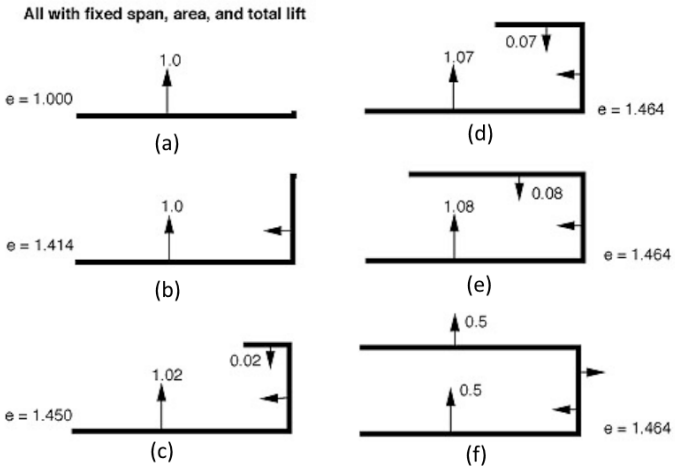

Figure 2.14: Optimal load distribution on non-planar wing configurations [10]

2.5. PREVIOUS OPTIMIZATION STUDIES ON NON-PLANAR WING CONFIGURATIONS

This section assesses the recent research performed on non-planar wing configurations. In addition, the differences of the most relevant studies are schematically summarized to provide a clear overview. The following studies are considered to provide background information on non-planar configuartions and to outline various factors that come into play when optimizing non-planar wing configurations:

- Drag characteristics for Optimally Span-Loaded Planar, Wingletted, and C Wings (2009) [13]
- Tip Extensions, Winglets, and C-wings: Conceptual Design and Optimization (2010) [14]
- Aerostructural Optimization of Nonplanar Lifting Surfaces (2010) [26]
- Aerodynamic Design Optimisation on Non-planar Lifting Surfaces (2016) [5]

2.5.1. ASSESSMENT OF PREVIOUS OPTIMIZATION STUDIES

The optimization studies under consideration have different goals for which different methods and constraints are applied to perform trade-off studies. This sections summarizes and compares the main differences in each study. Each study is assessed based on goals, models, constraints, design freedom, and optimization methods used. Assessment criteria are discussed. Results and conclusions from these studies contributed towards the creation of a model to support the current research.

GOAL OF STUDIES

Verstraeten et al [13] optimized the spanwise wing loading under fixed lift and root bending moment (RBM) constraints for a given winglet height and C-wing horizontal length. In addition, they performed linear optimization using Lagrange multipliers to trade-off the effect of winglet height and C-wing length. Ning et al. [14] demonstrated the importance of comparing wing weights at their critical load conditions. They used a more representative method to determine the wing weight. They compared the differences in induced drag for a fixed wetted area and fixed wing weight at various ratios of manoeuvre lift coefficient w.r.t. cruise lift coefficient $C_{L_{manoeuvre}}/C_{L_{cruise}}$. Jansen et al [26] performed aerostructural optimizations, in which the optimizer is given as much as freedom as possible. They took the aerostructural deflections into account to determine the aerodynamic performance and the structural wing weight. Finally, they used an equivalent beam model approach to explore the effect of structural sizing on the non-planar configurations.

STRUCTURAL MODELS

The structural models used in the reviewed studies vary from one another. However, the computational cost of all the methods is low which is a requirement for the preliminary optimization. Most studies, especially the more dated ones, use the Root Bending Moment (RBM) as measure for the structural wing weight. Ning et al. [14] concluded that the RBM as means of structural weight determination provides inappropriate results. The RBM method does not account for the effect of chordwise changes in the planform on the bending moment. Especially for non-planar configurations, the RBM method can result in inaccurate results since the moment arm of the non-planar surfaces can be very small, resulting in negligible or even negative bending moment contribution. Therefore they proposed adding the area-dependent weight to the load-depending weight model. This solution provides a better approximation of the wing weight. Jansen et al [26] modelled the structure of the wing using an equivalent beam finite element approach. This method provides an adequate approximation of the stiffness and deflection behaviour of a real wing.

AERODYNAMIC ANALYSIS

Since the main purpose of non-planar configurations is to reduce the induced drag, this effect is studied most. Many of the preliminary studies examined the effect of various non-planar concepts on the induced drag component, while ignoring parasitic drag despite the fact that the addition of non-planar surfaces can significantly increase the parasitic drag. Therefore, the most recent optimization studies also take this drag

component into account. At high subsonic and transonic flight conditions, the compressibility drag also becomes more important. Jansen et al. [26] included this drag component in his study, while Verstraeten et al. [13] and Ning et al. [14] neglected this effect or considered low subsonic conditions where the effect is less significant.

The methods used to determine parasitic and induced drag are comparable amongst the more recent studies. These studies use different programs to determine the induced drag component. However, the programs used are all based on the same principle: a VLM method is used in which the induced drag is calculated at the Trefftz plane. Also, the parasitic drag is calculated similarly. The section drag coefficient is assumed to depend on the section lift coefficient according to a parabolic variation. Jansen et al. [26] included the effect of variation in the Reynolds number to determine the sections drag coefficient. This is important since a lower chord length results in a lower Reynolds number, which increases the sectional drag coefficient. Finally, the sectional drag coefficient is interpolated in spanwise direction to obtain the parasitic drag coefficient for the complete wing.

OPTIMIZATION METHODS

The preliminary studies were often based on wind tunnel measurements and analytical solutions. In these studies, a 'one at a time' approach is used to determine the effect of various parameters. Verstraten et al. [13] and Ning et al. [14] used quadratic programming problems combined with Lagrange multipliers to study the effects of changing a selection of design parameters. These methods are well suited to perform trade studies where only a limited amount of geometric parameters is varied. However, in order to perform a full optimization study with a higher number of design variables, a nonlinear optimization method is necessary. Ning et al. used a gradient based optimization method to optimize a winglet. Jansen studied a wider range of non-planar concepts, ranging from planar wings to box wings. This design space contains a lot of local minima. Therefore a gradient based optimizer was not feasible and a particle swarm optimization method was used. All the reviewed studies performed the aerodynamic trade-off studies and optimization problems at a single flight condition, which is often a point in the cruise phase of a mission.

CONSTRAINTS

Most studies used constraints for the trade studies and optimization problems of non-planar tip devices. The most common used, are the RBM, fixed lift, or fixed wetted area constraints. These are simple methods which can be used during the preliminary trade-off studies. However, to perform a full optimization problem, the aerostrucutral coupling has to be taken into account where the lift and weight comply with the equations of motion for the considered flight condition.

DESIGN FREEDOM

Finally, the design freedom varies for the reviewed studies. Verstraeten et al. [13] only varied the winglet height and C-wing length. Ning et al. [14] allowed the optimizer to vary the winglet geometry with high freedom, but maintained a fixed main wing planform. Jansen et al. [26] gave the optimizer as much freedom as possible to design a wing within a defined design space using up to four surfaces.

2.5.2. PARASITIC VS INDUCED DRAG

As discussed above, the question if a configuration can result in a total drag reduction depends on the models used and assumptions made to determine the parasitic and induced drag components. Since there is no conclusive answer to this question, Skinner et al. [5] performed multi-objective optimizations of various non-planar wing configurations. For each configuration they determined the increment in parasitic drag and the reduction in induced drag. This resulted in the formation of the Pareto fronts for tip-extension, winglet, and highly non-planar configurations. A non-planar configuration can results in a total drag reduction if the reduction in induced drag can outweigh the increase in parasitic drag.

Figure 2.15 shows the resulting Pareto fronts under various RBM and span constraints for the winglet configurations. In addition to the winglet, the outer 25% of the wing is also taken into account for the optimization. The configurations explored by Skinner are depicted in figure 2.16. By moving along the Pareto

front form (c) to (a), it shows that the dihedral angle of the winglet decreases and the sweep increases. From these images, it also becomes apparent that a heavier structure (larger RBM) allows for a larger induced drag reduction at the expense of an increasing parasitic drag component.

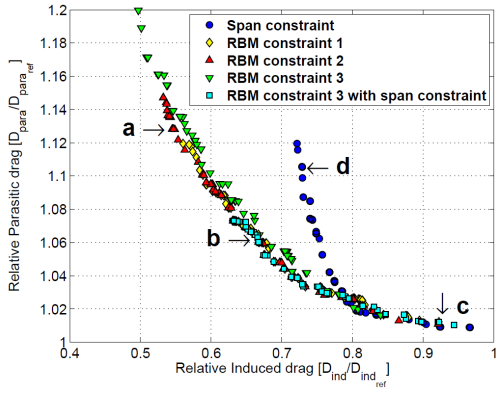

Figure 2.15: Pareto front of winglet configuration optimization [5]

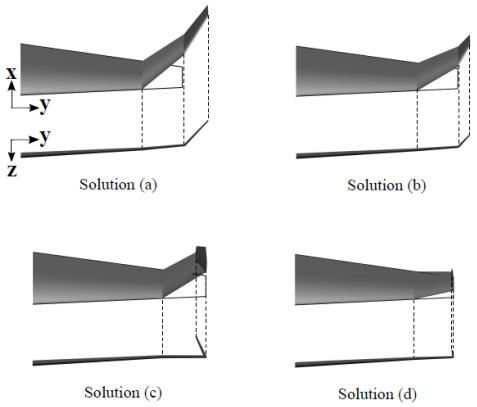

Figure 2.16: Winglet configurations as indicated in the Pareto front [5]

Figure 2.17 shows the Pareto front under span constraints for highly non-planar configurations. The configurations as indicated by the characters coincidence with the configurations shown in figure 2.18. The resulting Pareto front is approximately linear. The closed configurations show a large reduction in induced drag, while the parasitic drag is significantly increased. Both the horizontal lifting surfaces provide a positive and similar portion of the total lift. This is in agreement with Prandtl's best wing system as presented in section 2.1. The horizontal surface of the C-wing provides a negative lifting force. This is in agreement with Kroo's description of the C-wing configurations as discussed in section 2.1.

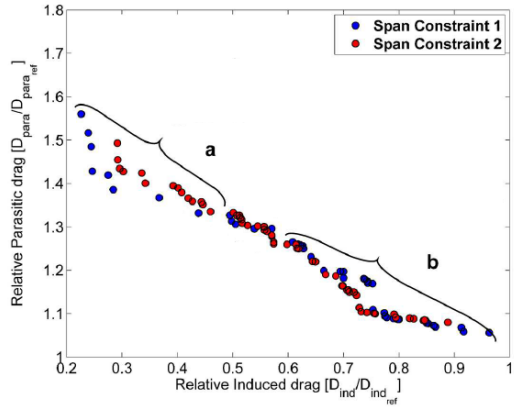

Figure 2.17: Pareto front of the highly non-planar wing configuration optimization [5]

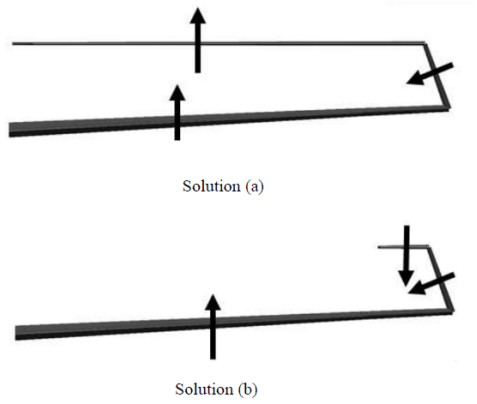

Figure 2.18: Highly non-planar configurations as indicated in the Pareto front [5]

Since both drag components have a unequal contribution to the total drag, the question if the reduction in induced drag can outweigh the increment in parasitic drag, depends on the 'relative importance' of the two drag components. According to equation 2.1, the induced drag increases with increasing lift coefficient and decreasing velocity. According to Kroo, during climb the induced drag can take up to 80% of the total drag; while in cruise conditions, the induced drag is typically around 40% of the total drag. Since the ratio between the drag components differs with flight condition, the configuration with the lowest total drag also depends on the considered flight condition.

Because the fuel consumption strongly depends on the total drag, the fuel consumption during the different flight phases of an A320 is analyzed in section 2.6. The fuel consumed during the climb, cruise, and descent phases was determined for mission ranges of 500km to 2000km. According to these results, the fuel consumed in the non-cruise phases can be a significant fraction of the total fuel consumed, especially for short range missions. Because the optimal configuration depends on the ratio between the drag components and differs significantly in the non-cruise phases, it is important to take the non-cruise flight conditions into account when a configuration is optimized for the minimum required block fuel.

2.5.3. SCHEMATIC OVERVIEW

Table 2.1 gives a schematic overview of the differences in relevant research literature as previously discussed. The comparison is based on the drag components used in the aerodynamic analysis, structural weight estimation methods, the optimization methods used, the considered configurations, and the leven of design freedom.

Table 2.1: Used models and assumptions for the most relevant reviewed studies

		Verstraeten	**Ning**	**Jansen**	**Skinner**
Aero.	Induced drag	X	X	X	X
	Viscous drag	X	X	X	X
	Compressibility drag			X	
Structural	Root bending moment	X			X
	RBM + area dependency		X		
	Equivalent beam model			X	
	Aeroelastic deformations			X	
	Cruise condition	X	X	X	X
	Manoeuvre condition		X	X	
Opt.	Linear trade-off study	X	X		
	Non-linear optimization study		X	X	X
Des. space	Tip extension	X	X	X	X
	Winglet	X	X	X	X
	C-wing	X		X	X
	Box wing			X	X
Des. Freedom	Fixed planform with:				
	- Limited freedom of tip device geometry	X			
	- High freedom of tip device geometry		X		X
	High freedom planform with:				
	- High freedom of tip device geometry			X	

2.6. ANALYSIS OF THE FUEL CONSUMPTION IN THE NON-CRUISE PHASES

As mentioned in the previous section, the minimum drag configuration depends on the ratio between the drag components. This ratio changes according to climb, descent, and cruise conditions and can have a significant impact on the block fuel: the required fuel amount to perform a mission. In this section, the amount of fuel used during these non-cruise phases is determined as fraction of the total block fuel.

For this purpose, the software tool Piano-X [27] was used to analyze the mission of an A320-214 aircraft. Figure 2.19 shows a typical mission profile for a Airbus A320-214 with a range of 1000 km. Figure 2.20 shows the cumulative fuel consumption over this mission profile. By differentiating this fuel consumption w.r.t the time, the fuel flow is obtained as shown in figure 2.21. It can be seen that the fuel consumed during take-off and climb constitutes a significant portion of the total fuel consumption for a 1000km mission.

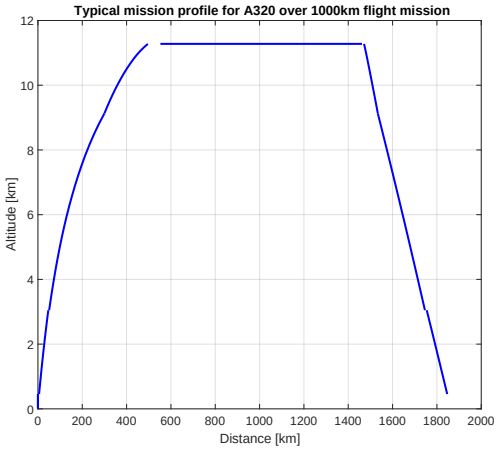

Figure 2.19: 500NM mission profile for the A320-214

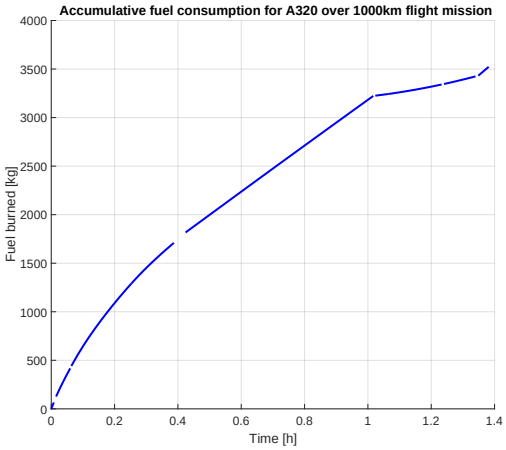

Figure 2.20: Accumulative fuel consumption for the A320-214

Figure 2.22 shows the relative fuel consumption of the A320 carrying the same payload of 4000kg for different mission ranges. According to this figure the fuel consumption in climb and descent phases can be more than half of the total fuel consumption for short range missions. Because the ratio of the drag components can be radically different at these non-cruise conditions, it is important to take these phases into account when optimizing a configuration for minimum block fuel.

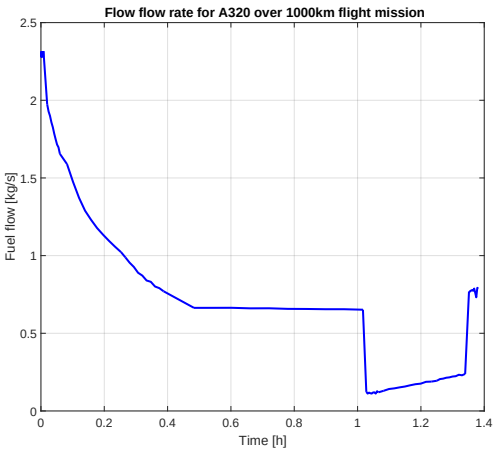

Figure 2.21: Fuel flow of the A320-214 during the 500NM mission

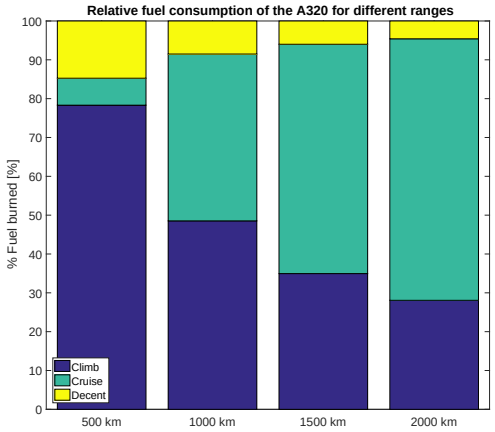

Figure 2.22: Relative fuel consumption for the flight phases for different ranges

3

MODEL

In order to determine the effects of the climb and descent segments of a mission on the non-planar wing configurations, a generic model has been developed that allows for the evaluation arbitrary wing configurations. This model consists of a structural module, an aerodynamic module, a mission module, a stability module, and a propulsion module. Figure 3.1 shows a step-by-step diagram of how the model was created. First, for each module the required meshes and analysis tools were created. Subsequently, the optimal number of discretization steps has been determined where necessary. After all the modules were created and validated, a Design of Experiments (DoE) and sensitivity analysis have been performed as preparation for the design optimization studies.

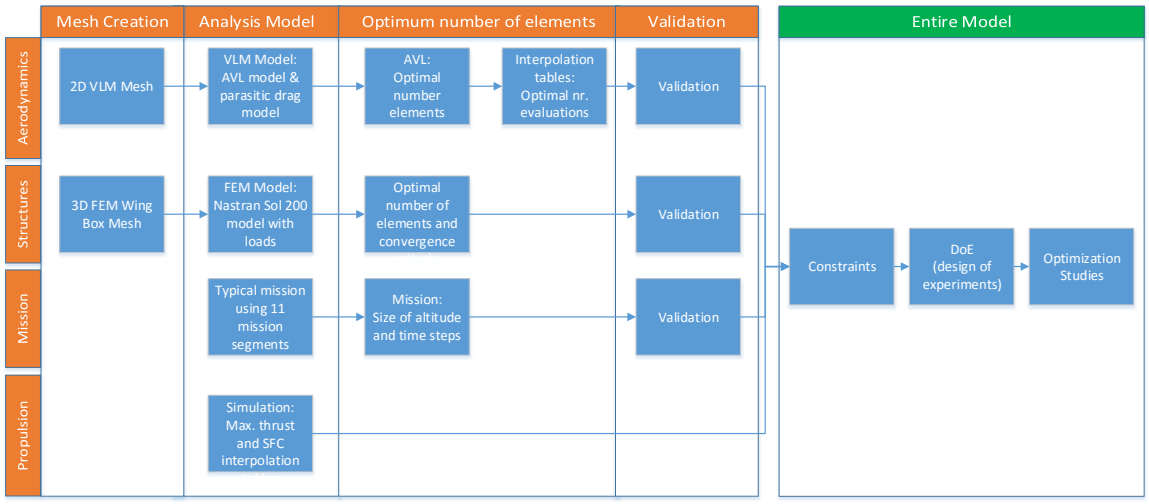

Figure 3.1: Step-by-step diagram of the model creation process

This chapter is structured as follows: section 3.1 states the main assumptions and their effects. Section 3.2 presents a schematic overview of the program flow between the various modules. Section 3.3 describes the baseline A320 model with its properties. Section 3.4 describes the wing parametrization. Finally, sections 3.5 and 3.6 describe each of the modules in more detail. All the presented figures in this section refer to the evaluation of the reference A320-200 wing.

3.1. ASSUMPTIONS

The main assumptions made in the model are:

- **Only symmetric flight is considered.**
  The mission model considers only symmetric flight. In reality an aircraft will perform lateral manoeuvres, e.g. turns. Especially in the initial climb and final approach phase these lateral manoeuvres may be performed. Also, no gusts or tail wind is taken into account.
- **Only longitudinal stability.**
  As a consequence of the previous assumption, only longitudinal stability and control is considered.
- **Fuselage group properties are assumed to remain constant.**
  The non-planar wing configurations will be retro fitted on the conventional A320. This implies that the fuselage group properties, fuselage group weight, fuselage group drag, and weight distribution remain constant.
- **15% fuel is stored in the tail tanks.**
  For configurations with a tail (planar, winglet, and C-wing) 15% of the fuel is assumed to be stored in the tail.
- **Aeroelastic effects are neglected**
  In this study, the aeroelastic effects are neglected. In reality the wing will deform under the aerodynamic loads resulting in an upward bending. This will affect the lift distribution and thus the aerodynamic properties of the aircraft. In the present study the wing is assumed to remain in its rig shape.
- **The maximum operating speed and Mach number (V_{MO}/M_{MO}) remains constant.**
  When the effect of the cost factor is analyzed, the optimizer is allowed to vary the climb speeds of the aircraft. Stall constrains the lower bound of the speed. The upper bound of the speed range is constrained by the maximum operating speed. This speed may be affected by changing the wing planform. However, in this study the V_{MO} and M_{MO} are assumed to remain constant.
- **Same engine location as percentage of span.**
  The engines used in this study are the CFM56-5B, which are most common used on the A320 aircraft. The optimal location of the engines can vary with changing the wing geometry. In this study the spanwise location of the engines, as percentage of the span, is assumed to remain constant.
- **Fuselage has no effect in aerodynamic analysis**
  The fuselage group is assumed to have no effect on the aerodynamic properties of the aircraft. Only the constant fuselage drag area ($C_D \cdot S$) is accounted for. Also, in the aerodynamic (VLM) model, the fuselage is not modelled. Therefore it will not effect the lift distribution of the wings. However, experimental studies on wing-body configurations (with different values of span and fuselage width) have demonstrated that the fuselage generates a lift contribution about the same as the contribution lost by the part of the wing masked by the fuselage [28].
- **Fuel fractions used below 1500ft remain constant**
  The fuel burned during the initial and final mission segments from engine warm-up up to 1500ft, and from 1500ft to engine shutdown are determined using the fuel fractions method. In section 3.3.4 is explained how these fuel fractions are determined. Changing the wing geometry will affect these fuel fractions. However, in this study these fractions are assumed to remain constant.
- **Manufacturing constraints for the wing box are not taken into account**
  Section 3.6 presents the structural model of the wingbox. A FEM model is used in which the thickness of each of the wingbox segments is optimized to the minimum weight. This may result in a irregular thickness distribution, which is not practical due to manufacturing reasons. However, there are no constraints on irregular thicknesses. Only a minimum thickness for the skin and booms is accounted for as will be explained in section 3.6.3.
- **Constant payload**
  The payload in the presented study remains constant and equal to the design payload of the conventional A320 reference aircraft.

3.2. SCHEMATIC OVERVIEW OF THE ANALYSIS

Figure 3.2 shows a basic overview of the connection between the various modules used for this study. For a given wing parametrization, aerodynamic and structural meshes are created. Using theses meshes, the wing weight of the corresponding configuration is determined in the structural module. In the aerodynamics module, an aero map is created, which determines the lift and drag coefficients as function of angle of attack and Mach number. These results, in combination with engine interpolation tables, are required by the mission analysis. Finally, the design is checked for stability, controllability and stall speed. Around this entire model, an optimization is applied which minimizes a given objective function.

The most important input and output variables of each module are shown in figure 3.2. Each of the blocks indicated in the figure will be discussed in more detail in the remaining sections of this chapter.

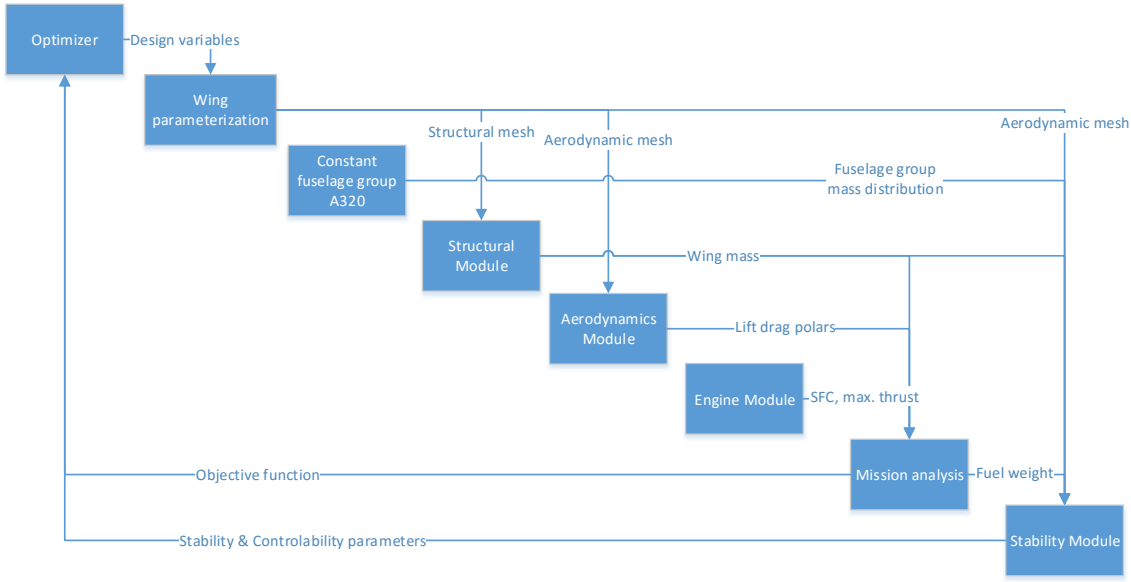

Figure 3.2: Design Structure Matrix of the coupling between the various modules

3.3. BASELINE MODEL - A320

In order to perform the proposed research, a baseline aircraft has to be selected which is suitable for the proposed research. This baseline aircraft is used to determine the weight and drag contribution of the fuselage group. In addition, the weight distribution of this baseline aircraft is used in the stability and controllability module of the presented model to ensure controllability and stability of the optimized configurations.

The aircraft selected as baseline for the proposed optimization study is the Airbus A320-200. It has a design range of 2700 NM [29], however most flights are considerably shorter [30]. Figure 3.3 shows the frequency as function of flight distance for all A320 family aircraft in the US national airspace in one day [30]. It can be seen that most flights are in the 200NM to 1200NM range. As concluded in chapter 2.6, the fuel consumption during the climb and descent phases is a significant fraction of the total fuel consumption for these short range flights. Therefore, the A320 provides a suitable baseline and reference to study the effects of including these non-cruise performance aspects. In addition, the A320 is one of the most widely used aircraft.

Section 3.3.1 provides the main characteristics of the A320-200. Section 3.3.2 discusses how the fuselage weight and drag components, which are held constant in this study, are determined. Section 3.3.3 discusses weight and longitudinal location of the various aircraft components, which is required by the stability module. Finally, section 3.3.4 discusses the fuel consumption in the landing-takeoff (LTO) segments.

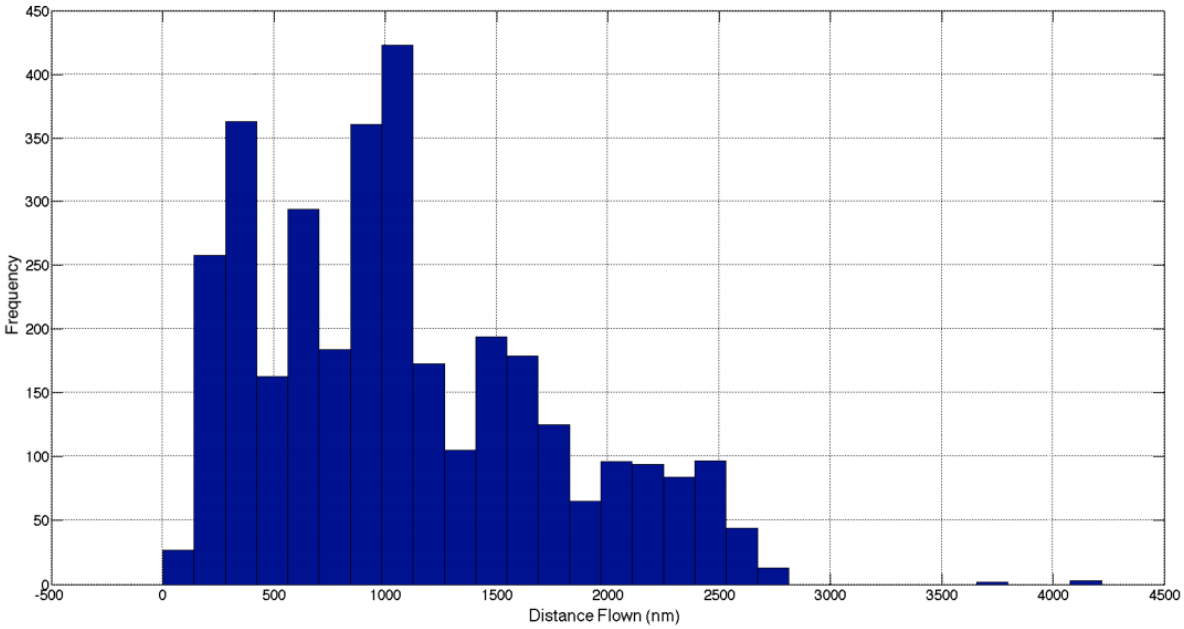

Figure 3.3: Frequency of mission length of the A320 in US airspace [30].

3.3.1. CHARACTERISTICS OF THE A320

The most important weight, planform, and flight condition characteristics of the A320 are shown in table 3.1 [29, 31]. These characteristics will be used to determine the fuselage group properties as discussed below. In addition, the values are used for validation purposes.

Table 3.1: Main characteristics of the A320

Weights		
Max. take-off	73500	$[kg]$
Zero-fuel	60500	$[kg]$
Engine (CFM56-5B) dry weight [32]	2500	$[kg]$
Wing Planform		
Area	122.40	$[m^2]$
Span	33.91	$[m]$
MAC	4.29	$[m]$
Aspect Ratio	9.39	$[-]$
Taper Ratio	0.24	$[-]$
1/4 Chord Sweep	25.00	$[°]$
Typical cruise conditions		
Speed	448	$[kts]$
Mach	0.78	[-]
Altitude	37000	$[ft]$
Fuel consumption	2100	$[kg/h]$
Design range	2700	$[NM]$
L/D_{cruise}	16.00	$[-]$
Maximum operating conditions		
V_{MO}	350	$[kts]$
M_{MO}	0.82	[-]

3.3.2. DETERMINATION OF THE FUSELAGE GROUP PROPERTIES

The fuselage group is defined as the complete aircraft minus its lifting surfaces, i.e. the aircraft minus the wing and horizontal stabilizer, and engines, nacelles, and control surfaces. In this study, the fuselage properties are determined at the beginning of the optimization process and their values are assumed to remain constant. The advantage of this approach is that it does not require the analysis of the entire aircraft as result on changes in the wing configuration.

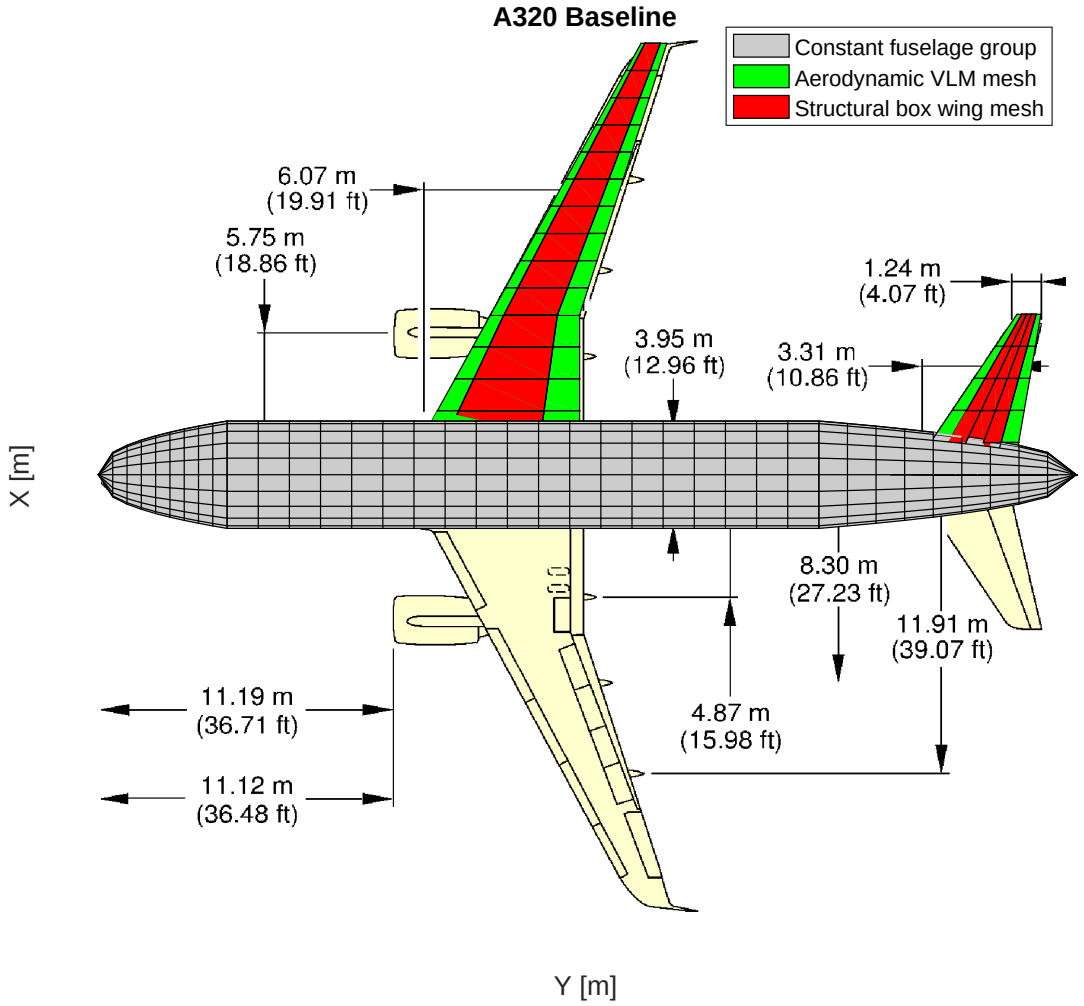

Figure 3.4: Reference A320 with illustration of the corresponding aerodynamic and structural meshes as used in this study [33]

The weight of the fuselage group can be determined using equation 3.1. The wing weight of the reference A320 will be determined with the structural module at its critical load conditions. The fuel weight can be determined using the mission analysis module. In this method, the resulting fuselage group weight is assumed to be constant during the optimization.

$$W_{fus} = W_{MTOW_{ref}} - W_{fuel_{des}} - W_{wing_{ref}} - W_{PL,des} \tag{3.1}$$

The drag of the fuselage group $C_{D_{fus}}$ can be determined using the aerodynamic module at cruise conditions to determine the lift and drag coefficients for the lifting surfaces. Using equation 3.2, the drag coefficient of the fuselage group can be determined.

$$\left(\frac{C_L}{C_D}\right)_{ref} = \frac{C_{L_{wing}} + C_{L_{h-tail}}}{C_{D_{wing}} + C_{D_{h-tail}} + C_{D_{fus}}} \tag{3.2}$$

Where $\left(\frac{C_L}{C_D}\right)_{ref}$ is assumed to be 16.0 at cruise conditions [31]. The lift and drag coefficient of the tail and horizontal stabilizer are determined by evaluating the reference A320 with the program presented in this section.

By rewriting equation 3.2, the fuselage group drag coefficient can be determined. Because the reference area of the to be analyzed wing configrations can vary significantly, the drag area $C_{D_{fus}} \cdot S_{ref}$ is assumed to be constant.

3.3.3. WEIGHT DISTRIBUTION

The weight distribution of the aircraft is required to determine the static stability and controllability of the aircraft, as will be discussed in more detail in section 4.3. For each subgroup within the fuselage group, the weight is determined using the Torenbeek relations [34]. The longitudinal position of each subgroup is determined based on the Airbus A320 Aircraft Characteristics Airport and Maintenance Planning document [33]. Table 3.2 presents these weights with their corresponding longitudinal location of the A320. The location of the components in the fuselage group are assumed to remain constant in the optimization studies. The location of the components in the wing group are varied within the model. In addition, the weight of the wing and horizontal tail are computed by the model for the analyzed wing configuration.

Table 3.2: A320 weight distribution

	Weight [kg]	**Longitudinal position [m]**
Fuselage group		
Vertical tail	473	23.3
Fuselage	7231	15.0
Alighting gear group	3108	5.1
APU	254	36.0
Instruments and navigational equipment	1103	4.0
Triplex system	869	16.5
Electric group	1212	16.5
Furnishing	4435	17.0
Air conditioning	974	16.5
Operational items	2135	18.8
Miscellaneous	398	16.0
Wing group		
Wing group	9981	16.9
Propulsion group (CFM56)	6402	12.9
Nacelle group	737	16.0
Surface control group	1164	18.8
Horizontal tail	713	33.7

3.3.4. FUEL FRACTIONS LTO SEGMENTS MISSION

To determine the fuel consumption in the initial (departure) phase and final (arrival) phases under 1500ft of the mission, fuel fractions have been used. These fuel fractions (FF) are defined as:

$$FF_i = \frac{W_{final_i}}{W_{initial_i}} \tag{3.3}$$

Where $W_{initial_i}$ relates to the mass of the aircraft at the start of the i^{th} mission segment, and W_{final_i} relates to the mass of at the end of the same mission segment. Torenbeek provides fuel fractions for commercial transport jets, see table 3.3 [34].

Table 3.3: Fuel fractions of transport jets according to Torenbeek [34]

	Fuel fraction [-]
Engine start and warm up	0.99
Taxi	0.99
Take-off	0.995
Climb and acceleration to cruise	0.98
Descent	0.99
Landing taxi and shutdown	0.992

However, in order to be more accurate, the fuel fraction of the A320 has been determined using Eurocontrol's data [35]. Based on the default ICAO taxi-out/in time, the fuel consumption in the taxi and take off, and approach and landing phases is determined [35]. These numbers are summarized in table 3.4. The initial start mass of 73500 kg is the MTOW of the A320. The 'mission end' mass of 57354 kg, as indicated in the table, is determined by summing the operational empty weight, the design payload, and 10% of the design fuel mass to account for the reserve fuel. The fuel consumption in the LTO segments is obtained from the EUROCONTROL document. Using this data, a more accurate fuel fraction prediction for the initial and final phases of the flight is made. This results in fuel fractions of 0.992 and 0.996 for the initial and final phases of the mission respectively. These fractions are assumed to remain constant in this study. The fuel consumption for the remaining parts of the mission, climb from 1500ft to descend to 1500ft, are determined using a more detailed mission analysis, as will be discussed in more detail in section 3.8.

Table 3.4: Fuel fractions of the A320 based on Eurocontrol data

	Fuel consumed [kg]	**Mass [kg]**	**Fuel fraction [-]**
Mission start		73500	
Taxi-out	237.1		
Take-off	95.1		
Climb out	246.8		
Climb - 1500 ft		72921	0.992
Climb to cruise	-	-	
Cruise	-	-	
Decent to 1500ft	-	-	
Descend - 1500ft		57591	
Approach and landing	149.76		
Taxi-in	87.36		
Mission end		57354	0.996

3.4. WING PARAMETRIZATION

In order to model a wing geometry, a model is created in which different trapezoidal wing segments are placed after each other, in which the wing tip coincidences with the root of the consecutive wing segment [26]. Each wing segment is parametrized by 6 variables: its length, taper, leading edge sweep, dihedral, twist at the begin and end of each segment. In addition, the root chord and the longitudinal position of the first wing segment are variable. Using this parametrization, each a high variety wing geometry can be created. Also, the number of lifting surfaces is variable. In this study, two lifting surfaces will be used: one for the wing and one for the horizontal stabilizer.

Figures 3.5a and 3.5b show the top and front view of a planar wing configurations and box wing configurations respectively. The dihedral of each segment is defined w.r.t. the global x-y plane, while the twist is

defined in the local axis system of each segment.

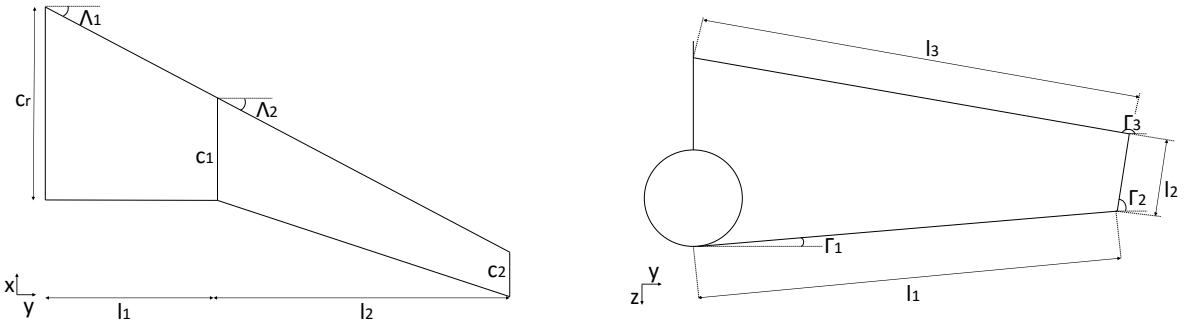

(a) Top view of a planar configuration

(b) Front view of a box wing configuration

Figure 3.5: Wing parametrization

3.4.1. WING REFERENCE VALUES

In addition to the wing parametrization as described in the previous section, some reference values are defined within the model. The reference area of the aircraft is defined as the sum of the area of each segment projected in the x-y plane:

$$S_{ref} = 2 \cdot \sum_{i=1}^{n_{seg}} S_{xy_i} \tag{3.4}$$

The mean aerodynamic chord (MAC) is defined as the area weighted average of the MAC of each segments, see equation 3.5.

$$MAC = \frac{2}{S_{ref}} \sum_{i=1}^{n_{seg}} S_{xy_i} \cdot MAC_i \tag{3.5}$$

Where the MAC of a trapezoidal wing segments is given by equation 3.6. In this equation C_r and λ refer to the root chord and taper ratio of the wing segment respectively.

$$MAC_i = \frac{2C_r(1+\lambda+\lambda^2)}{3(1+\lambda)} \tag{3.6}$$

3.4.2. MESH CREATION

Within the model, an aerodynamic and structural mesh are created. The meshes are created by dividing each wing segment in a number of elements in the chordwise, spanwise, and thickness direction. To ensure a continuous distribution of elements between the different wing segments, the number of elements in the chordwise and thickness direction are equal for each of the wing segments. To find the optimal number of elements, a mesh convergence test has been performed, as will be discussed in more detail in sections 3.5.3 and 3.6.4 for the aerodynamic and structural mesh respectively. Note that in the remainder of this report, a wing segment refers to a part of the wing as defined by its span, sweep etc., while a wing element refers to a mesh element within a wing segment.

The structural model consists of a wing box that is meshed in a number of elements in the chordwise N_c, spanwise N_b, and thickness N_v direction. The wing box is modelled as a trapezoidal cross section that is fitted in the airfoil between given chordwise percentages. In this study the width of the wing box is ranging from 15% to 75% of the local chord length, see figure 3.4 [33]. As will be discussed in section 3.5, two different airfoils are used in this study, a super-critical RAE2822 airfoil and a symmetrical NACA0012 airfoil.

The wing box is modelled using an upper skin, lower skin, front spar, and aft spar. In addition, four booms are added in the corners of the wing box, which carry the normal stresses [36], see 3.6a. Figure 3.6b shows a isometric view of how the wing box is positioned in the wing.

Ribs are not included in this model. The main purpose of the ribs is to resist torsional loads and to stiffen the skin against buckling [36]. Since a linear static Nastran analysis will be used, bucking cannot be modelled accurately. Instead of including the ribs in the structural mesh, their weight is accounted for using an empirical relationship as will be discussed in more detail in section 3.6.

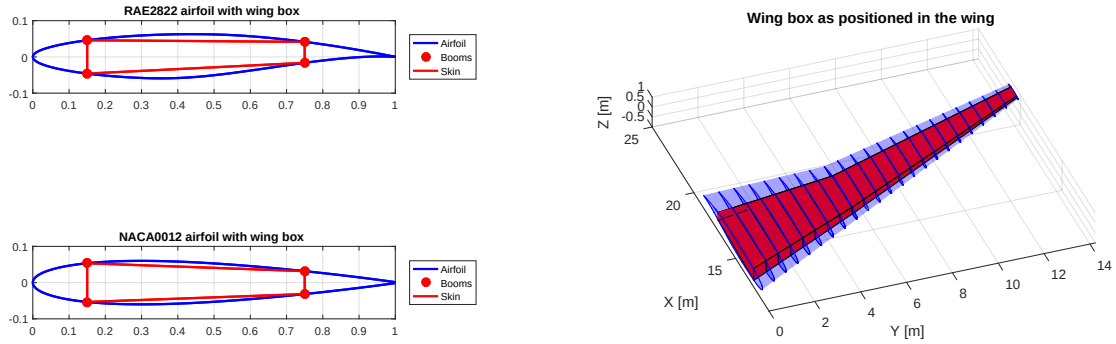

(a) Cross section view of the wingbox in the airfoil

(b) Isometric view of the wing box in the wing

Figure 3.6: Structural wingbox as positioned in the wing

The different wing segments are than attached to each other to form the mesh of the entire wing. The structural model consists of 3D wing box elements that are hinged about the center line in case of a change in dihedral, while the aerodynamic model consists of 2D elements. Therefore small coupling elements are added in the aerodynamic model to remain consistent with the structural model, see figure 3.7.

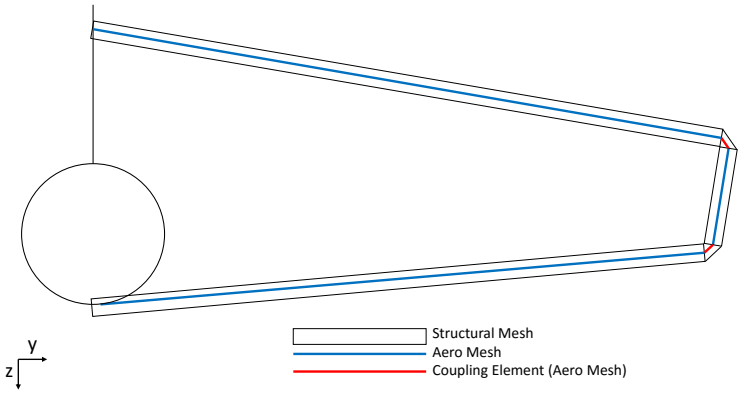

Figure 3.7: Coupling elements in the aerodynamic mesh

3.5. AERODYNAMICS MODULE

This section presents the aerodynamic model, which is evaluated for each analyzed aircraft configuration. As discussed in section 2.5, it is important to include both the induced drag and the parasitic drag components.

Figure 3.8 shows the flowchart of the aerodynamics module. The inputs of this module are the aerodynamic mesh, and the AVL mesh. Using this mesh, AVL analyses are performed for a series of angles of attack (AoA) and a series of Mach numbers. Because the total number of AVL runs is quite significant, running

these analysis subsequently may result in high computation times. Therefore these AVL runs are performed as background processes, which allows them to run parallel. The results of these analyses are stored in the AVL output files as indicated in the flowchart. Once all the runs are completed, for each combination of Mach number and AoA the sectional lift coefficient distribution, the 3D lift coefficient, and the induced drag coefficient are obtained and post-processed to include the parasitic drag. This results in a lift coefficient C_L and drag coefficient C_D as function of the Mach number and AoA of the aircraft:

$$C_L = f(AoA, Mach) \tag{3.7}$$

$$C_D = f(AoA, Mach) \tag{3.8}$$

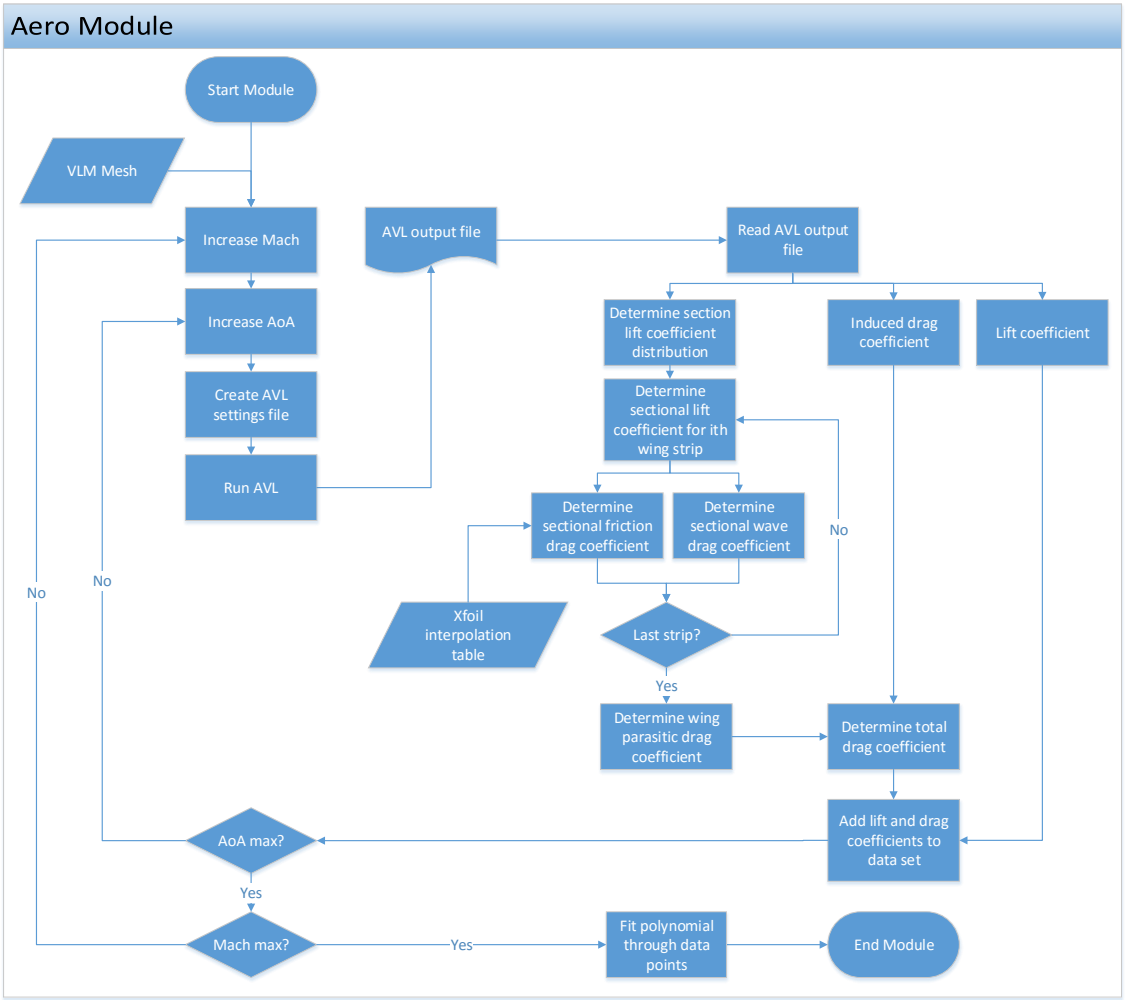

Figure 3.8: Flowchart of the aerodynamics module

These coefficient are determined for the entire range of Mach numbers between 0.4 and 0.8, and angles of attack between 0° and 15°. Using a polynomial fit, the lift and drag polar interpolation tables are created that are required for the mission analysis.

The induced drag coefficient $C_{D_{ind}}$ and lift coefficient C_L of the aircraft configurations are directly obtained from AVL for the given flight conditions. Section 3.5.1 describes how the parasitic drag coefficient of the aircraft is obtained under the given conditions. Section 3.5.2 describes how the computed lift and drag coefficients are interpolated to form the lift and drag interpolation models, which are required by the mission

analysis. Finally, section 3.5.3 discusses how the optimal number of elements for AVL and the optimal number of aerodynamic evaluations is determined.

3.5.1. DETERMINATION OF THE PARASITIC DRAG COMPONENT

As mentioned above, the friction drag is a significant part of the total drag. In this study, the parasitic drag of the aircraft is divided in three components:

- The parasitic drag of the fuselage group
- The parasitic drag of the wing, which is divided in the friction drag and the wave drag of the wing.
- The parasitic drag of the horizontal stabilizer, which is also divided in the friction drag and the wave drag of the horizontal stabilizer.

As mentioned in section 3.3.2, it is assumed that the fuselage group properties do not change in this study. Therefore it is assumed that the total fuselage drag remains constant, i.e. $C_{D,fus} \cdot S_{ref}$ remains constant for each considered configuration. Because the wing reference area can vary significantly in this study, the fuselage drag coefficient for each wing configuration is defined as:

$$C_{D,fus} = \frac{C_{D,fus,baseline} \cdot S_{ref,baseline}}{S_{ref}} \tag{3.9}$$

In which $C_{D,fus,baseline}$ and $S_{ref,baseline}$ are the fuselage drag coefficient and wing reference are of the baseline A320 respectively, as discussed in section 3.3.2.

FRICTION DRAG

As mentioned above, an AVL analysis is performed for a large number of combinations of Mach number and AoA. One of the outputs of this analysis is the sectional lift distribution over the wing and horizontal stabilizer. For each spanwise strip, the sectional lift coefficient c_l is determined.

The airfoil analysis tool XFOIL [37], allows for subsonic viscous airfoil analyses. For the two airfoils considered in this study, the RAE2822 and NACA0012 airfoils, the lift drag polars are constructed for a range of Reynolds numbers at a Mach number of 0. Subsequently, through each polar, a quadratic polynomial is fitted according to equation 3.10 [26].

$$c_{d,friction} = c_{d_0}(Re) + c_{d_1}(Re)c_l + c_{d_2}(Re)c_l^2 \tag{3.10}$$

In which $c_{d_0}, c_{d_1}, and c_{d_2}$ are interpolation constants, which are a function of the Reynolds number. These interpolation coefficient are determined for a range of Reynolds numbers using XFOIL. Subsequently, these calculated interpolation constants are saved and used as an interpolation database in the optimization program.

To obtain the coefficients at the specific Reynolds number of the current wing strip, these coefficients are interpolated as function of the Reynolds number. This way, the three required coefficients at the required Reynolds number are obtained. In combination with the sectional lift coefficient, the sectional drag coefficient can then be determined. Figure 3.9a and 3.9b shows the lift drag polars as function of the Reynolds number for the RAE2822 and NACA0012 airfoils respectively.

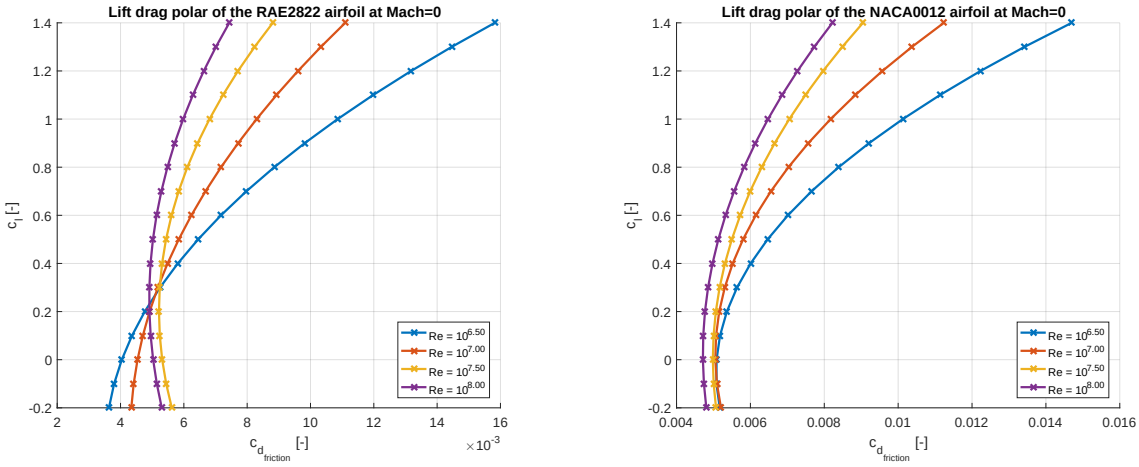

(a) Supercritical RAE2822 Airfoil

(b) Symmetrical NACA0012 Airfoil

Figure 3.9: Airfoil lift drag polars for various Reynolds numbers

WAVE DRAG

In addition to the parasitic drag as discussed in the previous section, the wave drag has to be taken into account. This drag component can be a significant part of the total wing drag at high Mach numbers.

This drag component is determined based on the method as described in [15]. The wave drag of each spanwise wing strip is determined according to equation 3.11.

$$c_{d_{wave}} = \begin{cases} 0 & M \leq M_{cr} \\ 20(M - M_{cr})^4 & M > M_{cr} \end{cases} \tag{3.11}$$

In which M is the free stream Mach number and M_{cr} is the critical Mach number for the current wing strip, which is determined using equation 3.12.

$$M_{cr} = M_{DD} - \sqrt[3]{\frac{0.1}{80}} \tag{3.12}$$

In which M_{DD} is the drag divergence Mach number for a specific wing cross section. This drag divergence Mach number can be calculated using equation 3.13.

$$M_{DD}\cos\Lambda_{0.5c} + \frac{c_l}{10\cos\Lambda_{0.5c}{}^2} + \frac{t/c}{cos\Lambda_{0.5c}} = \kappa_A \tag{3.13}$$

In which $\Lambda_{0.5c}$ is the half chord sweep of the specific wing section, t/c is the thickness over chord ratio of the airfoil, and κ_A is the Korn factor. The factor equals $\kappa_A = 0.95$ for supercritical airfoils, such as the RAE2822, and $\kappa_A = 0.87$ for conventional airfoil, such as the NACA0012 airfoil [15]. Figures 3.10a and 3.10b shows the wave drag coefficient as function of Mach number for various lift coefficient at a half sweep angle of 20°. As can be seen in these figures, the drag divergence Mach number of the NACA0012 profile is lower compared to the supercritical RAE2822 airfoil. Also, its gradient is much steeper than the gradient of the RAE2822 airfoil.

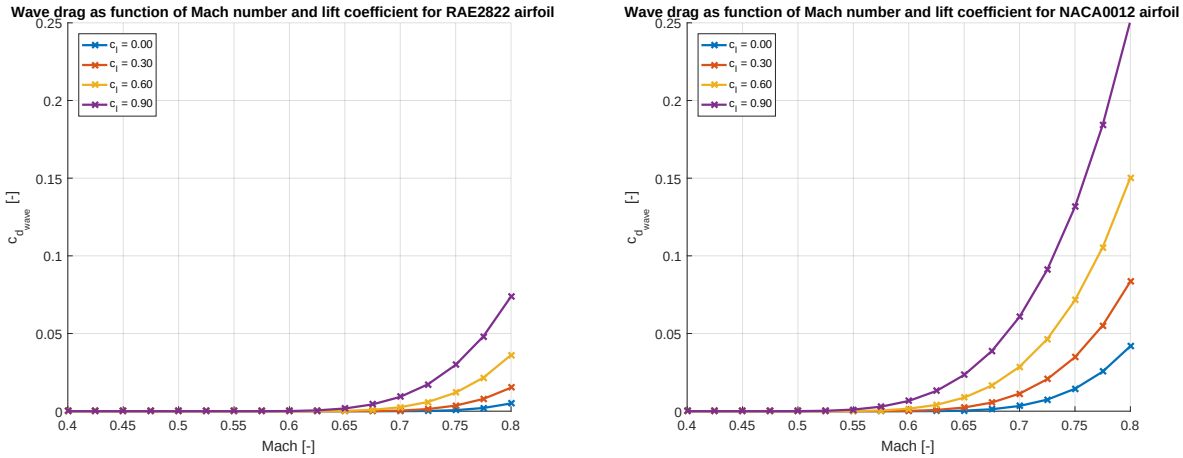

(a) Supercritical RAE2822 Airfoil

(b) Symmetrical NACA0012 Airfoil

Figure 3.10: Airfoil wave drag as function of Mach number

If the friction drag and wave drag coefficients for each strip are determined, the total wing (or horizontal stabilizer) parasitic drag is calculated according to equation 3.14. Because only symmetric flight conditions are considered in this study, it is sufficient to determine the parasitic drag of only one wing, and multiply this with a factor two, as indicated in the equation.

$$C_{D_{para,wing}} = 2\frac{\sum_{i=1}^{n_{strips}}(c_{d,friction_i} + c_{d,wave_i}) \cdot S_i}{S_{ref}} \tag{3.14}$$

In which $C_{d,friction_i}, C_{d,wave_i}$ and S_i are the sectional friction and wave drag coefficients and strip area of the i^{th} strip respectively. The total aircraft parasitic drag is then determined using equation 3.15.

$$C_{D_{para}} = C_{D_{fus}} + C_{D_{wing}} + C_{D_{hor.stab.}} \tag{3.15}$$

After which the total drag coefficient is obtained by summing the parasitic and induced drag components:

$$C_D = C_{D_{para}} + C_{D_{ind}} \tag{3.16}$$

3.5.2. LIFT AND DRAG INTERPOLATION TABLES

Once the aircraft lift C_L and drag C_D coefficients of the aircraft are determined for the entire range of angles of attack and Mach numbers, a fifth order polynomial surface is plotted through these points to create an interpolation table for the lift and drag coefficients as described above. These interpolation models are required by the mission analysis, as will be explained in section 3.8.

For the angle of attack range, a proportional distribution is used, such that the step size in angles of attack remain constant. However, because the drag coefficients can vary significant in the high Mach range, due to the increment of wave drag, a higher number of points is required in this area. At lower Mach numbers, less data points provide enough accuracy to fit the polynomial. Therefore, for the Mach range, a cosinus spacing is used at which the drag coefficients are calculated. This offers an increased accuracy in the high Mach range, while the computational time remains low.

Figures 3.11a and 3.11b show the evaluated lift and drag coefficients (red dots) and the polynomial surface for the reference A320 aircraft. Also, the coefficient of determination (R^2) value is given. According to this value, the polynomial surfaces matches very well with the calculated data points. These two interpolation tables are the input for the mission analysis, at which they are evaluated at each point to solve the equations of motion.

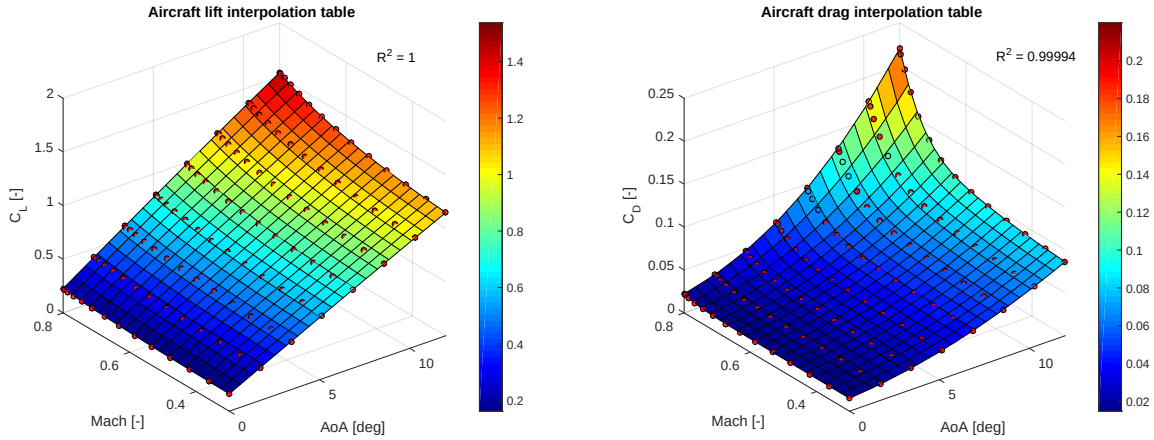

(a) Lift polar as function of Mach

(b) Drag polar as function of Mach

Figure 3.11: Interpolation tables as used in the mission analysis.

3.5.3. OPTIMAL NUMBER OF ELEMENTS

Previous sections described in detail how the aerodynamic characteristics for each configuration are determined for given flight conditions. This section discusses the optimal number chordwise and spanwise that are used in the AVL simulations. In addition, the optimal number of data points in the angle of attack range and Mach range at which the aerodynamic performance is evaluated to form the interpolation model is determined.

OPTIMAL NUMBER OF ELEMENTS AVL

As discussed in section 3.4.2, the number of spanwise elements of each wing segment is determined based in the segments length and the spanwise scaling factor F_{Nb}. Also, the number of chordwise elements can be increased to get a more accurate pressure distribution over the wing. However, increasing the amount of elements results in higher computation times. Therefore an optimum number of elements is selected for which the computational times remain relative low, while a high accuracy of the AVL results is obtained.

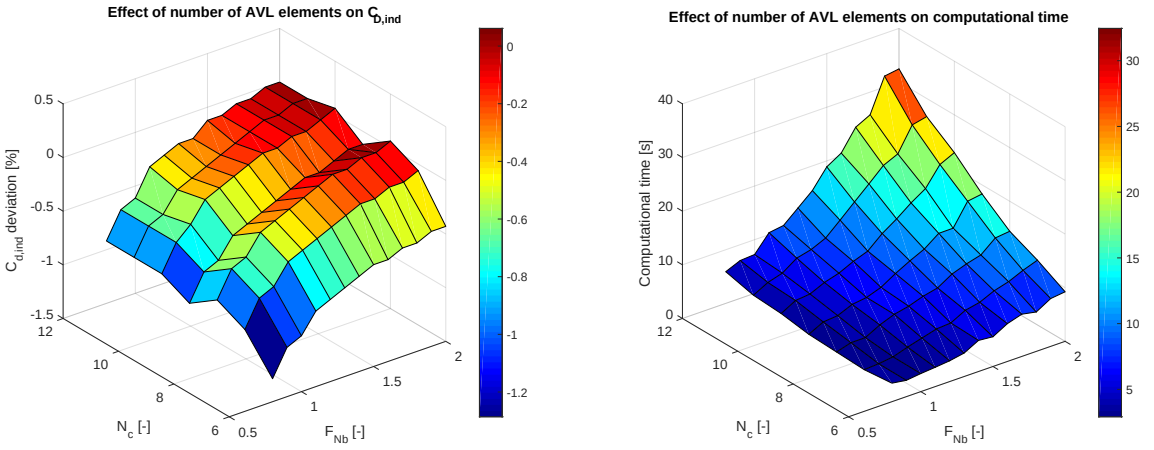

(a) Induced drag error as function of spanwise and chordwise elements

(b) Computation time as function of spanwise and chordwise elements

Figure 3.12: Optimum number of elements in the AVL analysis

Figure 3.12a shows the induced drag deviation in percentage w.r.t. to the most accurate AVL analysis that has been performed with $F_{Nb} = 2$ and $N_c = 12$. Figure 3.12b shows the computational time in seconds as function of the spanwise scaling factor and the number of chordwise elements. The selected number of elements is $F_{Nb} = 1.5$ and $N_c = 10$. As can be seen in the figures, the error in induced drag at this point is approximately 0.3%, while the computational time of one AVL analysis remains relative low with 10s. The minimum number of spanwise elements for each wing segment equals 4, to prevent inaccurate modulation of very small wing segments, such as small wing tips.

OPTIMAL NUMBER OF AERODYNAMIC EVALUATIONS

In addition to the optimum number of elements within an AVL analysis, the number of AVL analyses can also significantly affect the accuracy of the resulting interpolation tables. Increasing the number of AVL analyses increases the accuracy. However, the computational time required to create the interpolation tables also scales with the total number of analyses.

To determine the optimal number of analyses, first the number of analyses for each AoA is varied, while the the number of analyses for each Mach number equals 20, which is considered as very accurate. Figure 3.13 shows the deviation of the drag coefficient C_D w.r.t. the case in which also 20 analyses are performed in the AoA range. It can be seen that increasing the number of AVL analyses in the AoA range results in an higher accuracy. The largest deviations are found at low Mach numbers. The optimal number of analyses in the AoA range is selected to be 8. In this case, the error remains below 0.5% in the entire interpolation table.

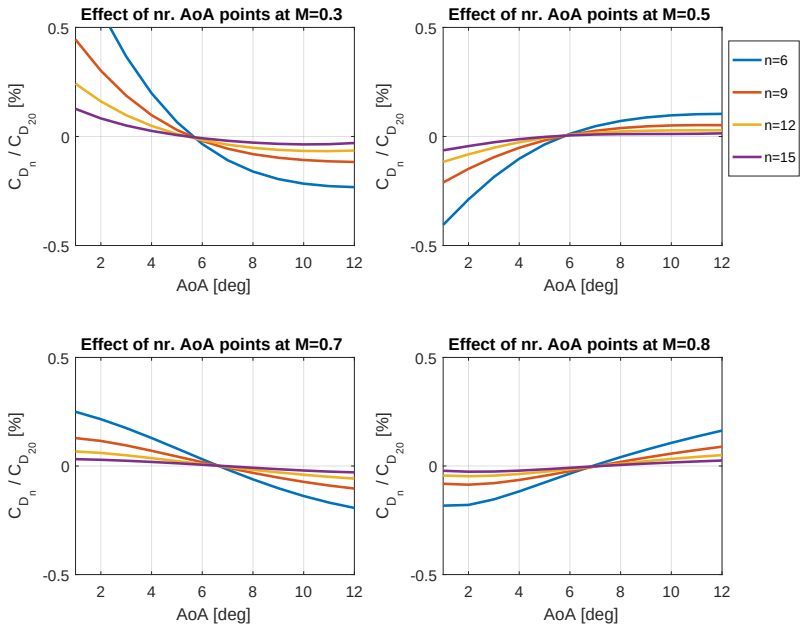

Figure 3.13: Effect of number of points in the Angle of Attack range

Figure 3.14 shows a similar plot. However, in this case the number of AoA analyses equals 20, while the number of analyses in the Mach range is varied. As can be seen, the deviation grows with increasing Mach number. The optimal number of analyses in the Mach range is selected to be 14. Also, in this case the error remains below 0.5% throughout the entire interpolation table.

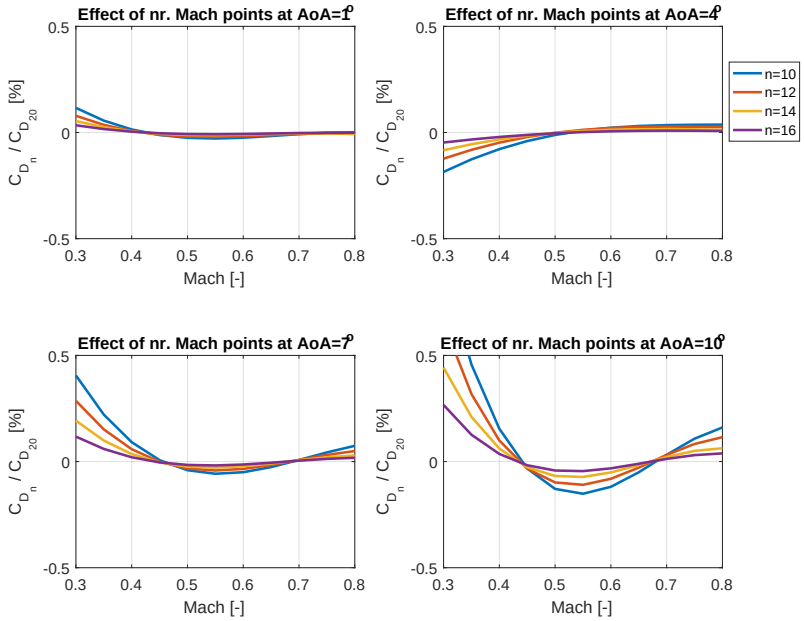

Figure 3.14: Effect of number of points in the Mach range

3.5.4. VALIDATION

To validate the aerodynamic model, the aerodynamic characteristics, C_L and C_D, of the baseline A320 as obtained from the discussed model are compared to the values as obtained from Q3D [38]. Q3D is a validated aerodynamic analyses tool, which combines a VLM method with an airfoil boundary layer analysis tool, such as XFOIL [37], VGK [39], or MSES [40]. In order to validate the model, an input file for Q3D is created that contains exactly the same geometry as used in the current model. Subsequently, both the current model and Q3D evaluate the aerodynamic performance at a range of AoA and Mach numbers.

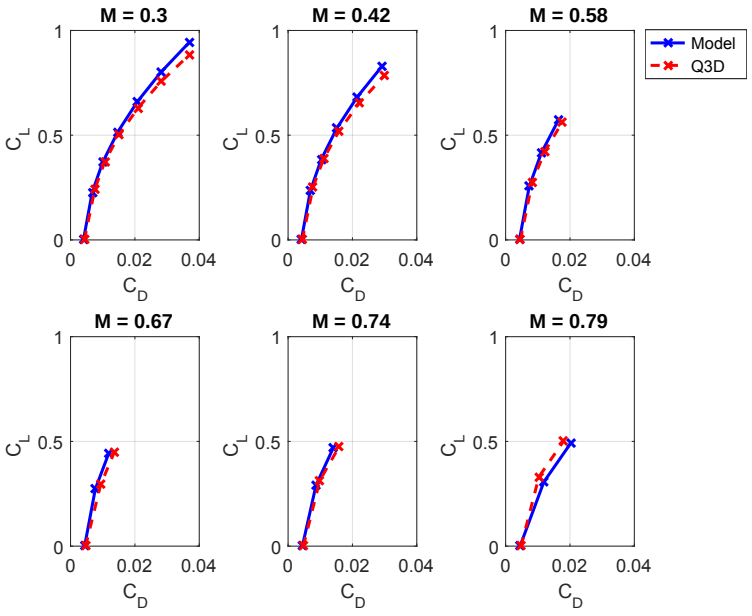

Figure 3.15: Validation of the aerodynamics module with Q3D [38]

Figures 3.15 show the lift drag polars for various Mach numbers. The results of the current model are compared to the results as obtained from Q3D. At the transonic Mach range, Q3D was not able to converge at higher lift coefficients, resulting in only a small amount of data points. As can be seen the two models give comparable results. However, at transonic Mach numbers, especially in combination with higher lift coefficients, the differences between the results of the two programs becomes larger.

3.6. STRUCTURAL MODULE

Figure 3.16 shows the flowchart of the structural module. The input of the structural module are the aerodynamic and structural meshes of the wing. Using an initial wing weight estimation and the fuel weight of the reference A320, the aircraft take-off (TO) weight is established. For this take-off weight, the critical loads at 2.5g condition are determined using AVL. The critical load distribution from AVL is mapped on the structural Nastran model. Using Nastran, the weight of the wing box is minimized under the critical load conditions and stress constraints, by taking a safety factor into account. The optimized wing weight is multiplied with a 'secondary weight factor' to obtain the total wing weight. This process is iterated until the resulting wing weight equals the initial wing weight used to determine the take-off weight to within 0.1%.

The wing box model, critical load determination, wing weight optimization, and tail weight determination are discussed in more detail in this section. Finally, this chapter concludes with the validation of the structural model.

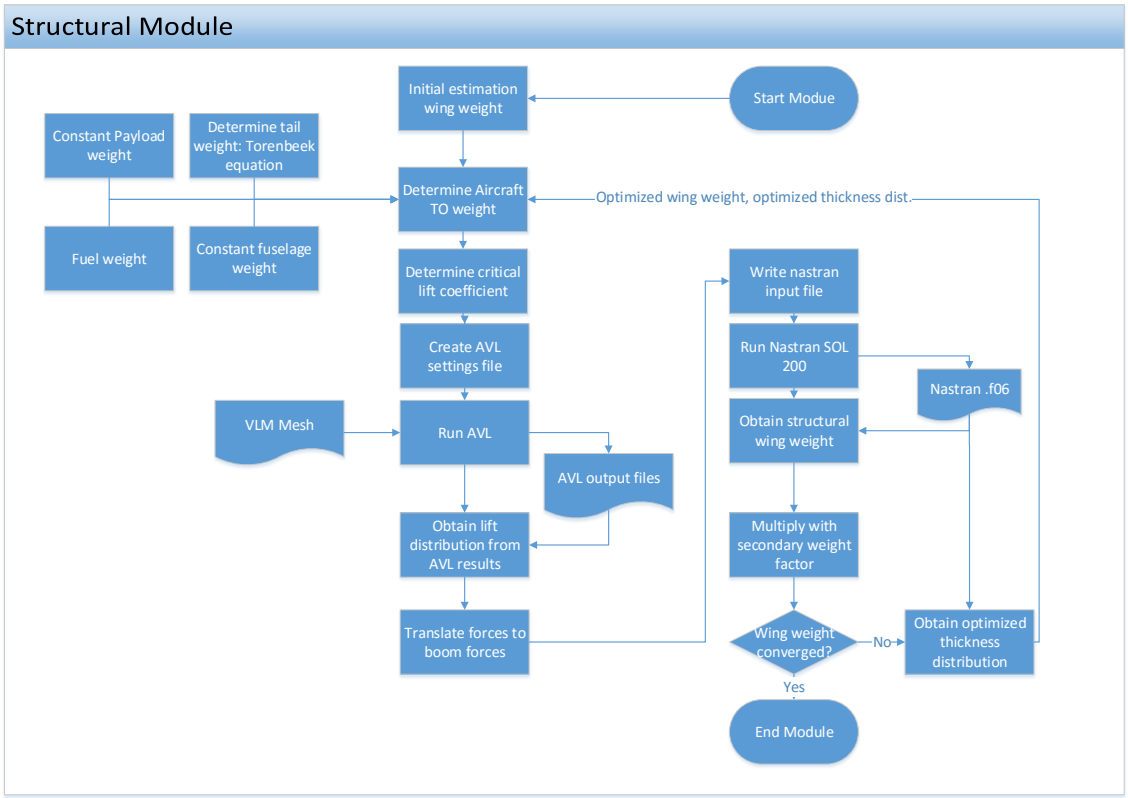

Figure 3.16: Flowcharts of the structures module

3.6.1. WING BOX MODEL

The wing box consists of four skins (top, bottom, front, and rear), and four booms in the four corners respectively, as discussed in section 3.4.2. This model is implemented in Nastran [41] using various elements:

- The skin is modelled using CTRIA3 and CQUAD4 elements, which are defined as a 'isoparametric membrane-bending or plane strain quadrilateral plate elements.' [41]. These elements have three and four corners respectively. The properties of these elements is defined using the PSHELL property which defines the skin thickness and material properties.

- The booms are modelled using CBAR elements, which is a simple beam element with a continuous cross section. The properties of these elements are defined using the PBAR property to give the CBAR elements a cross sectional area and material properties. For the booms a square cross-section has been used.

The material of the wing box, for both the skin and the ribs, is assumed to be Aluminum 7075-T6 [38]. Its material properties are shown in table 3.5 [42]. In addition, a safety factor n_{safety} of 1.5 has been used [12]. Therefore the maximum allowable stress is 335 MPa. Because the skin elements can carry both shear and normal stresses, the Von Mises stress is used as failure criteria. For the boom elements, the maximum normal stresses are considered as failure criteria. In equations, these constraints can be written as follows:

- For the skin elements:
$$\sigma_{vonmises} \leq \frac{\sigma_{y_{Al}}}{n_{safety}} \tag{3.17}$$

- For the boom elements:
$$|\sigma_{normal}| \leq \frac{\sigma_{y_{Al}}}{n_{safety}} \tag{3.18}$$

Table 3.5: Material properties of Aluminum 7075-T6 [42]

Parameter	Value	Unit	Description
E_{Al}	71.7	$[GPa]$	E-modulus
$\sigma_{y_{Al}}$	503	$[MPa]$	Yield stress
ν_{Al}	0.33	$[-]$	Poisson ratio
ρ_{Al}	2810	$[kg/m^3]$	Density

As initial thickness, 7mm is assumed as skin thickness and 120mm is assumed as width of the square booms. However, the computational time required to converge from this initial and constant thickness distribution to the optimal thickness distribution is quite large. Therefore, once the optimal thickness distribution is obtained for a configuration, these thicknesses are used as initial thickness for subsequent Nastran optimization. This reduced the computation times significantly.

3.6.2. CRITICAL LOAD DISTRIBUTION

The first step in the structural module is the determination of the critical loads on the wing. The critical load case is defined as a 2.5g manoeuvre at its critical weight with the high-lift devices retracted up to VMO/MMO, according to FAR 25 [12]. As critical weight, the take-off weight has been used. The take-off weight consists of:

- **Constant fuselage weight:**
The fuselage weight is assumed to be constant in this study. This constant weight contribution is determined in equation 3.1 to equal 33225 kg.

- **Constant payload weight:**
In this study, the payload weight is considered constant and equal to the design payload as given in table 3.1.

- **Tail weight:**
The tail will have a conventional configuration. Therefore an accurate prediction of the horizontal tail

weight can be made using the Torenbeek formula, which is based on empirical relations [34].

$$W_{h-tail} = S_{tail} k_h f \left(\frac{S_{h-tail}^{0.2} V_D}{\sqrt{cos(\Lambda)}} \right) \tag{3.19}$$

Where V_D is the design dive speed, S_{tail} is the surface area of the horizontal tail, k_h is a correction factor for the tailplane configuration which equals 1.0 for a fixed stabilizer. The function f refers to an empirical relationship as obtained from Torenbeek [34].

- **Fuel weight required for the mission:**
  Because the actual block fuel required for the current mission is unknown at this point in the program, the baseline A320 block fuel required for the given mission length, as obtained from Piano-X [27], is used as a fuel weight estimation. The actual block fuel may differ slightly from this reference fuel weight. However, to determine the actual fuel weight, an iteration process over the entire program would be required. This would increase the computation time significantly, while the effect of the optimal wing weight is small because differences between the actual block fuel and the assumed block fuel is only a small percentage of the total take-off weight.

- **Wing weight estimation:**
  Also the wing weight is not known at this point in the program. However, in contrast to the fuel weight, the differences in wing weight are a significant part of the total take-off weight. Therefore the wing weight is iterated until it is consistent with the wing weight used to deterine the critical loads, as shown in figure 3.16. As starting value for this iteration process, the wing box weight of the reference A320 aircraft is taken.

Once the take-off weight is determined, the critical lift coefficient $C_{L_{crit}}$ can be determined using equation 3.20. In this equation, W_{crit} is the take-off weight, V_{MO} the maximum operating speed, rho the density at cruise altitude, S_{ref} the aircrafts reference area, and n_{max} is the maximum load factor of 2.5g.

$$C_{L_{crit}} = \frac{W_{crit}}{1/2 \rho V_{MO}^2 S_{ref}} \cdot n_{max} \tag{3.20}$$

This critical lift coefficient, maximum operating speed, and density are the input for the AVL analysis to determine the critical load distribution. This critical lift distribution is then mapped on the structural model. The airfoil lift coefficient of each spanwise element is multiplied with the area of same element, the dynamic pressure, and the local normal vector to obtain the local normal force at a given spanwise element, see equation 3.21.

$$L_i = c_{l_i} \cdot S_i \cdot q \cdot u_i \tag{3.21}$$

In which c_{l_i} refers to the sectional lift coefficient, S_i to the segments area, q to the dynamic pressure, and u_i to the segments normal vector.

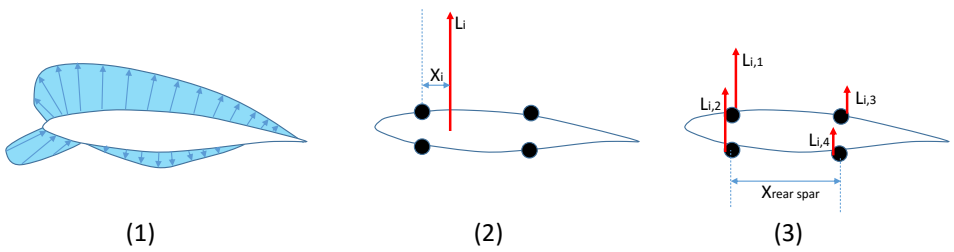

Figure 3.17: Mapping of aerodynamic loads on the structural model.

In addition to the normal force, the lift distribution on the cross section may also result in a torque. The chord-wise location at which the resultant load acts is also obtained from AVL. In the Nastran model, the

loads are placed on the four boom nodes, see figure 3.17. Placing the loads on the skin results in large local deformations, which results in inaccurate results. The two loads at the front spar $L_{i,1}$ and $L_{i,2}$ are equal, and the two loads at the rear spar $L_{i,3}$ and $L_{i,4}$ are equal. These loads are divided such that equations 3.22 and 3.23 are satisfied, to comply with the total force and torque as created by the pressure distribution.

$$L_i = L_{i,1} + L_{i,2} + L_{i,3} + L_{i,4} \tag{3.22}$$

$$L_i \cdot x_i = (L_{i,3} + L_{i,4}) \cdot x_{rear-spar} \tag{3.23}$$

In addition to the aerodynamic loads some other loads are taken into account:

- **The fuel weight:**
  As mentioned in section 3.1 it is assumed that 85% of the block fuel is stored in the wings. The fuel tank is assumed to range from the wings root up to 75% of the wing semi-span. In an equivalent way to the aerodynamic loads, these fuel loads are distributed over the four booms. This results in a bending relief of the wing.
- **The engines:**
  The engines are modelled as point loads at a fixed spanwise percentage on the wing. The engines are modelled by a weight and a thrust point loads.
- **The gravity:**
  The gravitational parameter is introduced in the Nastran model. The addition of the gravitational forces results in a small bending relief.

After all the loads are determined, these are written to a Nastran input file, which is used to determine the stress and optimize the thickness of the various elements as will be discussed in the next section.

3.6.3. STRUCTURAL WING BOX OPTIMIZATION

If the Nastran input file with the critical loads is created, it can be analyzed using Nastran SOL 101 [41]. This is a static analysis, which computes the stress distribution in the wing box. Also, the structural wing box mass is computed by Nastran, which equals the amount of required material multiplied by its density. The results for the reference A320 aircraft are shown in figure 3.18. The upper image shows the skin thickness in mm (left), and the skin Von Mises stress distribution in MPa (right). The lower image shows the boom width in mm (left) and the boom normal stress distribution in MPa (right).

It can be seen that this wing box satisfies the stress constraints because the stresses remain under 335 MPa. However, this constant thickness distribution along the wing span is not the most efficient in terms of wing weight. For example, at the wing tip the stresses are lower than at the root, which allows for thinner skins and booms.

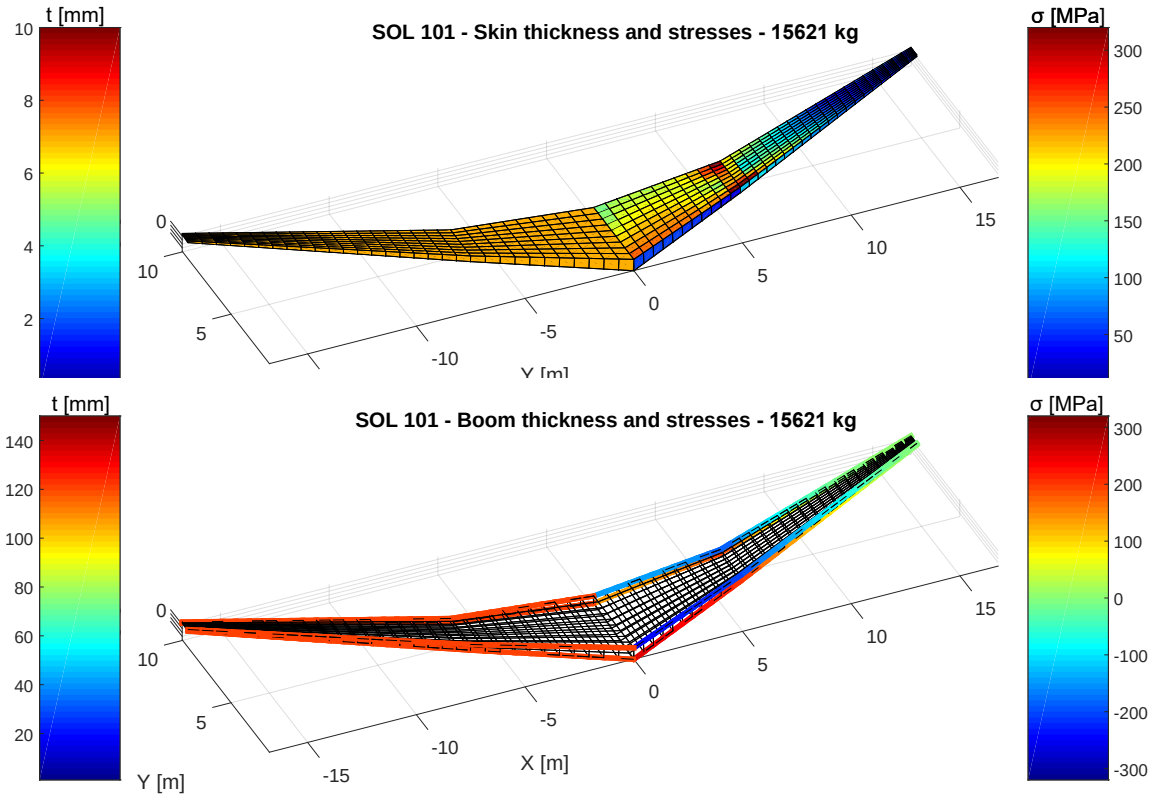

Figure 3.18: Stress distributions as result of a SOL 101 analysis for given skin and boom thicknesses.

Therefore, the thickness of each element is optimized using Nastran SOL 200 to obtain the minimum wing weight that satisfies all the stress constraints. In addition, the minimum thickness is constraint due to manufacturing reasons. The minimum allowable skin thickness is assumed to be 1 mm. The minimum boom width is assumed to be 10 mm. Table 3.6 shows the optimization parameters for SOL 200.

Table 3.6: Nastran SOL 200 optimization settings

Parameter	Value	Unit	Description
DELX	3e-3	[-]	Gradient estimation step size
DESMAX	1000	[-]	Maximum number of iterations
DXMIN	1e-6	[mm]	Minimum design variable move limit
METHOD	Modified Method of Feasible Directions	[-]	Optimization method
CONV1	4e-3	[-]	Relative criterion to detect convergence

Figure 3.19 shows the results of the SOL 200 analysis for the A320 reference wing. As indicated in the figure, the wing weight is significantly reduced while it still meets the stress criteria. In this top figure, it can be seen that the wing box is almost fully stressed, i.e. the stress at almost each element in the wing box is equal to the maximum allowable stress. Also, it can be seen that the thickness of the skin varies in chordwise direction. At the location of the kink, the thickness is increased to meet the stress constraints. In the lower figure, it can be seen that the booms are also almost fully stressed. Only at the wing tip, the normal stresses are lower than the maximum allowable stresses because manufacturing constraint is active which limits the minimum thickness to 1mm. Finally, it can be observed that the two booms at the upper skin are loaded in compressional stresses, while the lower booms are loaded with tensional stresses. This is the result of the upward bending wing due to the lift forces.

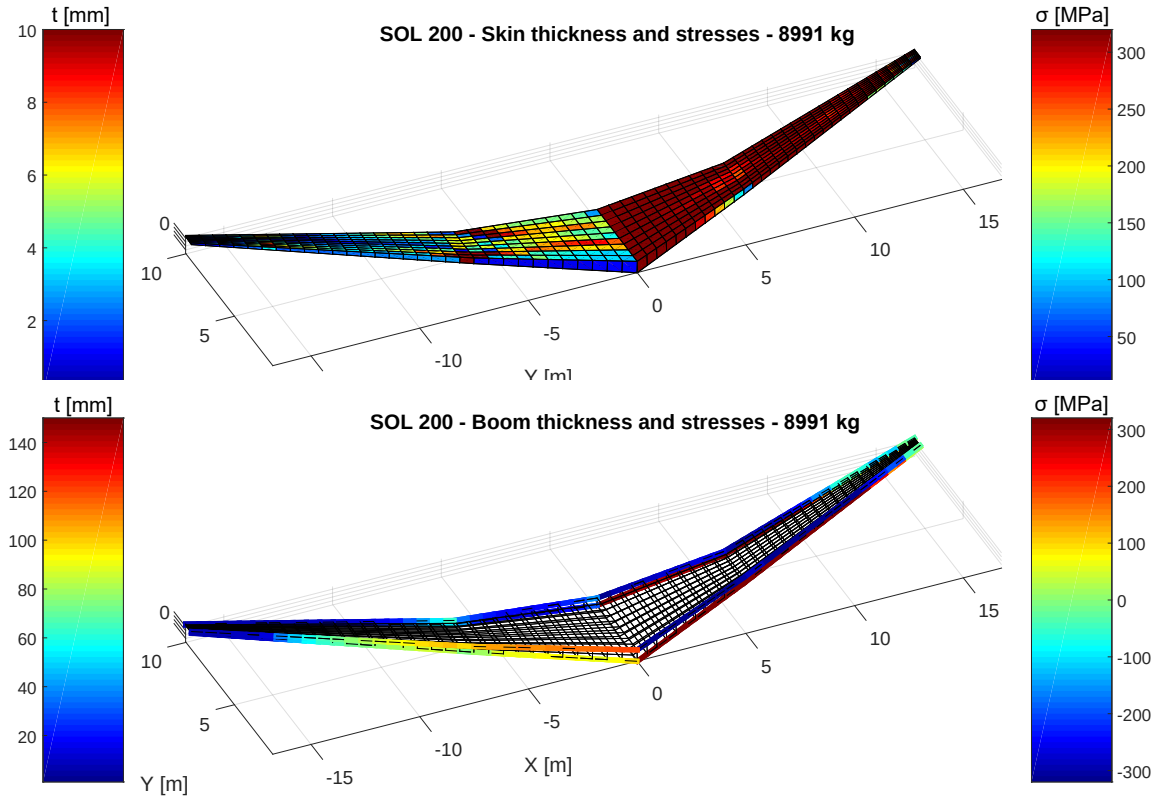

Figure 3.19: Optimized thickness and stress distributions as result of a SOL 200 optimization

However, an aircrafts wing also consists of ribs, fuel tank, wiring, etc. [43]. Therefore a 'secondary weight' factor is introduced to account for these non-structural wing components. This factor is defined as equation 3.24, which is the results of a regression analysis between the actual wing box weight and the structural box in the range of 800 kg to 12000 kg for the structural weight [38].

$$W_{wing,total} = 9.1669 \cdot (2 \cdot W_{Nastran})^{0.8248} \tag{3.24}$$

3.6.4. OPTIMAL NUMBER OF ELEMENTS

As discussed in section 3.4.2, the wing box is meshed in N_c, N_b, and N_v elements. The number of elements in the vertical direction N_v is set to one. Increasing the number of elements in this direction does not affect the wing mass significantly. The number of elements in chordwise direction N_c is also assumed to equal one in this study. Allowing multiple chordwise elements significantly increases the required computational times. Equivalent to the number of spanwise elements in the AVL model, the number of elements in spanwise direction N_b varies with the span of the wing segment according to the following relation:

$$N_{b_i} = b_i \cdot K_{N_b} \tag{3.25}$$

Where b_i is the span in the i^{th} wing segment. K_{N_b} is the spanwise number of elements factor. Also for the structural model, the minimum number of elements for each wing segment is set to four, in order to accurately model very small wing segments.

Increasing the number of elements may increase the accuracy of the structural model, however this also increases the computational time. Therefore the optimal number of elements has to be determined at which the optimized wing weight becomes more or less mesh independent but the computational time is still at an acceptable level. Therefore the optimum number of spanwise elements has been determined. In addition, the convergence criteria of Nastran, may have a significant effect of the results. Therefore, also an optimal value for this settings has been selected. Figure 3.20a shows the normalized wing weight as function of the number of spanwise elements scaling factor F_{Nb} and the *CONV1* setting of Nastran. Figure 3.20b shows the

computational time for each corresponding Nastran run. It can be seen that the wing weight at a spanwise scaling factor of 1.5 and a *CONV1* setting of $4 \cdot 10^{-3}$ approximates the wing weight within 1% of the most accurate value while the computational time is approximately 10 seconds. This point is indicated by the red dot in both figures. Because this number of elements converges to an accurate wing weight within an acceptable time, this number of elements and convergence criteria have been selected to be used in this study.

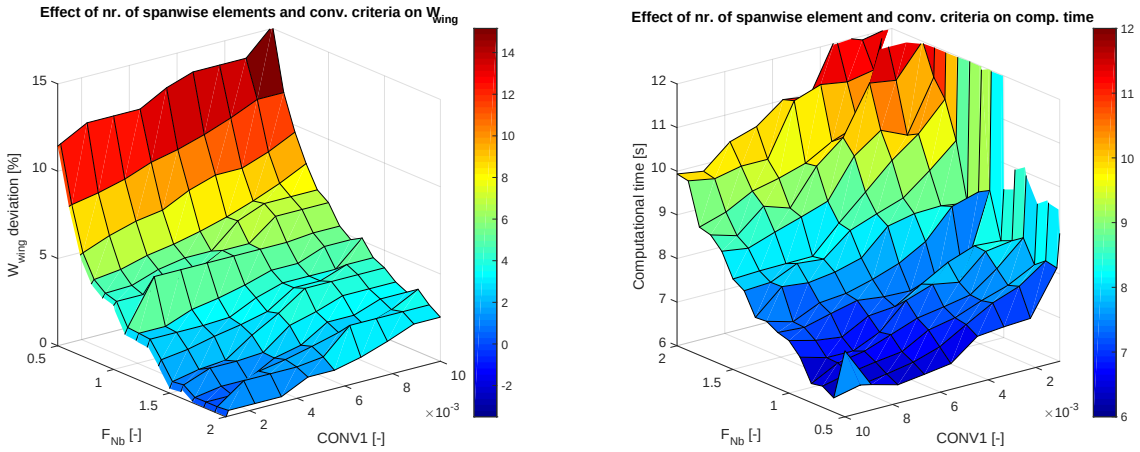

(a) Effect on accuracy

(b) Effect on computation time

Figure 3.20: Optimal number of spanwise elements on convergence criteria for the structural module

3.6.5. VALIDATION

The structural module has been validated using Torenbeeks method, Howe method, and EMWET [34, 38, 44]. For five small to mid-range aircraft, the wing mass is estimated using the wing planform parameters as input [29]. The actual wing mass of these aircraft is obtained from literature. Table 3.7 shows the initial service year, MTOW, wing area, and wing weight for each of these aircraft. The last column in the table shows the source from which the planform parameters and the actual wing mass are obtained respectively.

Table 3.7: Characteristics of aircraft used for the structural validation

Aircraft	Initial service date	MTOW [kg]	Wing area [m^2]	W_{wing} [kg]	Source
Douglas DC-9-10	1965	35245	86.77	4248	[29, 36]
Douglas DC-9-40	1968	51710	92.97	5394	[29, 36]
MD-83	1980	72580	112.3	7184	[29, 36]
Boeing 727-200	1970	95028	157.9	8405	[29, 36]
Airbus A320-200	1988	73500	122.4	8673	[29, 38]

The EMWET weight estimation is obtained using the student edition of EMWET [38]. The wing planform parameters are defined in the input file, together with the CST coefficients of the airfoils for each segment. Using a quasi-3D method the aerodynamic loads are estimated under 2.5g condition. Using these loads and the wing planform, EMWET converges to a wing weight estimation [38].

The results of the wing weight estimation using the various methods are shown in figure 3.21. It can be seen that Torenbeek's method overestimates the wing weight of these small to mid-range aircraft. However it stays within 20% of the actual wing weight. Howe's method and EMWET are more accurate and stay within 5% of the actual wing weight. The current model, which is indicated by the *Nastran model* slightly underestimates the actual wing weight. However, it stays within 5% of the actual wing weight. Therefore it is concluded that the structural module provides an accurate estimation of the wing weight.

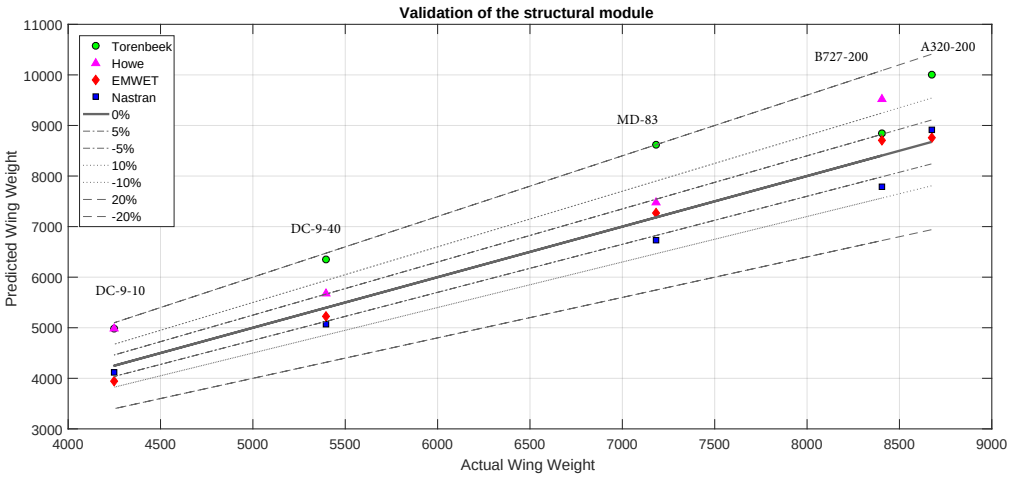

Figure 3.21: Validation of the structural module: Wing weights as determined using various methods as function of the actual wing weight

3.7. PROPULSION MODULE

In order to perform a full mission analysis, the maximum thrust and thrust specific fuel consumption (TSFC) at each point in the flight should be known. One method to determine these parameters is to include an engine simulation program in the mission analysis. However, to obtain accurate results from the mission analysis, a large number of points should be evaluated, as will be discussed in more detail in section 3.8. To reduce the computational time, two interpolation tables are created for a CFM65-5B. The maximum thrust (T_{max}) as function of altitude (h) and Mach number (M), and the SFC as function of altitude (h), Mach number (M), and engine thrust (T), equation 3.26 and 3.27 respectively.

$$T_{max} = InterpTable(h, M) \tag{3.26}$$

$$SFC = InterpTable(h, M, T) \tag{3.27}$$

These tables are created using the 'Gas turbine Simulation Program' (GSP) [45], which is an in-house tool of the Netherlands Aerospace Center (NLR).

3.7.1. INTERPOLATION TABLE MAXIMUM THRUST

To determine the maximum thrust, the core rotational speed (N2) has been set to 100% [46]. By subsequently varying the altitude and Mach number using the GSP API [45], the maximum thrust is determined. Table 3.8 shows the combinations of altitudes and Mach numbers which are evaluated using GSP. As can be seen in the table, a total of 475 data points is evaluated. Finally, a interpolation table is created using MATLAB's *ScatteredInterpolation* function.

Table 3.8: Combination of altitudes and Mach numbers that are evaluated to determine the maximum thrust using GSP [45]

Parameter	Unit	Min value	Max value	Step	Nr. Points
Mach	[–]	0	0.9	0.05	19
Altitude	[km]	0	12	0.5	25

Using this interpolation table, figures 3.22a and 3.22b are created. Figure 3.22a shows a 3 dimensional view of the maximum thrust as function of the altitude and Mach number. Figure 3.22b represents the same data in 2d: the effect of the altitude on the maximum thrust for various Mach numbers.

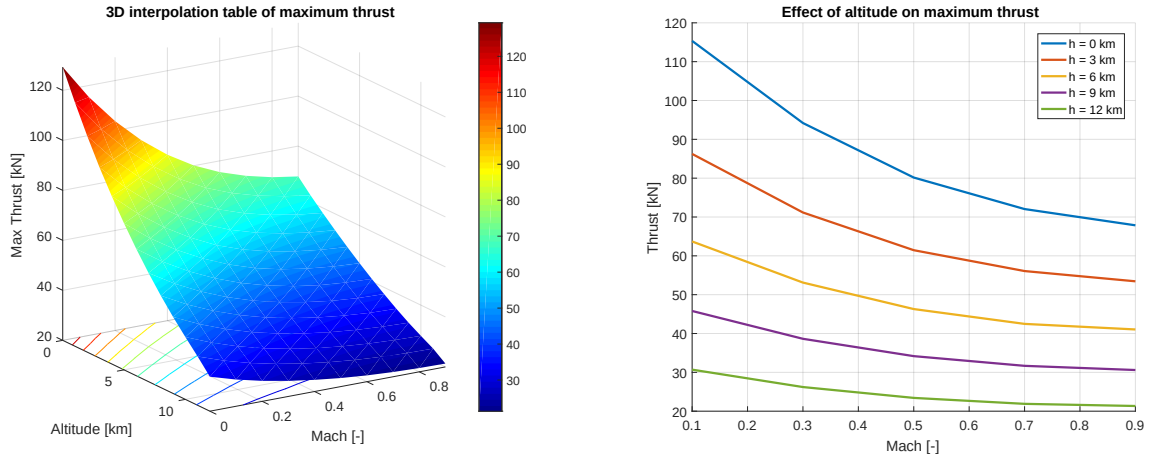

(a) Isometric view of the created interpolation table for max. thrust

(b) Thrust as function of Mach number for various altitudes

Figure 3.22: Maximum thrust as function of altitude and Mach as obtained from GSP for the CFM56-5B engine model [45]

3.7.2. INTERPOLATION TABLE SFC

To create the interpolation table for the SFC, the GSP API has been used to determine the SFC as function of altitude, Mach number, and thrust. In order to determine the thrust range between 0 and T_{max}, the power setting (Γ) has been introduced, which is defined as the thrust divided by the maximum thrust at a given altitude and Mach number:

$$\Gamma = T / T_{max} \tag{3.28}$$

Table 3.9 shows the combination of points that are evaluated to construct this interpolation table. Note that the table indicates that the power setting is varied, however this power setting is multiplied with the maximum thrust at each point to determine the actual thrust, which is used as input for GSP. By varying the power setting instead of the actual thrust, an equivalent number of points are evaluated for each combination of altitude and Mach number. The evaluated data points are transformed to an interpolation table using MATLAB *Scateredinteprolant* function.

Table 3.9: Combination of altitudes and Mach numbers that are evaluated to determine the SFC using in GSP [45]

Parameter	Unit	Min value	Max value	Step	Nr. Points
Mach	[−]	0	0.9	0.05	19
Altitude	[km]	0	12	0.5	25
N2	[%]	5	100	1	96

Figures 3.23a and 3.23b show the effect of Mach and the PS for various altitudes. The data in these figures is obtained from the created interpolation table. From figure 3.23a, it can be seen that the SFC increases with Mach number, and decreases with altitude. Also, it can be seen that some combinations of Mach number and altitude are not possible, e.g. high mach number on low altitude. Therefore extrapolation of this interpolation table is disabled to prevent unfeasible results in the mission analysis.

Figure 3.23b shows the effect of the power setting at a Mach number of 0.7. From this figure can be concluded that the SFC decreases with an increasing power setting. At high power settings (between 0.7 and 1.0), variation in the power setting has a small effect on the SFC. However this effect increases exponentially at lower power settings.

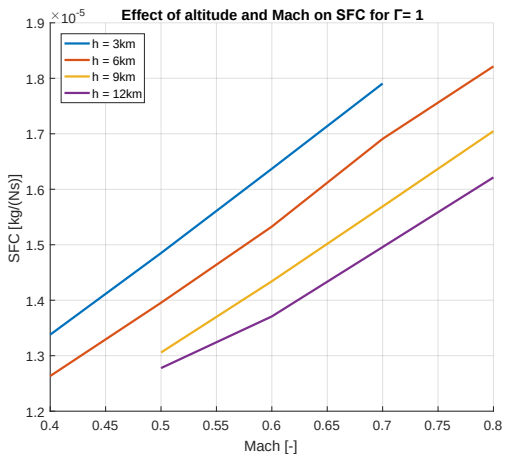

(a) SFC as function of Mach for various altitudes

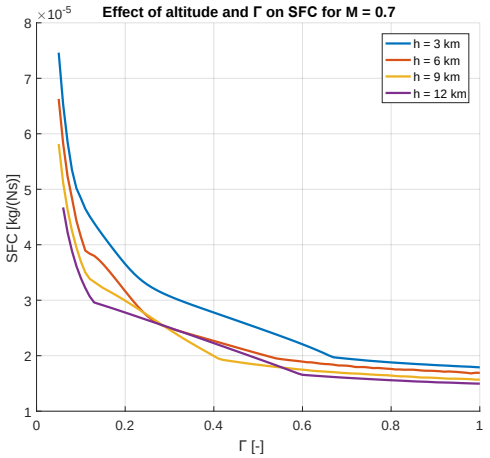

(b) SFC as function of Power setting for various altitudes

Figure 3.23: SFC as function of Mach and Power setting as obtained from GSP for the CFM56-5B engine model [45]

3.8. MISSION MODULE

The mission module combines the results of the aerodynamics and structural module to determine the fuel consumption and block time. Figure 3.24 shows the flowchart of this module.

For this study, the flight performance during ground roll, take-off, and first part of climb are not modelled. During these phases a lot of changes in the aircraft geometry affect the flight performance, such as the deployment of the flaps and the undercarriage. Since these phases are only a small fraction of the entire mission their flight performance is not modelled in the mission analyze module. The fuel consumption for these phases is computed using fuel fractions, as discussed in section 3.3.4. The mission analysis will start at 1500ft, where it is assumed that the flaps and the undercarriage are retracted.

The first step in the mission analysis is to determine the take-off weight using an initial block fuel estimation, see equation 3.29. Subsequently the fuel burn during the engine warm up, taxi, and climb till 1500ft is determined using a fixed fuel fraction as determined in section 3.3.4. The mission from 1500ft climb to 1500ft descent is divided in 11 mission segments, 5 for the climb phase, 1 for the cruise phase, and 5 for the descent phase. Each of these segments is divided in a number of points at which the equations of motion (EoM) are solved using a Newton-Raphson method to determine the state of the aircraft. Subsequently the fuel flow and the time required to fly from one to another point can be determined. This process is discussed in more detail in section 3.8.1. Section 3.8.2 discusses the assumptions and properties of each of the 11 mission segments.

$$W_{TO} = W_{fuselage} + W_{wing} + W_{hor.stab.} + W_{PL} + W_{blockfuel} \tag{3.29}$$

Once each of the 11 mission segments are evaluated, the cruise range is iterated until the computed range equals the required mission range. Finally the fuel burn in the final approach, landing, and taxi are determined using a fixed fuel fraction, as discussed in section 3.3.4. The resulting block fuel is multiplied by 1.2 to account for 20% reserve fuel. Because the initial block fuel affects the resulting block fuel of each mission analysis, this process is iterated until the initial block fuel equals the resulting block fuel.

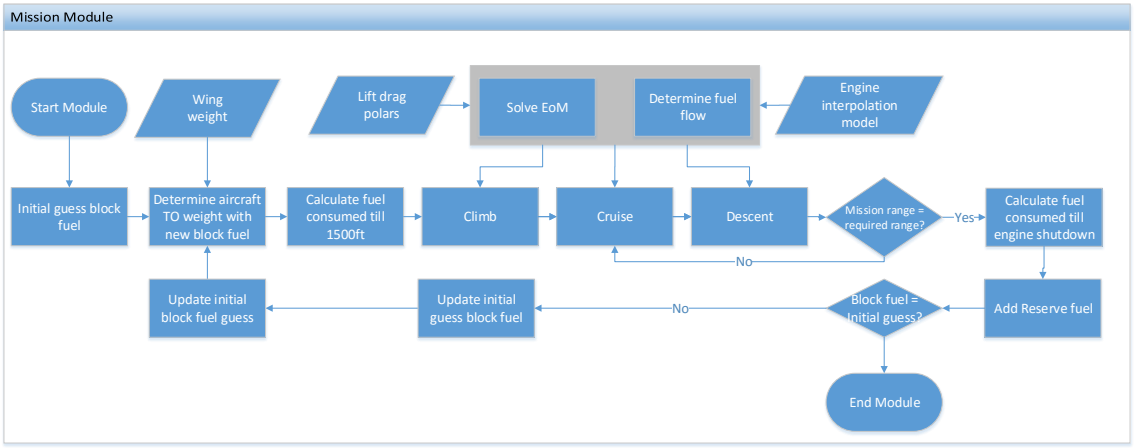

Figure 3.24: Flowchart of the mission module

3.8.1. STATE OF THE AIRCRAFT

The section describes how the fuel consumption at each point in the mission profile is determined. In order to do this, the state of the aircraft is required, which is determined using the Equations of Motion (EoM).

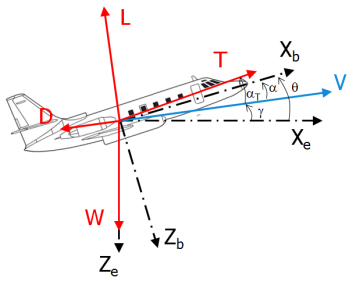

Figure 3.25: Free Body Diagram of an symmetric aircraft [47]

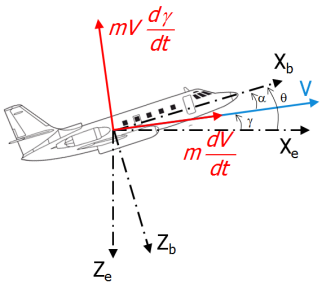

Figure 3.26: Kinetic Diagram of an symmetric aircraft [47]

Figure 3.25 and 3.26 shows the parameters used to describe the aircraft performance as a point mass. Using these parameters in combination with Newton's second law $F = m \cdot a$, the following equations of motion (EOM) can be established:

$$T cos(\alpha_T) - D - W sin(\gamma) = m \frac{dV}{dt} \tag{3.30}$$

$$L - W cos(\gamma) + T sin(\alpha_T) = mV \frac{d\gamma}{dt} \tag{3.31}$$

Where:

- $T(V, h, \Gamma)$ is the thrust of the aircraft. It is a function of the velocity V, altitude h, and throttle setting Γ.
- α_t is the incidence angle of the engines. This value is assumed to equal the angle of attack of the aircraft, i.e. $\alpha_t = \alpha$.
- $D(V, h, \alpha)$ is the drag of the aircraft. It is a function of the velocity V, altitude h, and angle of attack α.
- W is the weight of the aircraft. This value gradually reduces since fuel is consumed.
- γ is the flight path angle.
- $L(V, h, \alpha)$ is the lift of the aircraft. It is a function of the velocity V, altitude h, and angle of attack α.

When the mass of the aircraft is known, the 5 unknowns in these two equations remain: α, V, h, γ, and Γ. By specifying at least three of these parameters, two parameters remain variable. The state of the aircraft can then be determined by solving for these two unknowns using the two EoM. Which parameters can be specified for a given point in the mission depends on the current flight condition, as will be discussed in the next section.

Once the state of the aircraft is determined, the fuel flow can be determined by multiplying the required thrust with the SFC, see equation 3.32. As discussed in section 3.7, the SFC is a function of the Mach number, attitude, and thrust, which are all known at this point.

$$f = T \cdot SFC(M, h, T) \tag{3.32}$$

After the fuel flow is determined at each point in the mission, it can be integrated w.r.t. time to obtain the block fuel of the aircraft for the given mission profile.

3.8.2. MISSION SEGMENTS

A typical mission profile consists of different segments. For a commercial transport aircraft, these segments include take-off, climb, cruise, and descent. Figure 3.27 shows a schematic representation of a typical mission profile for an A320. The shown velocities and altitudes are obtained from Airbus Flight Operations Support [48].

In this mission model, the aircraft climbs from 1500ft at a constant EAS to a given altitude (segment 1) at which it accelerates to higher constant EAS (segment 2). At this EAS, the aircraft climbs until it reaches the crossover altitude (segment 3), which is defined as the altitude at which the constant EAS equals the specified top of climb (ToC) Mach number. At this point the aircraft will continue to climb at constant Mach number until cruise altitude is reached (segment 4). If the ToC Mach number is lower than the cruise Mach number, the aircraft is required to accelerate to the cruise Mach number at the initital cruise altitude (segment 5).

In the cruise phase (segment 6), the Mach number remains constant. Due to the consumption of fuel, the aircrafts weight decreases. Therefore it is more efficient to gradually climb along the cruise phase, as described below. The descent phase is performed in a similar way as the climb phase, but inverted: the first part of the descent is performed under constant Mach number, followed by segments of constant EAS.

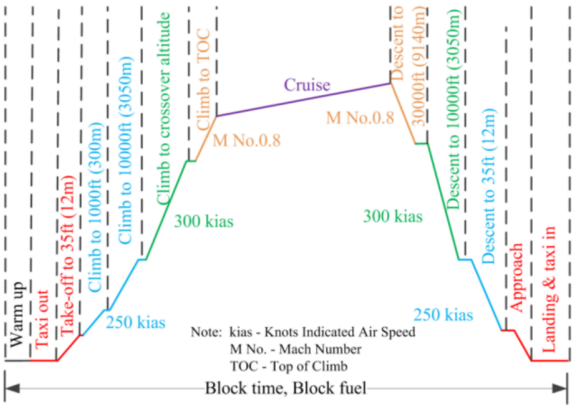

Figure 3.27: Typical flight mission for an A320 [49]

Climb

An aircraft typically climbs at 100% thrust setting. Therefore the throttle setting Γ during the the climb phase (segments 1 to 5) is assumed to be 1. As can be seen in figure 3.27, the climb is performed at constant equivalent airspeed (EAS) or constant Mach number at Top of Climb (ToC). The definitions for these parameters is shown below. It can be seen that the airspeed only depends on the altitude h. So by selecting a certain altitude, the true airspeed at that point is also fixed. Therefore, by specifying the altitude, the two unknowns

remain the flight path angle γ and the angle of attack α. Their values can be determined by solving the EoM using the Newton-Raphson method. The derivative of airspeed w.r.t. time can be determined using an iterative approach.

$$V = EAS\sqrt{\frac{\rho_0}{\rho(h)}} \tag{3.33}$$

$$V = M\sqrt{\gamma RT(h)} \tag{3.34}$$

At the horizontal acceleration segments (segment 2 and segment 5), the flight path angle equals zero, since a horizontal acceleration is assumed. In addition, the altitude and throttle setting are known, so the EoM can be solved to obtained the AoA α and the true airspeed V_{TAS}.

Cruise
In the cruise phase, the aircraft is assumed to fly at constant Mach number. The aircraft will fly at a constant lift coefficient C_L, which is defined according to equation 3.35.

$$C_{L_{cruise}} = \frac{2W_{start-cruise}}{\rho V_{TAS}^2 S_{ref}} \tag{3.35}$$

The altitude that provides the most fuel-efficient cruise at the start of the cruise phase is not the same as the optimal altitude at the end of the cruise. Since the aircraft weight gradually decreases due to the fuel burn, the most fuel-efficient flight altitude gradually increases, according to equation 3.35. By assuming a constant cruise Mach number M and by fixing the lift coefficient, and consequently the angle of attack α, the two unknowns remain the flight path angle γ and the throttle setting Γ, which can be determined by solving the EoM.

Descent
The descent phase is comparable to the climb phase, but inverted. During the first part of the descent, the aircraft will fly at constant Mach number followed by segments of constant EAS. In a real flight, the engine is set in idle conditions. Because it requires a very accurate engine model to determine the idle thrust of an engine, which is beyond the scope of this study, the idle thrust is assumed to be 7% of the maximum thrust at a given flight condition. According to ICAO, this is a representative percentage of the idle thrust [50].If at each altitude, the airspeed and idle thrust are known, the remaining unknowns are the angle of attack α and the flight path angle γ. These unknowns can be solved using the EoM.

Analogue to the horizontal acceleration phases, also in the horizontal deceleration phases (segment 7 and segment 10), the flight path angle γ, altitude h, and throttle setting Γ are known. So the EoM can be solved to obtained the AoA α and true airspeed V_{TAS}.

3.8.3. OPTIMAL NUMBER OF ELEMENTS

Analogue to the aerodynamic and structural module, the optimum number of steps in the mission analysis has been determined. in this mission analysis two different step sizes are considered: an altitude step Δh size which is used for the climb and descent segments, and a cruise distance step Δt_{cruise}, which is used for the acceleration, deceleration, and cruise segments, see equations 3.36 and 3.37 respectively. As can be seen, these step-sizes depend on the mission accuracy factor K_{acc}.

$$\Delta h = 50 \cdot K_{acc} \tag{3.36}$$

$$\Delta t = 10 \cdot K_{acc} \tag{3.37}$$

Figure 3.28a and 3.28b show the accuracy of the mission model and the computational time required for different values of K_{acc} respectively. The block fuel in these figures is normalized to the block fuel using the most accurate settings of K_{acc} = 0.2. From figure 3.28a can be concluded that the accuracy of the model increases with lower accuracy factors. The selected accuracy factor is 0.5. This accuracy factor results in a deviation smaller than 0.1% w.r.t. the case with an accuracy factor of 0.2. From figure 3.28b can be concluded that the computational time for an accuracy factor of 0.5 equals approximately 40s. Also, in this figure two peaks are visible at accuracy factors of 0.8 and 1.5. This is due to additional iterations, which are required to converge the block fuel.

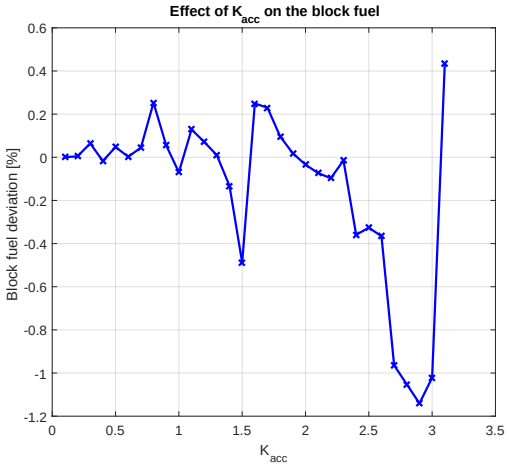

(a) Effect of the mission accuracy factor on the error in block fuel

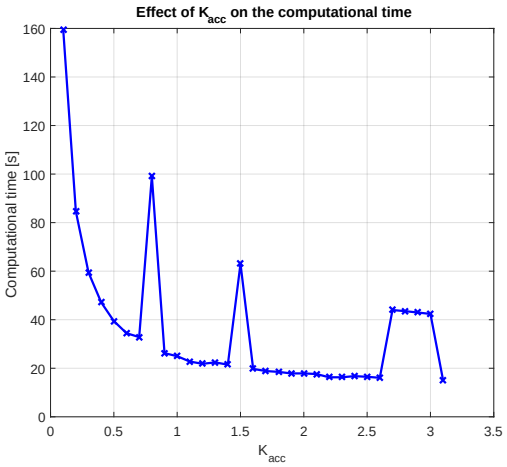

(b) Effect of the accuracy factor on the computational time

Figure 3.28: Determination of the accuracy factor for the mission module

3.8.4. VALIDATION

This section discusses the validation of the mission module. The results of the above presented model are compared to the commercial mission analysis tool Piano-X [27] for the baseline A320 for a mission profile of 1000km. The flight speeds of both models equal those as indicated in figure 3.27.

Figure 3.29a shows the altitude as function of the distance as obtained from the two models. As can be seen, the climb phase of both models is very comparable. In the cruise phase, the altitude gradually increases for the current model as discussed above. However, Piano-X simulates a constant altitude cruise phase. Therefore, small differences are visible in this phase. Finally, it can be seen that the descent phases are also very comparable. Figure 3.29b shows the flight path angle as function of the distance. Also these results are very comparable. Only in the initial climb segment, the current model shows higher flight path angles compared to Piano-X.

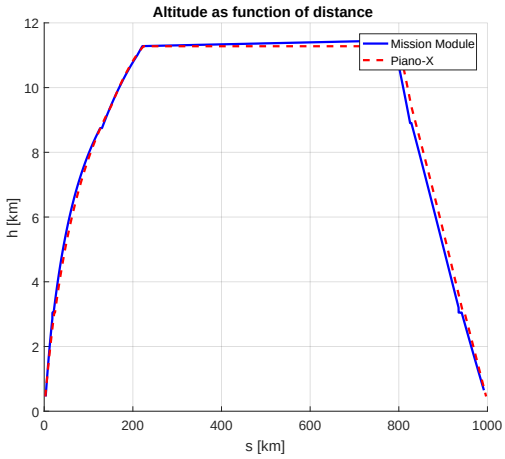

(a) Altitude as function of flight distance

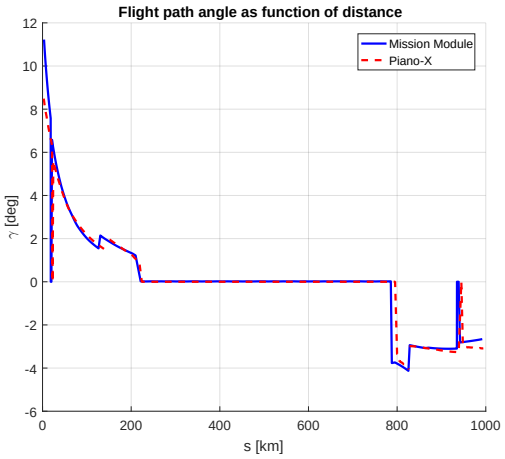

(b) Flight path angle as function of flight distance

Figure 3.29: Validation of the mission module with Piano-X [27]

Figure 3.30a shows the thrust as function of distance. From the figure can be concluded that the thrust of the current model is slightly higher in the climb segments. In the cruise segment, the difference between the two models is approximately 5kN, which may be the results of a higher drag value for the current model

compared to Piano-X. The largest differences are visible in the descent segments. The Piano-X results show zero or even negative thrust in the descent, which is not realistic. The model developed in this study shows a gradual increment in the required thrust. Decreasing in altitude results in a higher maximum thrust available. Because the throttle setting remains at 7%, also the thrust itself increases with decreasing altitude.

Finally, figure 3.30b shows the accumulative fuel consumption as function of the distance. According to the figure, the two lines slightly deviate from each other in the cruise phase. This may be the result of the lower thrust in the Piano-X model. However, also in this figure, the largest differences are visible in the descent phase, which is the result of the higher thrust in the current mission model.

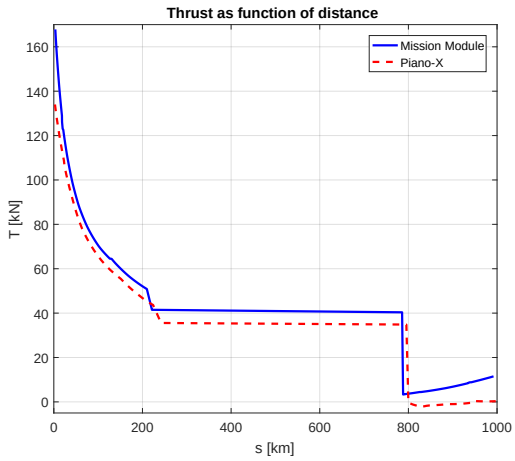

(a) Thrust as function of flight distance

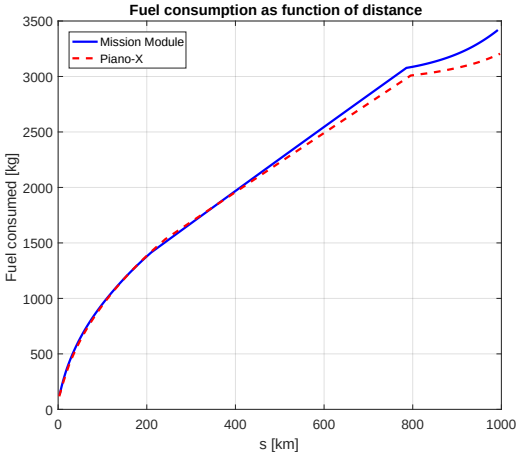

(b) Accumulative fuel consumption as function of flight distance

Figure 3.30: Validation of the mission module with Piano-X [27]

3.9. VALIDATION OF ENTIRE MODEL: OPTIMIZATION OF A320 AT ITS DESIGN POINT

After all the modules are created and validated, the combination of modules is tested to see accurate results are obtained. In order to do this, the baseline A320 as discussed above has been optimized for its fuel efficiency at its design range of 3200km and design payload [29]. The objective of this study was to minimize the fuel over the mission profile. For this optimization, the standard mission profile as indicated in figure 3.27 was used.

Figure 3.31 shows a similar figure as shown above. However, in this EASe, the right side of the aircraft refers to the baseline A320 aircraft, while to left side of the aircraft refers to the optimized A320 aircraft resulting from the optimization using the developed model. In addition, the blueprint of the A320 as obtained from [33] is visible underneath. Table 3.10 gives the most important wing and tail characteristics. As can be seen from both the figure and the table, the optimized configuration shows a slightly smaller wing span and lower sweep angle. This results in a 5.6% lighter wing weight compared to the real A320 aircraft. The aspect ratio of the optimized wing is higher due to the smaller reference area. Finally, it can be seen that the optimized aircraft features a larger tail. The original tail is scaled with a factor 1.2, in order to meet the stability and controllability constraints as explained in the next chapter. Although there are some small differences, the fact that the optimized configurations is close to the actual A320 aircraft is a good indication that the developed model provides accurate results.

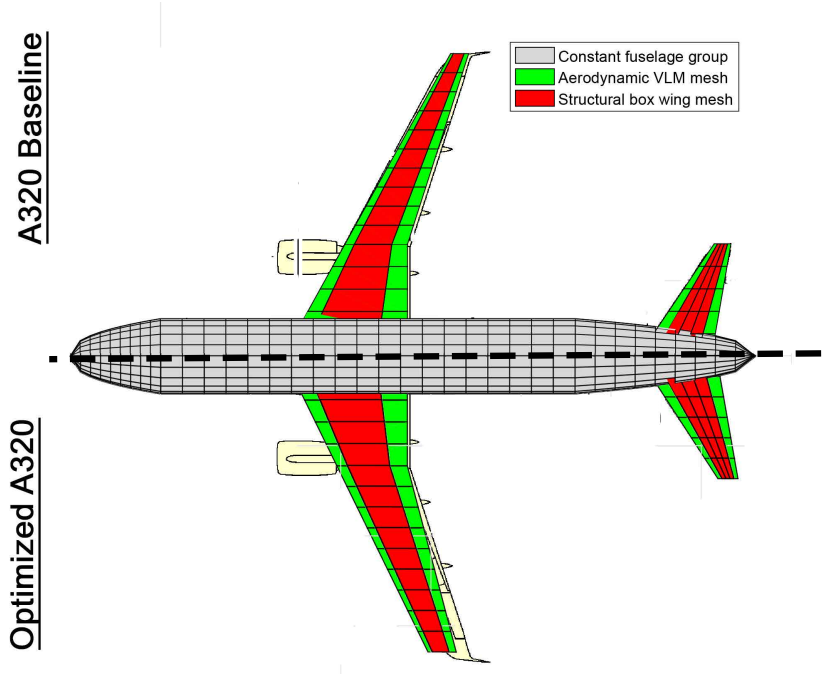

Figure 3.31: Validation of entire model: optimization of the A320 at its design range with design payload. The original A320 aircraft is shown on top, with its optimized version using the developed model at the bottom.

Parameter	**A320 Baseline**	**A320 Optimized**	**Difference [%[**
$M_{wing}[kg]$	8991.12	8420.34	5.59
$S_{ref}[m^2]$	122.40	108.15	13.18
$AR[-]$	9.39	10.08	-6.85
$b_{ref}[m]$	33.91	33.02	2.70
$K_{tail}[-]$	1.00	1.21	-17.36

Table 3.10: Wing and horizontal stabilizer characteristics of the A320 and its optimized variant

4

OPTIMIZATION SET-UP

4.1. CONSIDERED CONFIGURATIONS

In the design optimization studies four different wing geometries are considered: the planar wing, wing with winglet, C-wing, and box wing. In this study, these wing geometries are modelled using 2, 3, 4, and 4 wing segments respectively, as shown in table 4.1. The first two wing segments form the planar part of the wing. For these segments the supercritical RAE2822 airfoil is used. The third segment is the winglet with a symmetrical NACA0012 airfoil. The fourth segment is the inward pointing lifting surface for the C-wing or box wing. For this segment, also the supercritical RAE2822 airfoil has been used. Note that the airfoil of this segment is reversed for the C-wing, such it's creating a negative lift contribution according to to Kroo [51] and as shown in figure 2.14. The first three configurations also feature a horizontal stabilizer with a symmetrical NACA0012 profile to ensure stability and controllability of the aircraft. The box wing has no horizontal tail, instead its longitudinal wing position is varied to ensure stability and controllability.

Table 4.1: Wing segments with their corresponding airfoil for the four different wing geometries

	Wing				Tail
Segment	1	2	3	4	1
Planar	RAE 2822	RAE 2822	-	-	NACA 0012
Winglet	NACA 0012	NACA 0012	NACA 0012	-	NACA 0012
C-wing	RAE 2822	RAE 2822	RAE 2822	Reversed RAE 2822	NACA 0012
Box wing	RAE 2822	RAE 2822	RAE 2822	RAE 2822	-

As discussed in section 3.4, each wing segment is characterized by it's dihedral, leading edge sweep, twist at the beginning, twist at the end, span, and taper. In addition, the root chord of the first wing segment and the tail sizing are considered as design variables. To ensure stability and controllability for the box wing configuration, the longitudinal wing location is added as design variable. This results in $6 \cdot (n_{seg} + 1) + 2$ design variables for the first three configurations, and $6 \cdot (n_{seg}) + 2$ design variables for the box wing configuration. To reduce the computation cost, the following simplifications are made to reduce the number of design variables:

- Because this study is focused on the effects of the wing, it is assumed that the geometric properties of the horizontal stabilizer, i.e. its aspect ratio and taper ratio, remain constant. However, because changes in the wing geometry can affect the controllability and stability of the aircraft, a tail scaling factor is introduced. This scaling factor scales the horizontal stabilizer tail area, while the taper and aspect ratio of remain constant, see equation 4.1. This replaces the 6 design variables of the horizontal stabilizer by 1 scaling factor as design variable.

$$S_{horizontal,tail} = K_{tail} \cdot S_{horizontal,tail_{ref}} \tag{4.1}$$

- The leading edge sweep angles of the first two wing segments, the planar part of the wing, are assumed to be equal. This eliminates the sweep of the second wing segment as design variable.
- The kink location of the planar wing is assumed to be at the same relative spanwise location for all the designs. This eliminates the span of the second wing segment as design variable, since it is directly related to the span of the first wing segment.
- The trailing edge sweep of the first wing segment is assumed to be zero. This allows for effective trailing edge devices near the root of the wing. This eliminates the taper ratio of the first wing segment as design variable.

4.2. DESIGN VARIABLES & BOUNDS

Using the wing parametrization as discussed in section 3.4, in combination with the above mentioned simplifications, the initial designs of the 4 wing configurations are determined. These initial wing planforms are discussed in section 4.2.1. Section 4.2.2 presents the initial mission profiles and its bounds.

4.2.1. GEOMETRICAL AEROSTRUCTURAL

To clearly identify the effects of the addition of non-planar wing surfaces, the initial configurations are chosen such the wing segments that all the configurations have in common, have the same initial design variables. The initial design variables and bounds are shown in table 4.2 for the four configurations.

Table 4.2: Design variables with their initial values and bounds

Nr.	Segment	Symbol	Unit	Description	Planar wing	Winglet	C-wing	Box Wing	LB	UB
X(7)		$K_{h.stab}$	[-]	Tail sizing	1	1	1	-	0.2	2
X(8)	-	X_{wing}	[m]	Long. wing location	(11.8)	(11.8)	(11.8)	11.8	2	14
X(9)		C_r	[m]	Wing root chord	6.89	6.89	6.89	6.89	4	8
X(10)		b_1	[m]	Span	6.2	6.2	6.2	6.2	4	9
X(11)		Λ_1	[deg]	LE Sweep	27	27	27	27	10	45
X(12)		Γ_1	[deg]	Dihedral	5	5	5	5	0	45
-	1	λ_1	[-]	Taper	-	-	-	-	-	-
X(13)		$\epsilon_{begin,1}$	[deg]	Twist begin	5	5	5	5	-8	8
X(14)		$\epsilon_{end,1}$	[deg]	Twist end	0	0	0	0	-8	8
-		b_2	[m]	Span	-	-	-	-	-	-
-		Λ_2	[deg]	LE Sweep	-	-	-	-	-	-
-		Γ_2	[deg]	Dihedral	-	-	-	-	-	-
X(15)	2	λ_2	[-]	Taper	0.35	0.35	0.35	0.35	0.05	1
-		$\epsilon_{begin,2}$	[deg]	Twist begin	-	-	-	-	-	-
X(16)		$\epsilon_{end,2}$	[deg]	Twist end	-3	-3	-3	-3	-8	8
X(17)		b_3	[m]	Span	-	3	3	3	3	5
X(18)		Λ_3	[deg]	LE Sweep	-	45	45	45	10	60
X(19)		Γ_3	[deg]	Dihedral	-	80	80	80	30	120
X(20)	3	λ_3	[-]	Taper	-	1	1	1	0.1	2
X(21)		$\epsilon_{begin,3}$	[deg]	Twist begin	-	0	0	0	-8	8
X(22)		$\epsilon_{end,3}$	[deg]	Twist end	-	0	0	0	-8	8
X(23)		b_4	[m]	Span	-	-	3	-	3	5
X(24)		Λ_4	[deg]	LE Sweep	-	-	38	38	10	60
X(25)		Γ_4	[deg]	Dihedral	-	-	170	170	160	190
X(26)	4	λ_4	[-]	Taper	-	-	2	2	0.5	2.5
X(27)		$\epsilon_{begin,4}$	[deg]	Twist begin	-	-	0	0	-8	8
X(28)		$\epsilon_{end,4}$	[deg]	Twist end	-	-	0	0	-8	8

As mentioned above, some of these variables are assumed to depend on others, and therefore can be omitted from the list. For consistency, all the 6 variables are indicated in the table, however those that depend on other variables are given no value. In addition, the longitudinal wing location, has a fixed value that remains constant in the optimization for the first three configurations, while it is considered as a design variable for the box wing configuration. If the variable remains constant during the optimization, it is indicated using brackets in the table. The lower bounds for the third and fourth wing segments span equals 3 meter,

to make a clear distinction between the various configurations. Small lower bounds for these segments span may result in very small winglets and/or C-wings, which are hard to distinguish from the planar configuration.

Figure 4.1 gives a graphical representation of these four wing configurations. The wing loading as indicated in the figures is obtained at an angle of attack of 3 degrees and a Mach number of 0.78. This gives an indication of the effect of the non-planar wing surfaces on the lift distribution. As can be seen, the C-wings inboard segment produces a small negative lift force, which is in agreement with the literature as described by Kroo [51] and discussed in section 2.1.

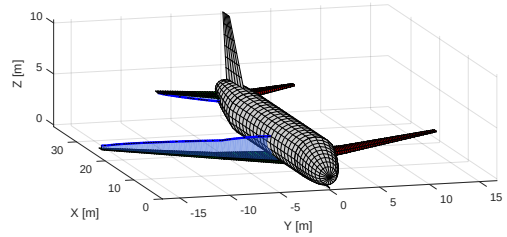

(a) Planar wing

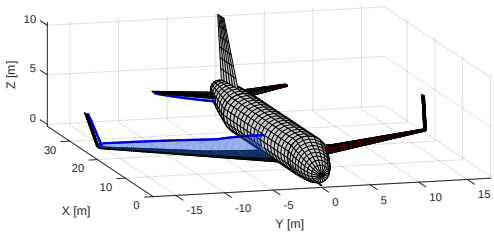

(b) Wing with winglet

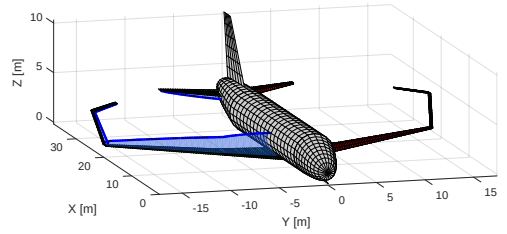

(c) C-wing

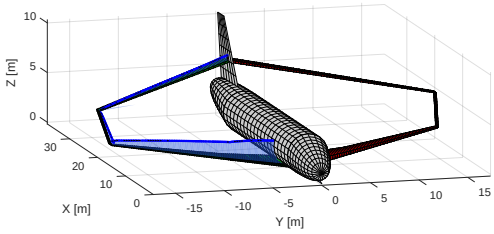

(d) Box wing

Figure 4.1: Initial wing configurations

4.2.2. MISSION

In addition to the wing configurations as discussed above, also mission optimization is performed to identify the effect of the cost factor on the mission profile. Because the main focus of this study is to identify how changes in the climb and descent strategy affect the mission and optimized planforms, the cruise conditions, i.e. cruise Mach number and cruise altitude, remain constant in the mission optimization. In addition, the initial climb speed (segment 1) and final descent speed (segment 11) are also fixed in the optimization to provide each mission with the same boundary conditions. At short range missions, the effect of the low speed mission segments is relative large. Therefore a short range mission of 600km is optimized to clearly identity the effects of the different climb and descent strategies on the most optimal wing configurations. According to figure 3.3, the 600km missions occur relative often.

As starting point for the mission optimization, the standard climb, cruise, and decent profiles for the A320 family are used. As discussed in section 3.8, the climb and decent segments of a mission are operated at two constant CAS and a constant Mach number. For the A320 family, typical numbers for these segments are 250 kts and 300 kts for the constant CAS parts, and Mach 0.78 for the constant Mach part, see figures 4.2a and

4.2b [48].

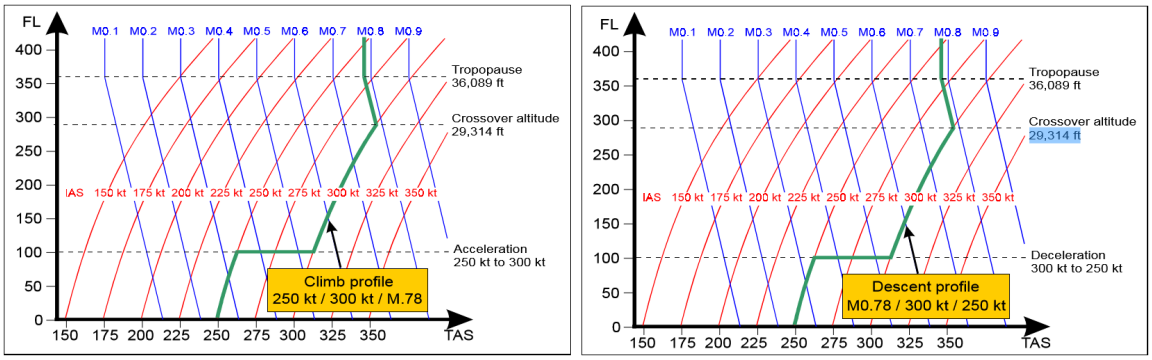

(a) A320 standard climb profile

(b) A320 standard decent profile

Figure 4.2: A320 standard climb and decent profiles [48].

The upper bounds for the optimization are given by the maximum operating speed V_{MO}/M_{MO} of 350 kts and Mach 0.82 respectively [33]. The lower bounds are given a conservative low value to give the optimizer a high design freedom. In practice, these lower bounds may be out of the flight envelope, so these values may seem unrealistic low. However, stall constraints, as will be explained in section 4.3, are also covered in the optimizations and the lower bounds of the flight envelope.

Table 4.3 shows the initial mission variables and their respective bounds as used in the mission optimization

Table 4.3: Mission profile design variables with their corresponding bounds

Phase	Parameter	Initial	Lower bound	Upper bound	Unit
Climb	$h_{accelerate}$	10000	6000	14000	[ft]
	CAS segm. 3	300	150	350	[kts]
	ToC Mach	0.78	0.65	0.78	[-]
Descent	ToD Mach	0.78	0.65	0.78	[-]
	$h_{decelerate}$	10000	6000	14000	[ft]
	CAS segm. 9	300	150	350	[kts]

4.3. CONSTRAINTS

To obtain feasible results, a number of constraints are considered:

- Stall constraint
  A constraint on stall speed is important when optimizing the planform geometry. Without this constraint, optimization often leads to unrealistically small tip chords with high section lift coefficients [14]. The stall speed is determined using equation 4.2.

$$V_{stall} = \sqrt{\frac{2L}{\rho S_{ref} C_{L,max}}} \tag{4.2}$$

  In this equation, L refers to the lift, ρ to the density, S_{ref} to the reference area, and $C_{L,max}$ to the maximum lift coefficient. The stall speed is assumed to remain constant and equal to that of the baseline A320 aircraft. This allows to rewrite equation 4.2 to equation 4.3 to determine the maximum lift coefficient of the to be optimized planform:

$$C_{L,max} = \left(\frac{W}{S \cdot C_{L,max}}\right)_{|A320} \cdot \frac{S}{W} \tag{4.3}$$

Where it is assumed that the lift equals the weight of the aircraft. Subsequently, the wing is analyzed at this maximum lift coefficient by AVL to determine the sectional lift coefficients of the wing, as explained in section 3.5. This constraint requires that all the sectional lift coefficients must be less or equal to the maximum lift coefficient of the airfoil $C_{l,max}$:

$$C_{l|C_{L,max}} \leq C_{l,max} \tag{4.4}$$

The airfoil maximum lift coefficient varies with Reynolds number. However, in this study the maximum sectional lift coefficient is assumed to be constant and equal to 1.4 and 1.45, for the RAE2822 and NACA0012 airfoil [37].

- Fuel volume constraint
  To ensure that the required block fuel fits in the wing, a volume constraint is imposed on the designs, such that the required fuel volume is smaller or equal to the available tank volume:

$$V_{fuel,required} \leq V_{tank,available} \tag{4.5}$$

In which the required volume $V_{tank,required}$ is determined according to:

$$V_{tank,required} = m_{fuel,required} \cdot \rho_{fuel} \tag{4.6}$$

The available tank volume is the combined volume of wing and tail. The tank volume is defined as the volume within the structural wing box, ranging from the root to 85% of the wing semi-span.

- Stability constraint
  Stability of the aircraft has to be ensured in all the flight conditions. However, optimizing for stability in all the flight conditions involves the sizing and deflection of the elevator, which is considered out the scope of this research. Instead, it is assumed that the elevator is not deflected in the cruise phase, to minimize the drag. Therefore the stability of the planforms is assessed based on a zero elevator deflection in cruise conditions. Because the stability depends on the weight distribution of the aircraft, which varies during a flight as fuel is consumed, the stability is evaluated at the beginning and at the end of the cruise phase. It is assumed that the static margin must be at least 5% [8], which leads to the following constraint:

$$0.05 - K_n \leq 0 \tag{4.7}$$

Where K_n is defined according to equation 4.8 [8]. The two stability derivates in this equation C_{M_α} and C_{L_α} are obtained from AVL under the considered flight conditions at the beginning and end of the cruise phase.

$$K_n = -\frac{C_{M_\alpha}}{C_{L_\alpha}} \tag{4.8}$$

- Controllability constraint
  Analogue to the stability constraint, also the controllability depends on the weight distribution of the aircraft. Therefore, also the controllability is evaluated at the start and at the end of the cruise phase. A positive moment around the center of gravity is required to be controllable and to be able to perform pitch up manoeuvers [52]. This leads to the following constraint:

$$C_m \geq 0 \tag{4.9}$$

This moment coefficient C_m is directly obtained from AVL at the considered flight conditions.

- Washout constraint
  To prevent tip stall of the aircraft, a constraint is imposed on the wing twist, which forces the optimized designs to have a small washout along the the wing span. This constraint is implemented according to:

$$\epsilon_{tip} \leq \epsilon_{root} \tag{4.10}$$

- Box Wing - fixed wing tip constraint
  For the box wing configuration, the tip of the fourth wing segment is constrained in the structural model. However, this requires that the wing tip of this segment is geometrically attached to the fuselage. Therefore an additional constraint is imposed for the box wing configuration, which enforces the tip of the last segment to coincidence with the fuselage group:

$$d_{min,1} \leq 0 \tag{4.11}$$

$$d_{min,2} \leq 0 \tag{4.12}$$

  Where d_{min} is defined as the minimum distance from the wing tip coordinate to the outer contour of the side view of the fuselage group, as illustrated in figure 4.3. The value of d_{min} is defined positive if the point lies outside the fuselage contours. In the case as illustrated in the figure, both the d_{min} values are positive, so the constraint is not met.

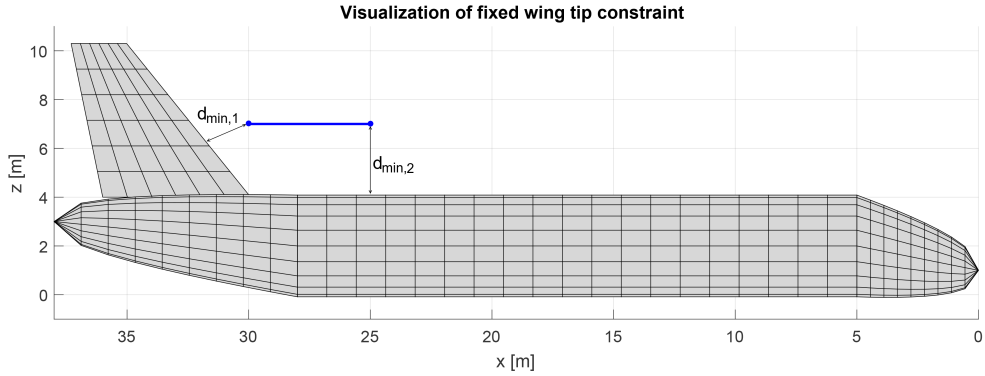

Figure 4.3: Illustration of the wing tip constraint for the box wing; the blue line represents the tip chord of the box wing's fourth wing segment

4.4. OPTIMIZATION SETTINGS

Previous sections discussed the considered design variables and constraints. This section discusses the scaling of the design variables, the used bounds, objective function, and the settings of MATLAB's optimizer *fmincon*.

4.4.1. SCALING OF DESIGN VARIABLES AND BOUNDS

Because the order of magnitude of the various design variables differs, varying with a constant value will significantly affect some design variables, i.e. the taper ratio of a segment (which is typically between 0 and 1), while other design variables are less affected, i.e. the dihedral of a segment (which can take values between 0° and 180°). To make sure that the optimizer equally affects each design variable, these are scaled between 0 and 1, according to equation 4.13.

$$x_0 = \frac{X_0 - LB_0}{UB_0 - LB_0} \tag{4.13}$$

Where:

- x_0 is the scaled design vector
- X_0 is the unscaled design vector
- LB_0 is the unscaled lower bound vector
- UB_0 it the unscaled upper bounds vector

As results, the lower and upper bounds for *fmincon* consist of:

$$LB = [0, 0, 0, ..., 0, 0] \tag{4.14}$$

$$UB = [1, 1, 1, ..., 1, 1] \tag{4.15}$$

4.4.2. OBJECTIVE FUNCTION

The developed model can analyze the effect of the cost factor on the block fuel and the block time. In order to make sure that both factors affect the objective function more or less equally, these values are normalized w.r.t. the block fuel and block time of the conventional A320 configuration with the standard mission profile, see equation 4.16. By increasing the cost factor k_{cost}, which can take values between 0 and 1, the optimizer gradually focuses more on reducing the block time than reducing the fuel consumption.

$$J_{obj} = (1 - k_{cost}) \cdot \frac{m_{fuel}}{m_{fuel_0}} + k_{cost} \cdot \frac{t_{block}}{t_{block_0}} \tag{4.16}$$

4.4.3. *Fmincon* SETTINGS

In addition to the design variables and the objective function, also the settings for the gradient based solver *fmincon* affect the final solution. Table 4.4 summarizes the used settings for the optimization studies. As optimization method, Sequential quadratic programming has been used. The optimization is considered to be converged if the first order optimality is smaller than 0.01. The *DiffMinChange* parameter describes the stepsize the optimizer takes in order to estimate the gradient. Since the design variables are scaled, this equals 2%. To obtain proper results, the gradient based optimizer requires a smooth objective and smooth constraint functions. By taking smaller derivative steps, the function becomes gradually more irregular due to the internal optimizations, which would results in wrong gradient estimations.

Table 4.4: MATLAB *Fmincon* function optimization settings

Parameter	Value
Algorithm	SQP
Optimality Tolerance	0.01
TolX	1.00E-04
DiffMinChange	0.02
TolCon	1.00E-04

4.5. OVERVIEW OF THE CONSIDERED OPTIMIZATION STUDIES

With the developed model, the mission and/or the four wing configurations can be optimized. This section gives an overview of the different studies and different cases that are considered. The next chapter presents the results of these different optimization studies.

First two mission optimizations are performed using a fixed wing design: a mission optimization with the goal to minimize the block fuel and an optimization with the goal to minimize the flight time, which leads to $k_{cost} = 0$ and $k_{cost} = 1$ in equation 4.16 respectively. To clearly identify the effect of the climb and descent

segments, the cruise altitude and cruise Mach number remain fixed throughout the optimizations. Also the initial climb and final descent flight speeds remain fixed to account for an equal kinetic and potential energy at the start and end of the mission. Finally, during this mission optimization, the aircraft geometry remains constant and equal to that of the baseline A320.

For the two resulting mission profiles, the four wing configurations, planar wing, winglet, C-wing, and box wing are optimized. In this case the mission profiles remain constant, and the wing and tail geometry are optimized for the minimum block fuel. So this results in a total of 8 wing configuration optimization studies.

Finally, the effect of changes in the cruise length and cruise Mach number are identified. This is not an optimization study. Instead, the cruise length and cruise Mach numbers of the four wing configurations are varied, and the results are analyzed. In this study, the optimized wing designs remain constant. Also, the climb and descent segments of the mission are fixed.

Table 4.5 summarizes the studies to give an clear overview. In addition, figure 4.4 provides a schematic overview of the different studies. Also, it shows how these three studies are related to each other. The next chapter discusses the results of each of these studies.

Table 4.5: Overview of the considered (optimization) studies using the developed model

Study	Case	Opt. Objective		Design variables			Planform					Mission profile	
		Min fuel	Min time	Climb & Descent	Cruise	Wing & Tail	A320	Planar	Winglet	C-Wing	Box wing	Fuel economy	Minimum time
1	1	X		X			X						-
	2		X	X			X						-
2	1	X				X		X				X	
	2	X				X		X					X
	3	X				X			X			X	
	4	X				X			X				X
	5	X				X				X		X	
	6	X				X				X			X
	7	X				X					X	X	
	8	X				X					X		X
3	1		-		X			X				X	
	2		-		X				X			X	
	3		-		X					X		X	
	4		-		X						X	X	

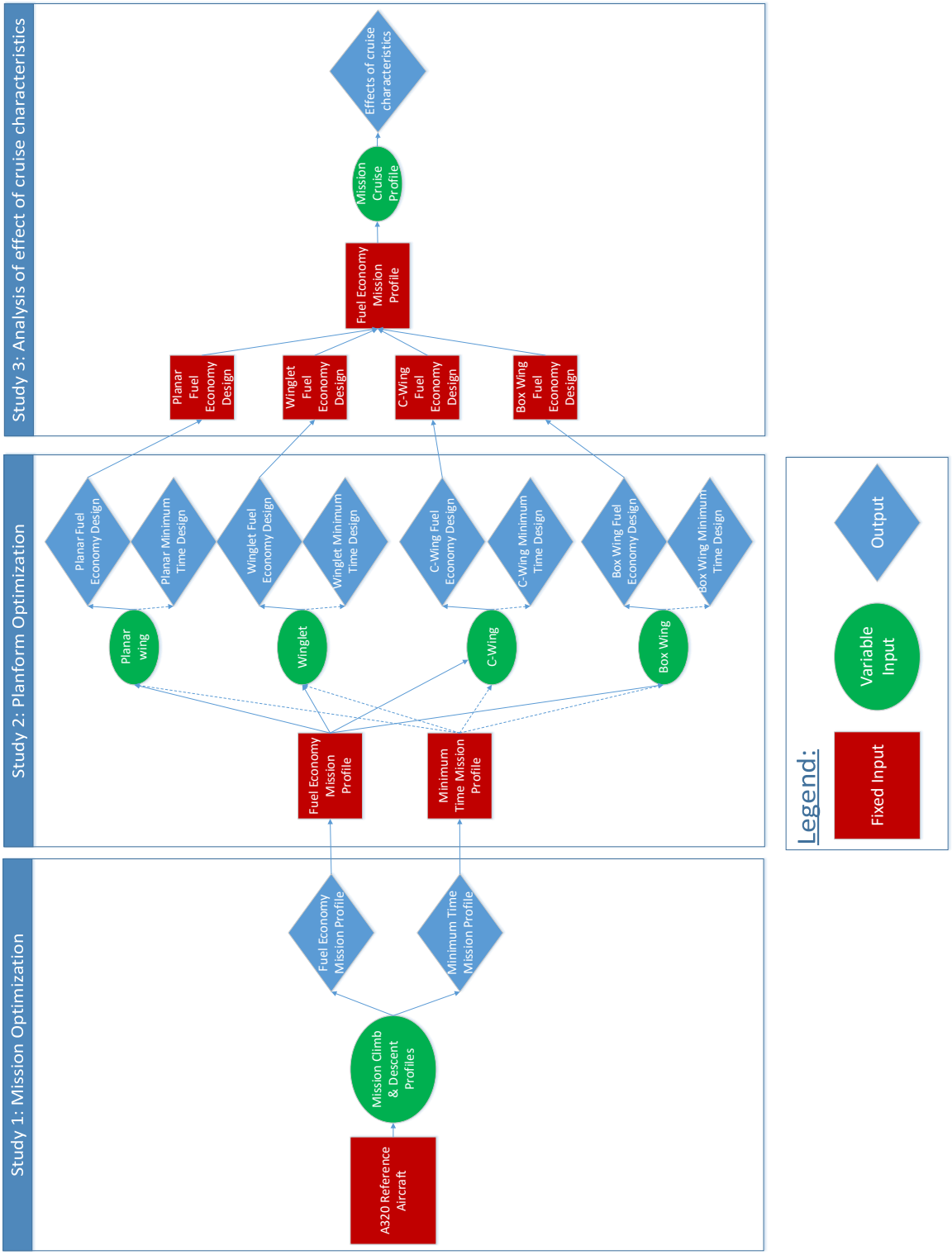

Figure 4.4: Schematic overview of the performed (optimization) studies

5

RESULTS

This chapter presents and discusses the results as obtained from the various optimization studies as given in table 4.5. Section 5.1 provides the results of the mission optimization studies leading to the 'fuel economy mission profile' and the 'minimum time mission profile' respectively. Section 5.2 discusses the differences in the wing designs as result of the design optimizations for the two different mission profiles respectively. In this section the effects of variation in the climb and descent strategies, on the most optimal design is analyzed, for each of the four wing configurations. Section 5.3 uses these optimized designs to analyze the differences between the four configurations. Finally, section 5.4 discusses the effect of varying the cruise characteristics on the fuel efficiency of the four configurations.

5.1. EFFECT OF THE COST FACTOR ON MISSION PROFILE

In order to analyze the effect of the cost factor on the optimal wing configuration, two different mission profiles are established for a cost factor of zero and one respectively. From this point on, these missions are being referred to as the 'fuel economy mission' and the 'minimum time mission' respectively. In this mission optimization, the reference A320 baseline aircraft has been used, which remains constant during this analysis. The mission profile, which is characterized by the different flight speeds and altitudes is optimized for the most fuel efficient or fastest mission respectively. Finally, the initial ($V_{EAS,1}$) and final ($V_{EAS,11}$) flights speeds remain constant to prevent infeasible high flight speeds at 1500ft, which may cause problems during the final descent and landing phase, which is not considered in this mission profile.

To clearly identify the effect of the low speed mission segments, i.e. the climb and descent phases, only these mission variables are varied in this optimization. So the cruise Mach number and cruise altitude remain constant. The remaining design variables are the two climb speeds ($V_{EAS,2}$ and M_4), the two decent speeds (M_8 and $V_{EAS,9}$), and the two altitudes at which the aircraft accelerates and decelerates from one to the other calibrated airspeed. The initial values and corresponding bounds are discussed in section 4.2.2.

Figures 5.1 and 5.2 show the results of this optimization study. Figure 5.1 shows the altitude as function of the distance. It can be seen that the most fuel efficient mission profile (for $k_{cost} = 0$) climbs faster to the cruise altitude and starts relatively early with its descent. The minimum time mission has a smaller flight path angle in the climb phase. This allows the aircraft to cover some more distance while climbing to cruise altitude. Finally, it can be seen that the aircraft remains longer in the cruise phase, to cover as much distance as possible at a high Mach number. Finally, a steep descent is required at the end of the mission.

Figure 5.2 shows the altitude as function of time. According to the figure, there is no large difference in climbing time between the two mission profiles. The main time profits are obtained in the decent phase. For the most fuel efficient mission profile, this phase covers almost half of the total block time. The minimum time mission profile shows a steep descent at which the most time profits are obtained.

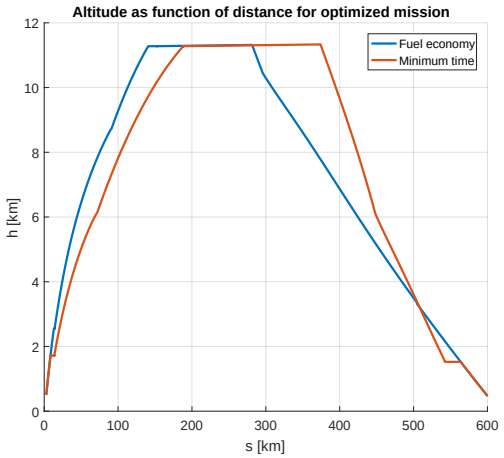

Figure 5.1: Altitude as function of flight distance for the optimized mission profiles

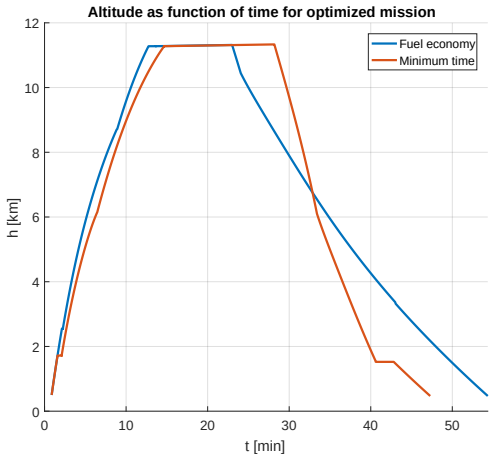

Figure 5.2: Altitude as function of flight time for the optimized mission profiles

Table 5.1 shows the fuel consumed and block time required for both mission profiles. Also, the relative profits are indicated. The fuel economy mission profile results in 209kg fuel savings but at the cost of 7 minutes longer flight time, which corresponds to 7% cost savings at the cost of 15% longer flight time.

Parameter	Unit	Fuel economy	Minimum time	Difference [%]
$F_{consumed}$	$[kg]$	2786.01	2994.48	-6.96
t_{block}	$[min]$	54.35	47.29	14.93

Table 5.1: Objective values of the two optimized mission profiles

Table 5.2 shows the mission profile parameters of both missions. From this table can be concluded that the fuel economy mission profile climbs at a lower calibrated airspeed of 271 kts compared to the minimum time mission profile, which climbs at the maximum allowed flight speed of 350 kts, which equals the V_{MO}. Also, the top of climb Mach number (M_4) is lower for the fuel economy mission profile. The cruise conditions are equal as discussed above. The Mach numbers at top of descent (M_8) are approximately equal to the cruise Mach number for both profiles. Finally, a large difference can be found in the constant EAS airspeeds. The fuel economy mission profile flight speed in this segments equals the flight speed of the final segment of 250 kts. For the minimum time mission profile, the flight speed again equals the V_{MO} of the aircraft.

Parameter	Unit	Fuel economy	Minimum time	Difference [%]
$V_{CAS,1}$	$[m/s]$	250.00	250.00	0.00
h_2	$[m]$	8370.00	5640.00	48.40
$V_{CAS,3}$	$[m/s]$	271.50	350.00	-22.43
M_4	$[-]$	0.73	0.78	-6.90
M_6	$[-]$	0.78	0.78	0.00
h_6	$[m]$	11277.60	11277.60	0.00
M_8	$[-]$	0.77	0.78	-1.17
$V_{CAS,9}$	$[m/s]$	250.00	350.00	-28.57
h_{10}	$[m]$	10890.00	5000.00	117.80
$V_{CAS,11}$	$[m/s]$	250.00	250.00	0.00

Table 5.2: Mission characteristics of the two optimized mission profiles

Figures 5.3 and 5.4 show the L/D ratio and the ratio between the induced drag and the total drag during the mission for both profiles respectively. From figure 5.3 can be seen that the L/D ratio of the fuel economy mission is higher for the non-cruise segments, while for the high minimum time mission, this ratio is lower in the non-cruise segments. In the cruise phase the L/D ratio for both missions is equal due to the equal

flight conditions. From figure 5.4 can be concluded that the the induced drag contribution to the total drag deviates from the cruise conditions. For the fuel economy mission, this ratio is up to 10% higher compared to the cruise conditions. For the minimum time mission this ratio is reduced with 15% in the climb and descent phases. This is due to the higher flight speeds in these segments, which allows for a lower lift coefficient, and thus a lower induced drag. On the other hand, a higher flight speed results in a higher parasitic drag.

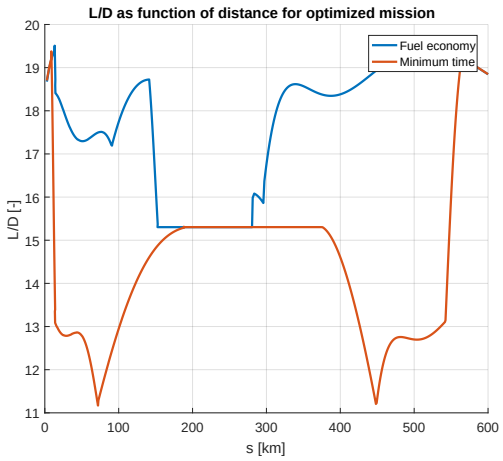

Figure 5.3: L/D as function of flight distance for the optimized mission profiles

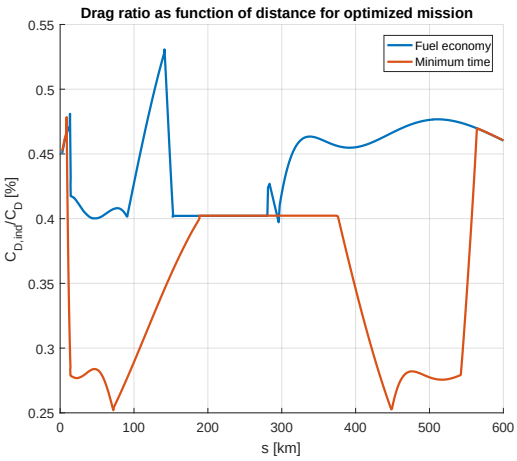

Figure 5.4: Induced drag contribution as function of flight distance for the optimized mission profiles

Finally, figures 5.5 and 5.6 shows the thrust and cumulative fuel consumption for both missions. It can be seen that the thrust in the initial climb phase is relatively high, and gradually reduces, which is the result of the lower density and lower pressure at higher altitudes. In the cruise phase, the thrust remains constant, and in the decent phase only very low thrust is required. The fuel consumption is a function of the thrust and the specific fuel constant (SFC). Due to the high thrust in the climb segment, the cumulative fuel consumption shows a steep gradient. In the cruise phase, this gradient remains constant due to the constant thrust and constant SFC. Finally, in the decent phase the gradient is only slightly lower, which is the result of the required lower thrust, but a high SFC, as discussed in section 3.7.

If the cumulative fuel consumptions of both missions is compared, it can be seen that the largest reductions in terms fuel consumption for the fuel economy mission are obtained due to the early start of the decent phase, in which less thrust is required.

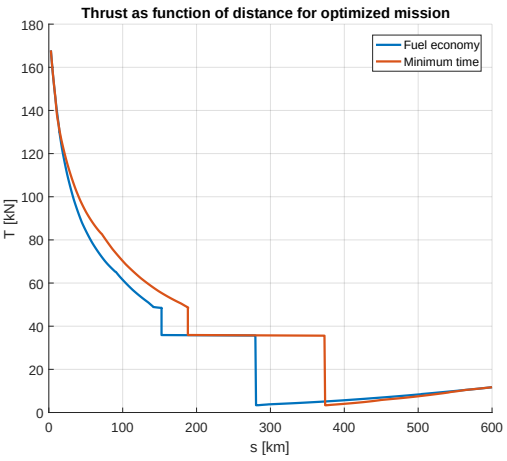

Figure 5.5: Thrust as function of flight distance for the optimized mission profiles

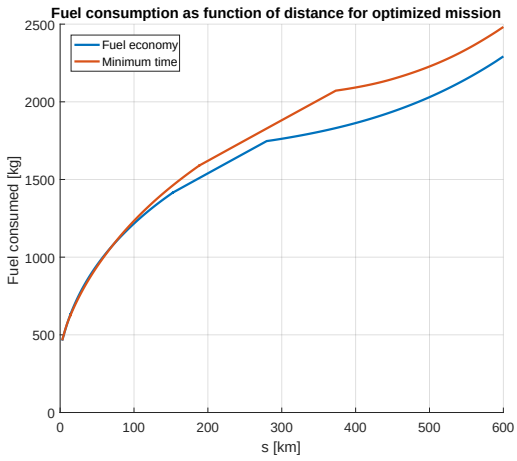

Figure 5.6: cumulative fuel consumption as function of flight distance for the optimized mission profiles

5.2. EFFECT OF COST FACTOR ON OPTIMIZED WING DESIGNS

For the two resulting mission profiles as presented in the previous section, the four wing configurations are optimized for minimum fuel consumption. The configuration that is optimized for the fuel economy mission profile is referred to as the 'fuel economy design', while the configurations that is optimized for the minimum time mission is referred to as the 'minimum time design'. This section presents the aerodynamics, structures, and performance of the four configurations. The differences between the most optimal designs for the two mission are discussed. Section 5.2.1 presents the planar configuration, section 5.2.2 the wing with winglet configuration, section 5.2.3 the C-wing configuration, and finally section 5.2.4 the box wing configuration.

5.2.1. PLANAR WING CONFIGURATION

Figure 5.7 shows the two optimized planar aircraft configurations for the fuel economy mission profile (top) and the minimum time mission profile (bottom). Figure 5.8 compares the wing geometries from a top view. It can be seen that the wing span of the minimum time design is 2m smaller. Also, the sweep and root chord of this design are higher compared to the fuel economy design. It can be seen that the aspect ratio (AR) of the minimum time design is smaller. These geometric values are also summarized in table 5.3. In addition, the relative differences between the two designs are shown. This is the result of the different climb and descent strategies. The parasitic drag component becomes more significant at high flight speeds. Therefore it's favorable to have a smaller wetted area. Also, the wave drag becomes more significant at these transonic conditions, making a more swept wing more beneficial.

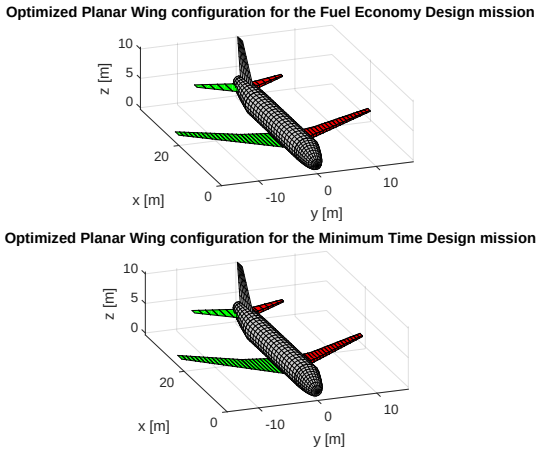

Figure 5.7: Optimized planar wing configurations

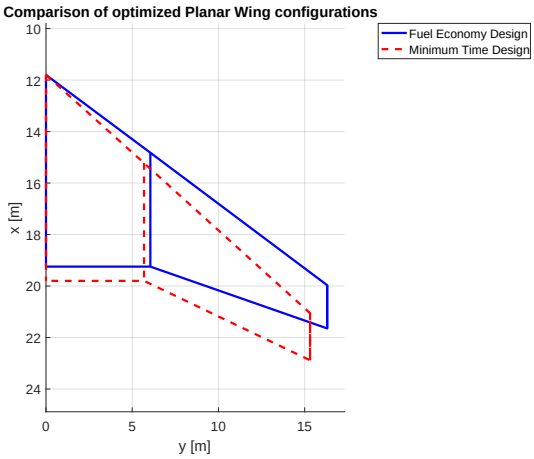

Figure 5.8: Comparison of the planar wing designs

In addition to the geometric differences between the planar designs, their wing weight and mission characteristics are summarized in table 5.3. As can be seen in the table, the wing of the minimum time design is slightly lower. If a fuel economy mission is flown with its optimized design, 2.6% fuel is saved w.r.t. the minimum time mission. However, this requires a 8 minutes longer flight time, which equals 16.2% of the total time. The wing span of the fuel economy design is 6.5% larger, which leads to lower induced drag. However, the Oswald factor in cruise conditions is slightly lower for this configuration, which in its turn may lead to a higher induced drag.

Parameter	Unit	Fuel economy	Minimum time	Difference [%]
$F_{consumed}$	$[kg]$	2672.58	2744.64	-2.63
t_{block}	$[min]$	55.20	47.50	16.21
M_{wing}	$[kg]$	6552.00	6542.00	0.15
S_{ref}	$[m^2]$	134.05	132.75	0.98
S_{wetted}	$[m^2]$	269.12	266.52	0.98
b_{ref}	$[m]$	32.62	30.64	6.46
AR	$[-]$	7.94	7.07	12.31
e_{cruise}	$[-]$	0.97	0.98	-1.02

Table 5.3: Mission and planform characteristics of the optimized planar wing configurations

To see what the wing mass is based on, a more detailed view of the thickness distribution of the wing designs is given in figure 5.9. The top figure shows the skin thickness distribution, while the lower figure shows the width of the booms. It can be seen that both the skins and the booms are slightly thicker in the kink area for the minimum time design.

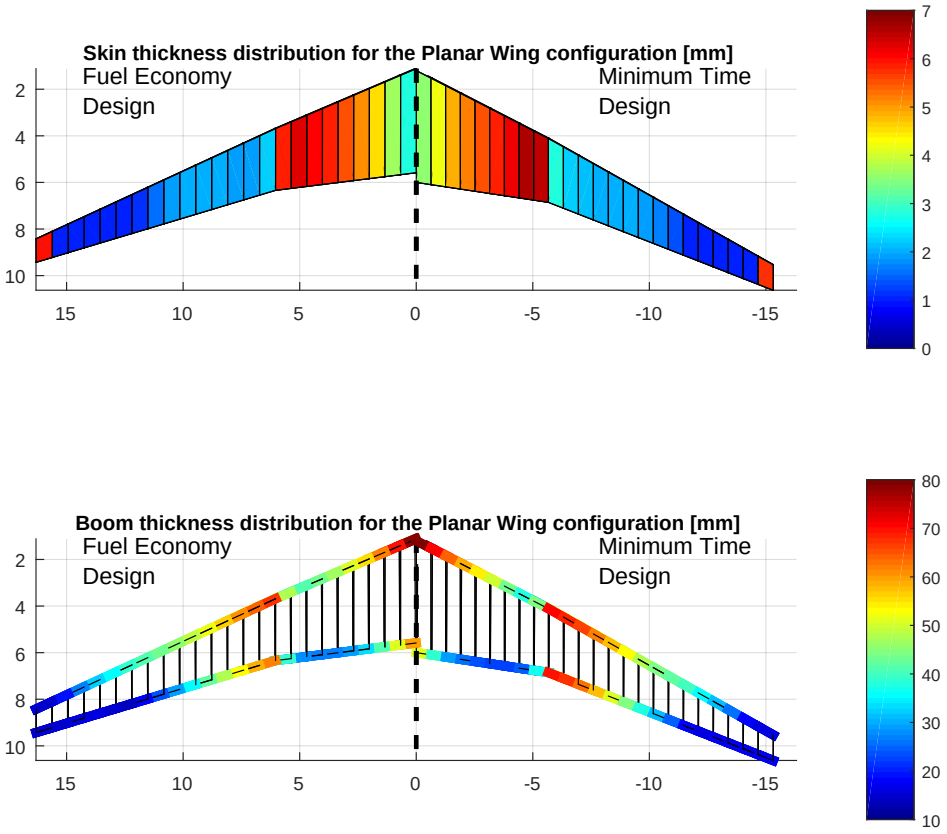

Figure 5.9: Optimal thickness distribution of the optimized planar wing configurations

The aerodynamic performance of the aircraft depends on its flight conditions. In order to compare the lift distribution over the wing for both planar configurations, these distributions are compared at the cruise conditions of the two configurations respectively. Figure 5.10 shows the lift coefficient distribution as function of the semi-wing span. The minimum time design shows slightly higher sectional lift coefficients between 4m

and 12m of the semi-wing span. At the wing root, the fuel economy design has a slightly higher lift coefficient.

If the $c \cdot c_l$ distribution is considered in figure 5.11, some different effects are visible. Because the total lift to be generated is more or less equal for both wings, the surface below the both graphs should be equal. Because the fuel economy design has a smaller wing span, a higher lift is required in the root section to compensate for this.

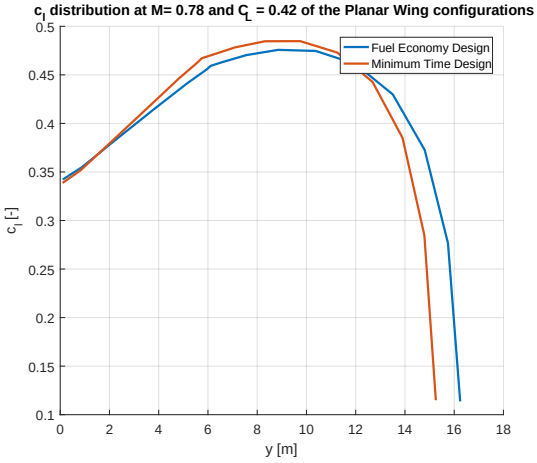

Figure 5.10: Lift coefficient distribution of the optimized planar wing configurations

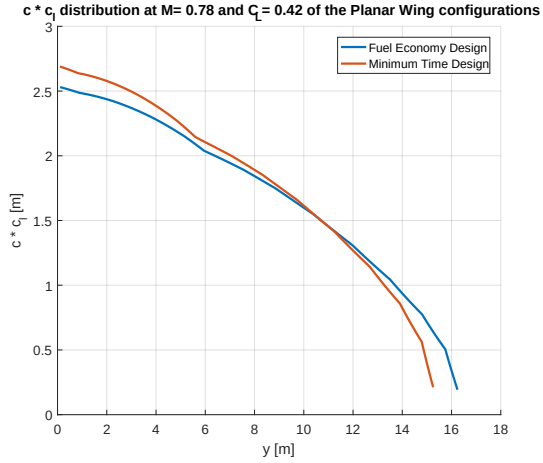

Figure 5.11: Lift distribution of the optimized planar wing configurations

As mentioned above, the lift and drag coefficients strongly depend on the flight conditions. Because an entire mission analysis is considered in this study, in which different flight conditions are evaluated, the effect of the Mach number on the lift and drag is analyzed. Figure 5.12 shows the parasitic drag, induced drag, and total drag as function of the Mach number. These results are obtained using the cruise conditions, i.e. at a cruise altitude of 11km and the corresponding aircrafts mass halfway the cruise phase. Subsequently, the total lift is assumed to equal the weight. This figure is in agreement with the theory as discussed in section 2.1: The induced drag decreases with Mach number, while the parasitic drag increases with Mach number. The total drag is the summation of both drag components.

As can be seen in the figure, the induced drag of the fuel economy design is lower compared to the minimum time optimized design in the entire Mach range. The induced drag is a function of the wing span and Oswald factor, as shown in equation 2.1. As mentioned above, the Oswald factor for the fuel economy design is slightly lower. However, the longer wingspan compensates for this in terms of induced drag reduction. The parasitic drag component is more or less equal up to a Mach number of 0.7. From this point on, the fuel economy design shows a significant increment in parasitic drag compared to the minimum time design. This is the direct effect of the larger wing sweep of the minimum time design, keeping the wave drag relative low. If the total drag is considered, it can be concluded that the fuel economy design minimal drag Mach number lies around Mach 0.73, while for the minimum time design this minimum drag Mach number is approximately 0.75. The minimum time optimized aircraft flies at higher Mach numbers in the climb and descent phases. Therefore it is expected that this optimized configuration has its minimum drag Mach number shifted to a higher Mach number compared to the fuel economy design.

A similar effect is visible in figure 5.13. This figure shows the lift drag polars for a range of Mach numbers. As can be seen in the figure, the drag coefficient C_D of the fuel economy design is lower for a given lift coefficient C_L at Mach numbers below 0.75. At higher Mach numbers, the minimum time optimized design shows lower drag coefficients.

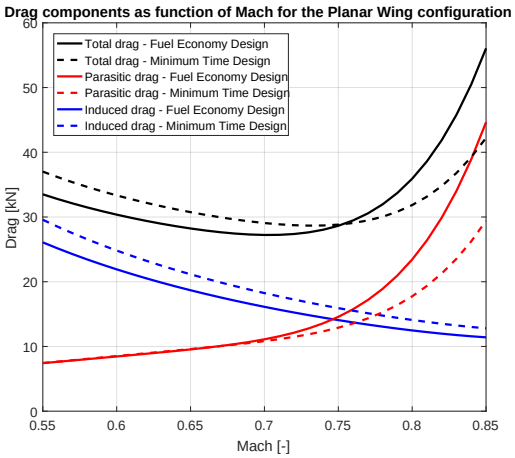

Figure 5.12: Drag components as function of Mach for optimized planar wing configurations

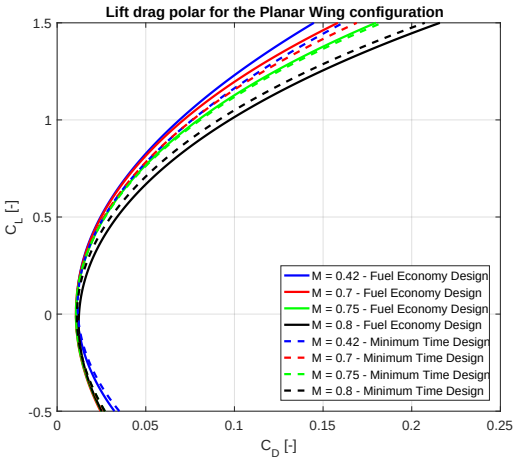

Figure 5.13: Lift drag polars as function of Mach for optimized planar wing configurations

5.2.2. WING WITH WINGLET CONFIGURATION

Figure 5.14 shows the optimized winglet configurations for the fuel economy mission profile (top) and the minimum time mission profile (bottom). To better visualize the differences, the designs are plotted on top of each other in figure 5.15. Similar to the planar configuration, the wing span of the minimum time design is smaller with an increased sweep angle. Remarkable is that the length of the winglet segment is slightly larger for this design, which results in an increased parasitic drag, which may have an detrimental effect of at high flight speeds. However, the total wetted area of the minimum time design is 2.1% lower compared to the fuel economy design, which would lead to a lower friction drag. Finally, the Oswald factors in the cruise conditions are shown in table 5.4. It can be seen that the minimum time design features a 3.5% higher Oswald factor. If these cruise Oswald factors are compared to those of the planar configuration, it can be seen that the winglet configurations have an Oswald factor that is approximately 0.1 to 0.15 higher compared to the planar configurations.

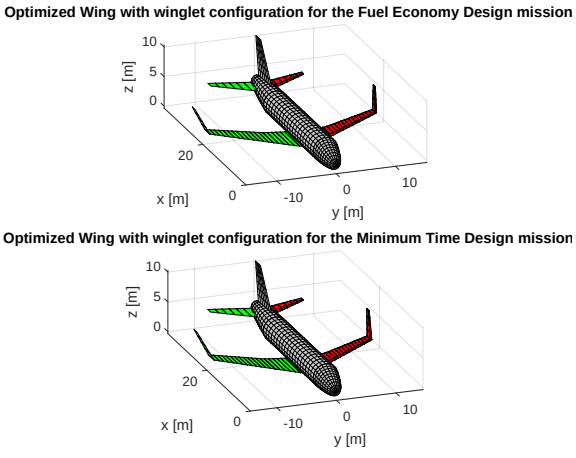

Figure 5.14: Optimized wing with winglet configurations

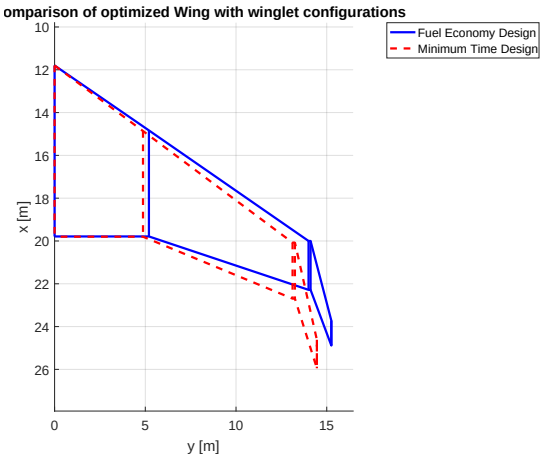

Figure 5.15: Comparison of the wing with winglet designs

Table 5.4 shows the differences in wing weight and mission characteristics for the winglet configuration. The minimum time design is approximately 150kg lighter, which equals 2.6% of the total wing mass. The total fuel consumed is 2.3% less for the fuel economy design, at the cost of a 7.5 minutes longer flight time.

Parameter	Unit	Fuel economy	Minimum time	Difference [%]
$F_{consumed}$	$[kg]$	2628.81	2689.43	-2.25
t_{block}	$[min]$	55.00	47.50	15.79
M_{wing}	$[kg]$	5959.00	5810.00	2.56
S_{ref}	$[m^2]$	135.10	130.52	3.51
S_{wetted}	$[m^2]$	285.82	280.00	2.08
b_{ref}	$[m]$	30.62	29.04	5.44
AR	$[-]$	6.94	6.46	7.43
e_{cruise}	$[-]$	1.10	1.14	-3.51

Table 5.4: Mission and planform characteristics of the optimized wing with winglet configurations

Figure 5.16 shows the thickness distribution of the skin and the booms on the top and bottom respectively. This thickness distribution is very comparable to planar configuration: a relative thick skin is required for the first wing segment (before the kink), after which the skin thickness decreases. If the two winglet design are compared, it can be seen that the minimum time design requires a thicker skin in the kink area, from 4m to 8m of the wing semi-span, to carry the shear stresses. However, at the root of the wing, the fuel economy design requires a thicker skin.

If the booms are considered, the opposite is visible: in the kink area, the booms of the fuel economy design are thicker, while for the minimum time design, the booms in the root section are slightly thicker.

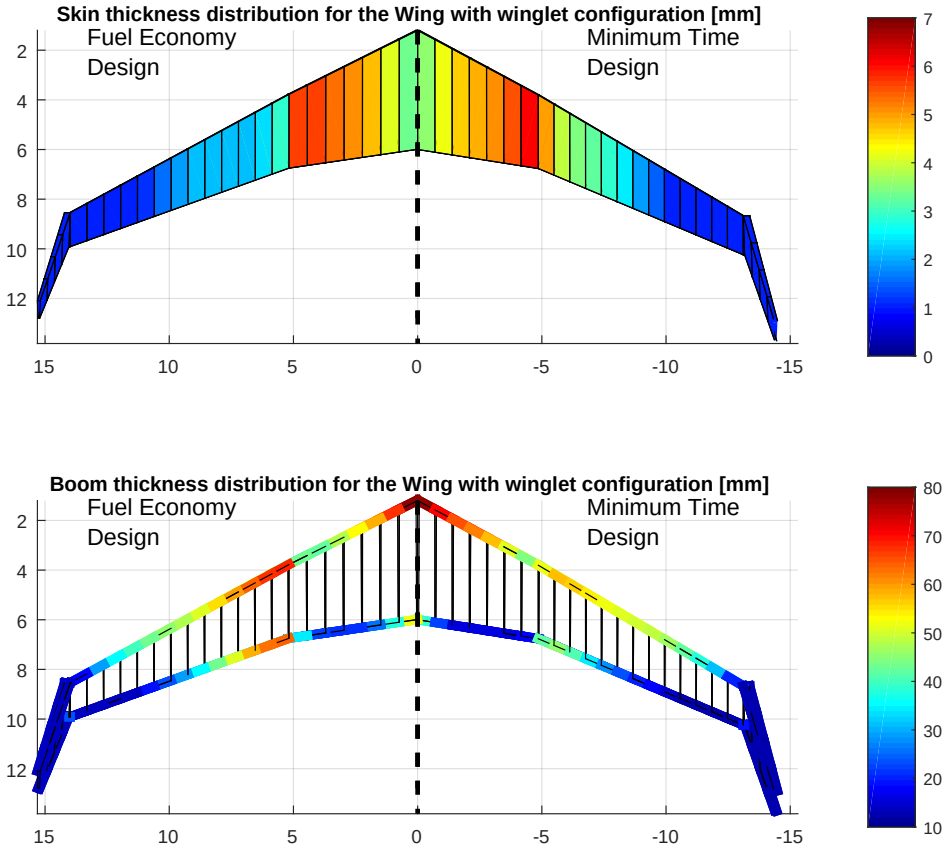

Figure 5.16: Optimal thickness distribution of the optimized wing with winglet configurations

Figure 5.17 shows the lift coefficient distribution of the winglet designs at Mach 0.78. These lift distributions are again obtained at the cruise conditions, in which lift equals weight. From this figure can be concluded that the lift coefficient of the minimum time design is higher over the entire wing span. If this lift coefficient distribution is compared to the planar configuration, it can be seen that the values are approximately the same. However, the winglet allows for a higher sectional lift coefficient in the tip area of the wing.

Figure 5.18 shows the $c \cdot c_l c$ distribution of the winglet designs. Analogue to the planar configurations, the kink in the wing around a semi-wing span of 5m is clearly visible. In this figure is also visible that the winglets produce an inward force, as a positive lift coefficient in this area is defined as pointing inward. Finally, comparing the lift distribution of the two designs, no large differences can be found. The curve for the minimum time design is shifted up, to get an equivalent total amount of lift with a smaller wing span.

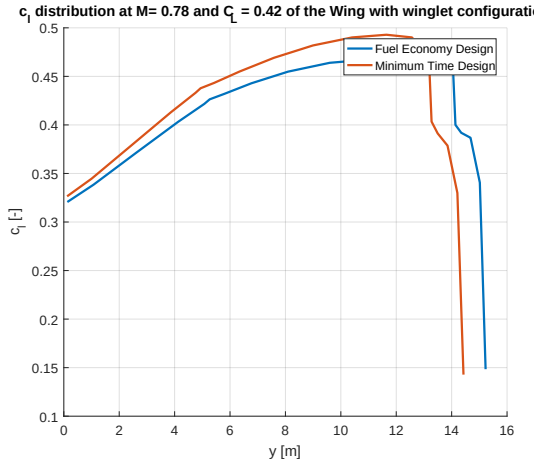

Figure 5.17: Lift coefficient distribution of the optimized wing with winglet configurations

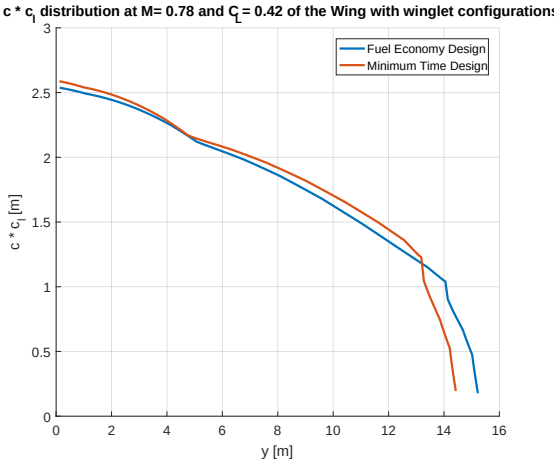

Figure 5.18: Lift distribution of the optimized wing with winglet configurations

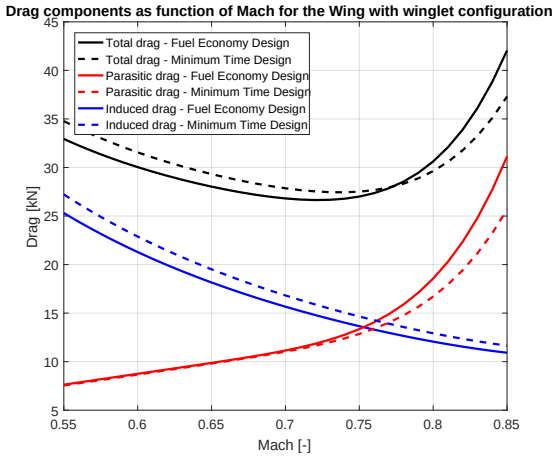

Figure 5.19: Drag components as function of Mach for optimized wing with winglet configurations

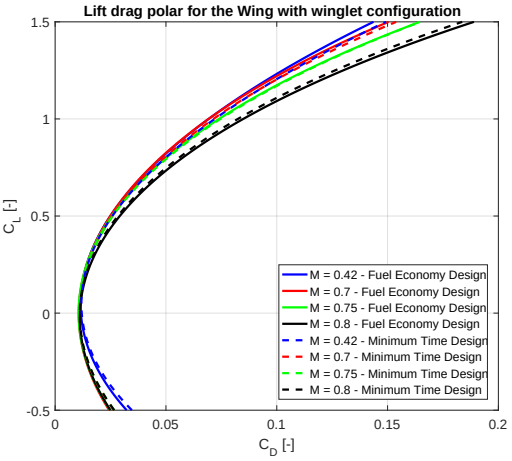

Figure 5.20: Lift drag polars as function of Mach for optimized wing with winglet configurations

Figure 5.19 shows the drag components as function of Mach number. Analogue to the planar configuration, these results are obtained in cruise conditions, i.e. at cruise altitude and the corresponding weight halfway the cruise segment. Also for the winglet configuration, the induced drag is lower for the fuel economy design due to the longer wing span. The parasitic drag lines starts to deviate from Mach 0.75. At higher Mach numbers, the fuel economy design shows a significant higher parasitic drag due its larger wave drag. The minimum drag Mach numbers are 0.73 and 0.75 for the fuel economy design and the minimum time

design respectively.

Figure 5.20 shows the lift drag polars for a series of Mach numbers. For the winglet configuration, the fuel economy design shows lower drag at Mach numbers below a Mach number of 0.76, which corresponds to the intersection of the two total drag curves in figure 5.19. At higher Mach numbers, the minimum time mission shows lower drag coefficients, especially at higher lift coefficients.

5.2.3. C-WING CONFIGURATION

Figure 5.21 shows an isometric view of the optimized designs for the C-wing configurations. Figure 5.22 compares the wing geometries from a top view. Again, it can be seen that the minimum time design has a smaller wing span and higher sweep angle. The wing roots chord lengths are both the same, and equal to the upper bound as used during the optimization. The winglet height (third wing segment span) is larger for the minimum time design. However, the fourth wing segment length is smaller for this configuration. The most important geometrical characteristics of the configurations are summarized in table 5.5. Finally, the Oswald factors in the cruise conditions are shown in the table. It can be seen that the minimum time design features a 7.8% higher Oswald factor. If these cruise Oswald factors are compared to those of the planar configuration, it can be seen that the C-wing designs have an Oswald factor that is approximately 0.25 to 0.3 higher.

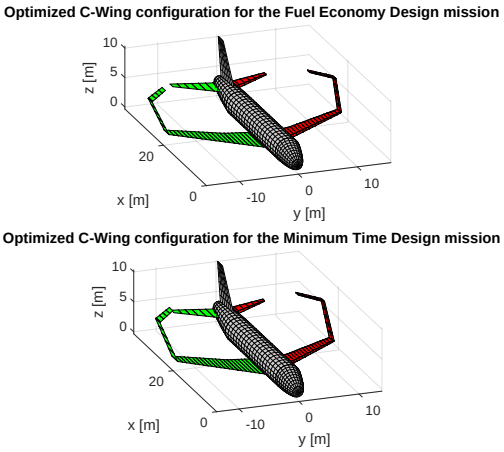

Figure 5.21: Optimized C-wing configurations

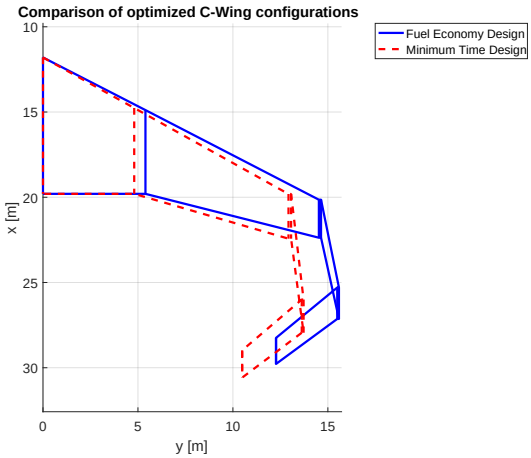

Figure 5.22: Comparison of the C-wing designs

The wing masses for the optimized C-wing designs differ approximately 1000kg, i.e. 15.9% of the total wing mass. This is a significant difference compared to the earlier discussed configurations. The difference in fuel consumption is 2.4% and the difference in flight time is 16.6%. These relative differences in mission characteristics between the two C-wing designs are comparable to the planar and winglet configurations as discussed before.

Parameter	Unit	Fuel economy	Minimum time	Difference [%]
$F_{consumed}$	$[kg]$	2685.98	2751.41	-2.38
t_{block}	$[min]$	55.40	47.50	16.63
M_{wing}	$[kg]$	8197.80	7073.30	15.90
S_{ref}	$[m^2]$	150.41	140.17	7.31
S_{wetted}	$[m^2]$	327.13	316.95	3.21
b_{ref}	$[m]$	31.35	27.64	13.42
AR	$[-]$	6.53	5.45	19.82
e_{cruise}	$[-]$	1.18	1.28	-7.81

Table 5.5: Mission and planform characteristics of the optimized C-wing configurations

Figure 5.23 shows the thickness distribution of the skin and booms of the C-wing designs. According to the figure, there is a substantial difference between the thickness distributions of both optimized designs, which may be the result of different local optima in the Nastran analysis. The fuel economy design shows a thicker skin thickness, especially near the root of the wing. However, the booms for this design are considerable smaller compared to the minimum time design. If this thickness distribution is compared with the previously discussed configurations, it can be seen that a thicker, and thus heavier, structure is required. Especially in the first wing segment, for which the bending moment is the largest, these differences are quite large compared to the planar and winglet configuration.

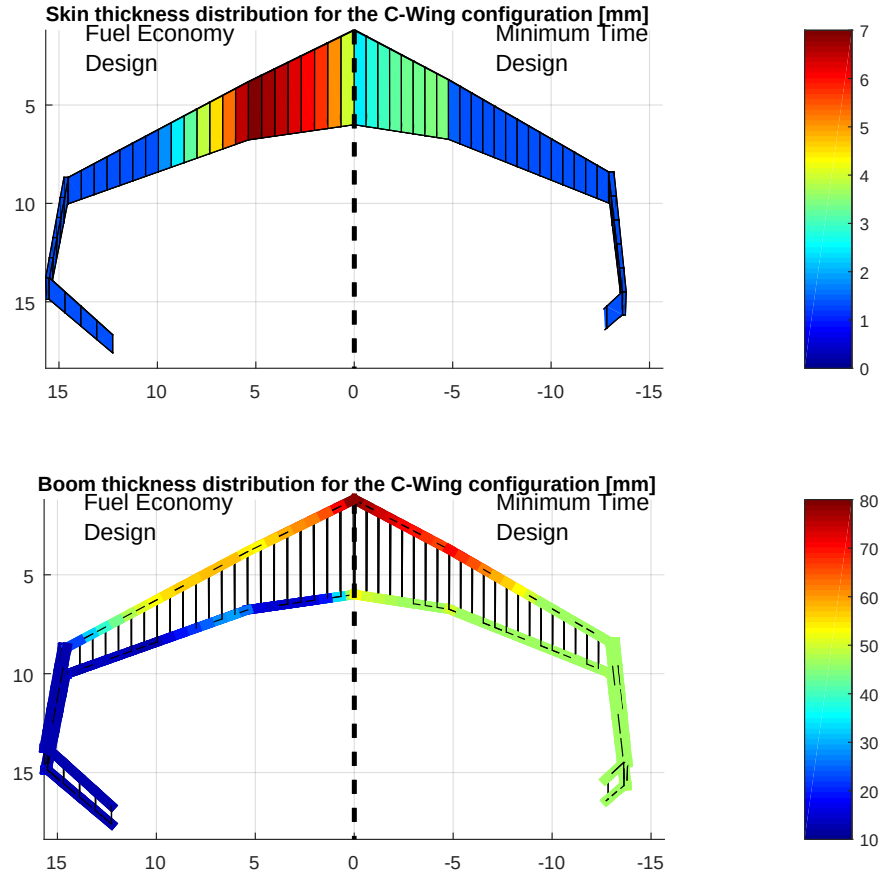

Figure 5.23: Optimal thickness distribution of the optimized C-wing configurations

By considering the lift coefficient distribution at cruise conditions, as given in figure 5.24, it can be seen that it is very comparable to the lift distribution of the winglet configurations: a higher lift coefficient towards the tip of the wing. Also, it can be seen that the fourth wing segment (the inward pointing surface) results in a negative lift contribution, as positive lift for this segment is pointing down. According to Kroo, this is favorable in terms of induced drag reduction as discussed in section 2.1 [51]. Although it is a small negative lift contribution, the total arm to the fuselage is large. This may provide a small bending relief. Figure 5.25 shows the $c \cdot c_l$ distribution of the C-wing designs. Again, the minimum time design distribution is higher at the root to compensate for the smaller wing span.

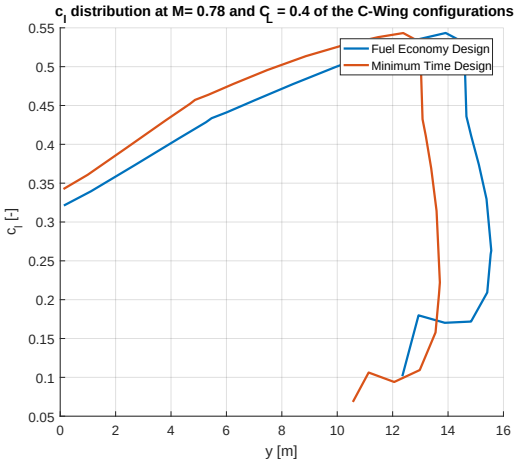

Figure 5.24: Lift coefficient distribution of the optimized C-wing configurations

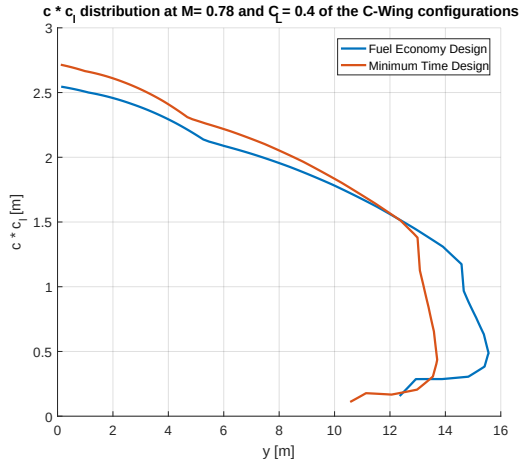

Figure 5.25: Lift distribution of the optimized C-wing configurations

Also for the optimized C-wing designs, the effect of the Mach number on the aerodynamic coefficients is analyzed. Figure 5.26 shows the drag components as function of Mach number. Also for the C-wing configuration, the induced drag is lower for the fuel economy design due to the longer wing span. The parasitic drag lines start to deviate from Mach 0.75. At higher Mach numbers, the fuel economy design shows a significant higher parasitic drag, which is mainly the results of the higher wave drag due to the smaller sweep angle. Equivalent to the winglet configuration, the minimum drag Mach numbers are 0.73 and 0.75 for the fuel economy design and the minimum time design respectively.

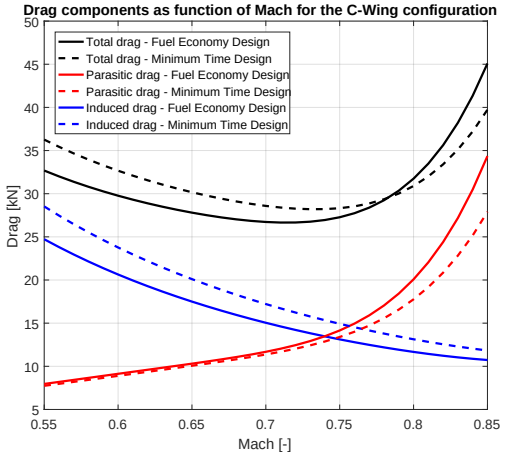

Figure 5.26: Drag components as function of Mach for optimized C-wing configurations

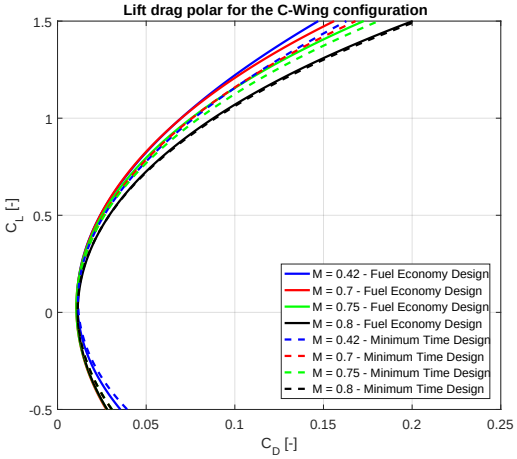

Figure 5.27: Lift drag polars as function of Mach for optimized C-wing configurations

Figure 5.27 shows the lift drag polars for a range of Mach numbers. For the C-wing configuration, the fuel economy design shows lower drag at Mach numbers below a Mach number of 0.78, which corresponds to the intersection of the two total drag curves in figure 5.26. At higher Mach numbers, the minimum time mission shows lower drag coefficients, especially at higher lift coefficients.

5.2.4. BOX-WING CONFIGURATION

Figure 5.28 shows the isometric view of the two optimized box wing designs. It can be seen that the wing span of both configurations is considerably smaller compared to the previous discussed configurations. To make a better comparison, these wing design are plotted on top of each other as shown in figure 5.29. According to the figure, the longitudinal position of the first wing segment of both wings is approximately equal. Also the

winglet segments are approximately the same height and not tapered. The main difference can be found in the wing span, which is 11.1% smaller for the minimum time design. More geometric characteristics of the two optimized designs can be found in table 5.6. Also, the Oswald factors in the cruise conditions are shown in the table. It can be seen that the minimum time configuration features a 0.9% higher Oswald factor. If these cruise Oswald factors are compared to those of the planar configuration, it can be seen that the box-wing configurations have an Oswald factor that is approximately 0.25 higher. It is remarkable to see that these Oswald factors are lower compared to the optimized C-wing configurations as discussed in the previous section. According too Kroo's theory as described in section 2.1, a box wing has the highest theoretical Oswald factor.

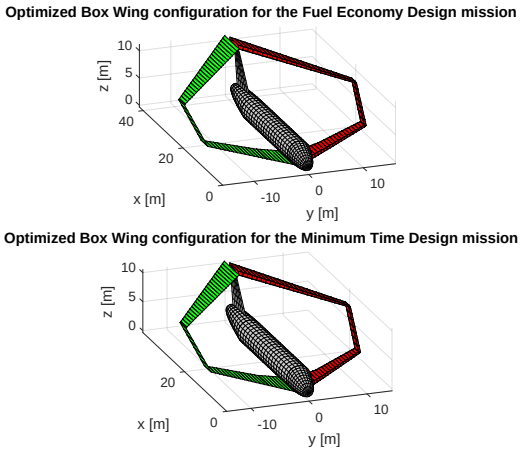

Figure 5.28: Optimized box wing configurations

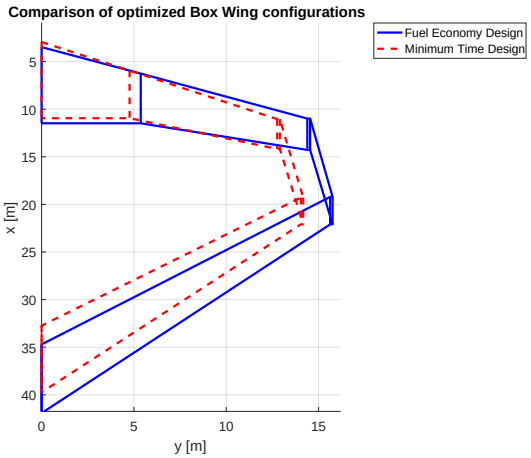

Figure 5.29: Comparison of the box wing designs

As can be seen in the table, the mass of the box wing is considerably lower compared to the previous configurations. Also, the difference between the two optimized box wings is 410kg, which equal 10.9% of the total wing weight. The difference in fuel consumption of both missions is 3%. The minimum time design is 15% faster.

Parameter	**Unit**	**Fuel economy**	**Minimum time**	**Difference [%]**
$F_{consumed}[kg]$	$[kg]$	2618.56	2702.99	-3.12
$t_{block}[min]$	$[min]$	54.30	47.20	15.04
M_{wing}	$[kg]$	4168.20	3758.40	10.90
S_{ref}	$[m^2]$	315.63	274.30	15.07
S_{wetted}	$[m^2]$	694.02	607.00	14.34
b_{ref}	$[m]$	31.80	28.61	11.15
AR	$[-]$	3.20	2.98	7.38
e_{cruise}	$[-]$	1.17	1.18	-0.85

Table 5.6: Mission and planform characteristics of the optimized box wing configurations

Figure 5.30 shows the thickness distribution of the skin and booms of the box wing designs. It can be seen that both the skins and booms are considerable thinner compared to previous configurations. This is the result of the two points at which it is attached to the fuselage. So although, the total wetted area of this configuration is larger, it allows for thinner skins and booms, and thus a lighter wing structure. If the two different optimized wing box designs are compared with each other, no significant changes can be found in the thickness distributions.

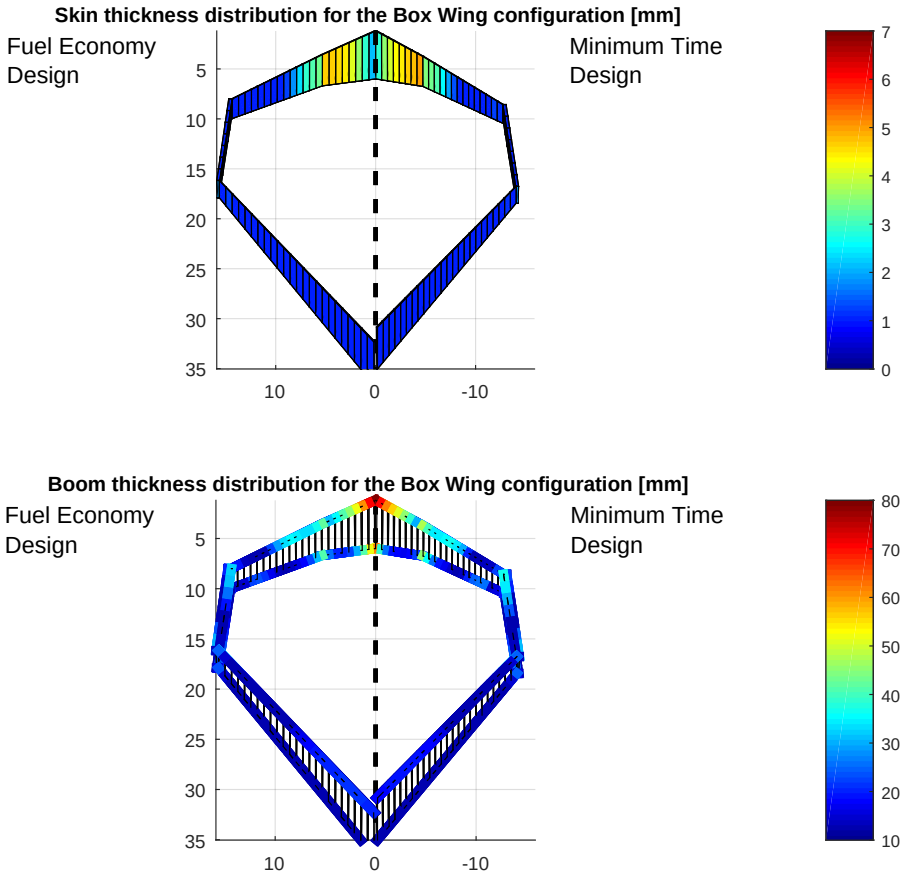

Figure 5.30: Optimal thickness distribution of the optimized box wing configurations

Figure 5.31 shows the lift coefficient distribution of the box wing designs. The negative lift coefficient as indicated in the figure, corresponds to the fourth wing segment. Because positive in this wing segment is defined as a downforce, this wing segment is in fact contributing with positive lift. Also, as discussed before, the aerodynamic lift distributions as presented in these figures are obtained at cruise conditions, i.e. a Mach number of 0.78 and where the lift equals the weight. Because the reference area of the box wing configurations is considerably larger, this results in a lower lift coefficient C_L of 0.19. If the two different optimized box wing designs are compared, it can be seen that the minimum time design has a higher sectional lift coefficient, both in the lower and upper wing.

Figure 5.32 shows the $c \cdot c_l$ distribution of the two optimized designs. Because the wing span of the minimum time design is smaller, a higher lift distribution is required to obtain equal lift. The largest differences in the lift distribution are located at the root of both the upper and lower wing.

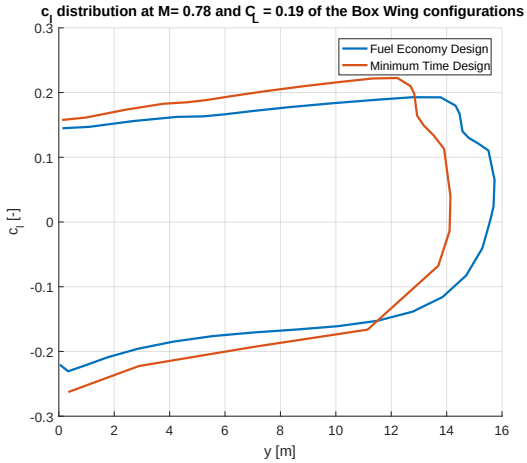

Figure 5.31: Lift coefficient distribution of the optimized box wing configurations

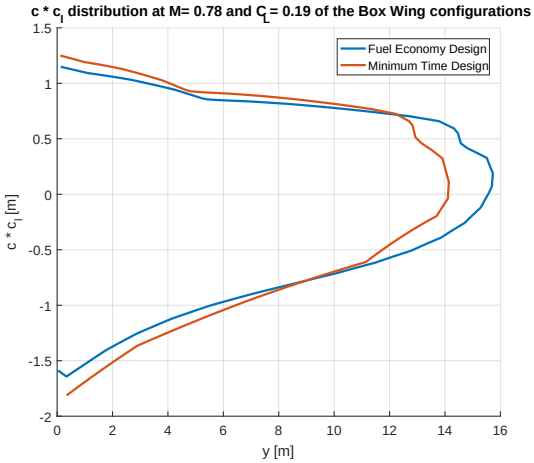

Figure 5.32: Lift distribution of the optimized box wing configurations

Also for the optimized box wing configurations, the effect of the Mach number on the aerodynamic coefficients is analyzed. Figure 5.33 shows the drag components as function of Mach number. The induced drag is lower over the entire Mach range for the fuel economy design due to the longer wing span. The parasitic drag is higher for the fuel economy design. At Mach numbers below 0.75, the two parasitic drag curves are parallel. In this Mach range, the parasitic drag of the fuel economy design is higher due to the larger wetted area compared to the minimum time design, which results in a higher friction drag. At Mach 0.75, the two curves start to deviate as result of higher wave drag for the fuel economy design. The minimum drag Mach numbers are 0.67 and 0.75 for the fuel economy design and the minimum time design respectively.

Figure 5.34 shows the lift drag polars for a range of Mach numbers. For the box wing configuration, the fuel economy design shows lower drag at Mach numbers below a Mach number of 0.76, which corresponds to the intersection of the two total drag curves in figure 5.33. At higher Mach numbers, the minimum time mission shows lower drag coefficients, especially at higher lift coefficients.

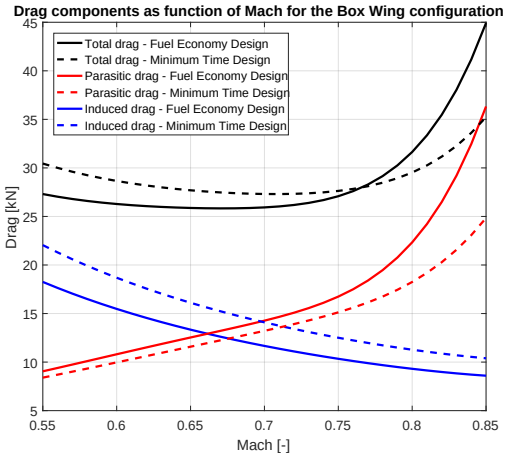

Figure 5.33: Drag components as function of Mach for optimized box wing configurations

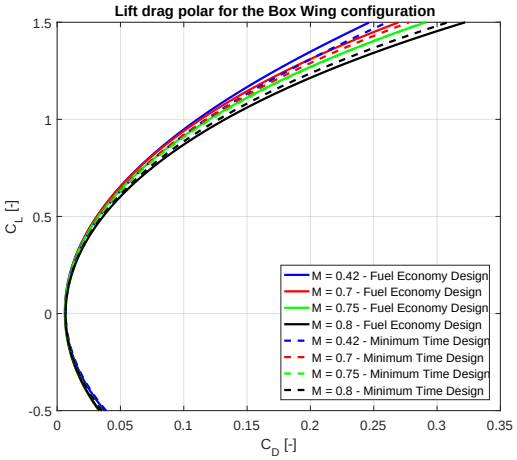

Figure 5.34: Lift drag polars as function of Mach for optimized box wing configurations

5.3. EFFECT OF NON-PLANAR WING SURFACES

This section describes the differences between the four optimized wing configurations. First, the configurations will be compared based on their total fuel consumption and their block time. Since these results are mainly affected by the weight of the wing and its aerodynamic properties, these two factors are discussed in more detail.

Figure 5.35 shows the total fuel consumption of the optimized designs for both mission profiles. The top figure shows the absolute fuel consumption. The bottom figure shows the fuel consumption of the non-planar configurations (wing with winglet, C-wing, and box wing) w.r.t. the planar configuration of the corresponding mission profile. From this figure can be concluded that both the winglet and the box-wing configuration can offer 1.5% to 2% fuel savings w.r.t. the planar configuration for both mission profiles. However, the C-wing configuration shows an increased fuel consumption in both missions. Finally, it can be seen that the box wing configuration performs slightly better compared to the winglet configuration in the fuel economy mission, while the winglet performs better in the minimum time mission. This is because the parasitic drag is relative more important in the minimum time mission due to the higher flight speeds. The winglet configuration has a smaller parasitic drag component compared to the box wing due to its smaller wetted area. Therefore this configuration performs better in the minimum time mission profile.

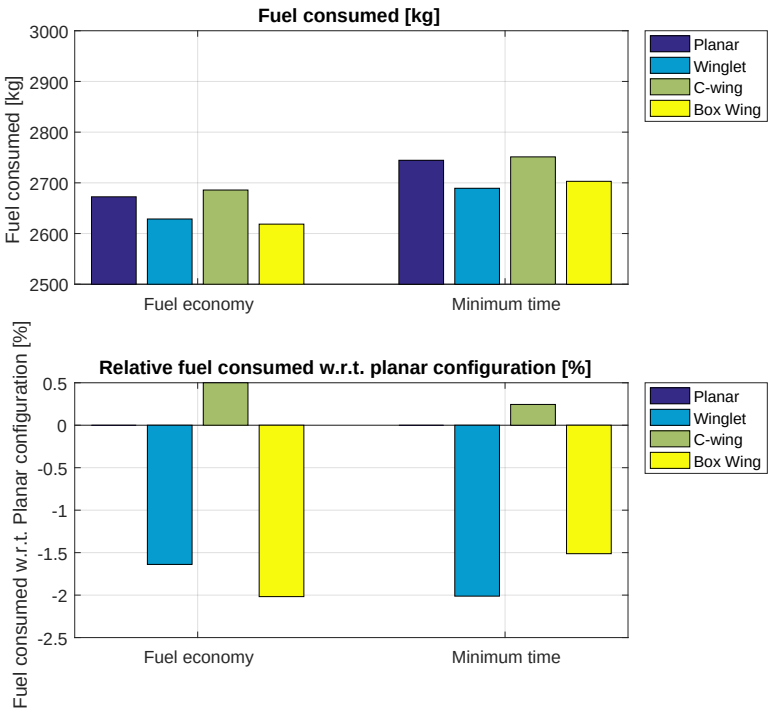

Figure 5.35: Absolute (top) and relative (bottom) comparison of the block fuel for both mission profiles

Figure 5.36 shows the block time for the various configurations. According to the figure, the largest savings in block time of 1.8% can be obtained for the fuel economy mission using a box wing configuration. For this mission profile, also the winglet configuration results in a 0.4% lower block time. For the minimum time mission profile, the differences in block time are significantly smaller. Because the mission profile is fixed, i.e. the flight speeds as function of altitude is fixed, these differences are the direct results of the differences in aircraft weight. Because the fuselage group weight remains constant in this study, only the wing mass affects this aircrafts weight. A lighter wing allows for a faster climb and therefore lower block times.

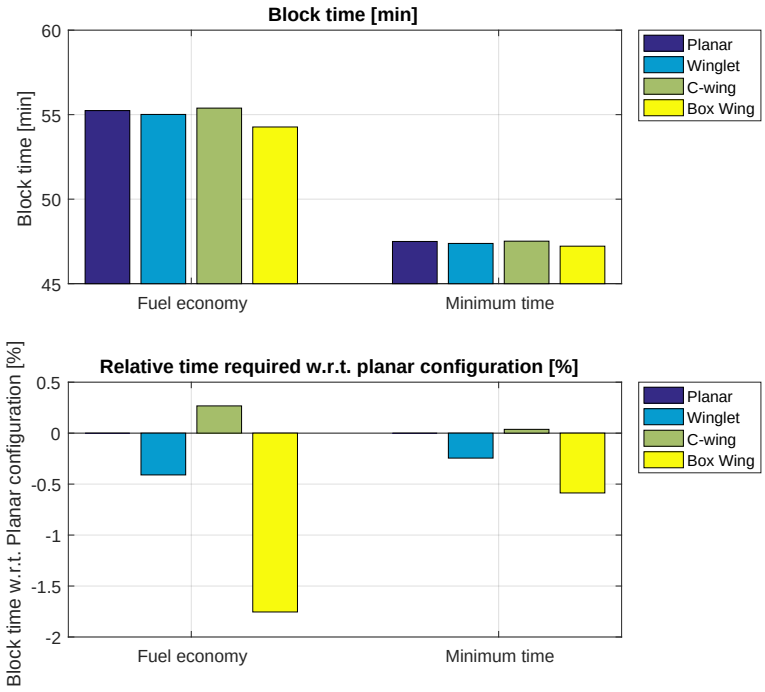

Figure 5.36: Absolute (top) and relative (bottom) comparison of the block time for both mission profiles

As mentioned above, the total fuel consumed during a mission mainly depends on the wing weight and the aerodynamic properties of the aircraft. Figure 5.37 compares the wing weights of the configurations. It is remarkable to see that all the configurations show a significant lower wing weight compared to the baseline A320 wing. The main reason is the lower wing span and lower aspect ratio of the wings. This allows for a stiffer wing structure, resulting in a lighter wing. By comparing the wing weight of the various configurations w.r.t. the planar designs, it can be seen that the winglet configuration allows for a weight reduction of approximately 10% for both mission profiles. The C-wing configuration requires a 25% and 7% heavier structure for the fuel economy design and minimum time design respectively. The box wing configuration offers with 40% the largest weight reduction of the considered configurations. As can be seen from figure 5.38, this configuration has the largest wetted area. However, the fact that it is attached to the fuselage at two points allows for a stiffer structure with thinner structural elements, resulting in a lighter wing.

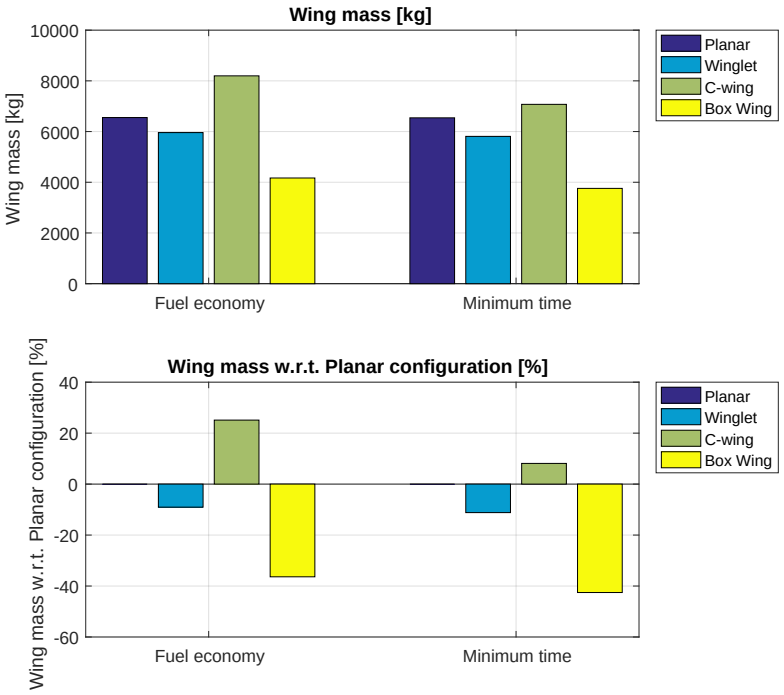

Figure 5.37: Absolute (top) and relative (bottom) comparison of the wing mass for both mission profiles

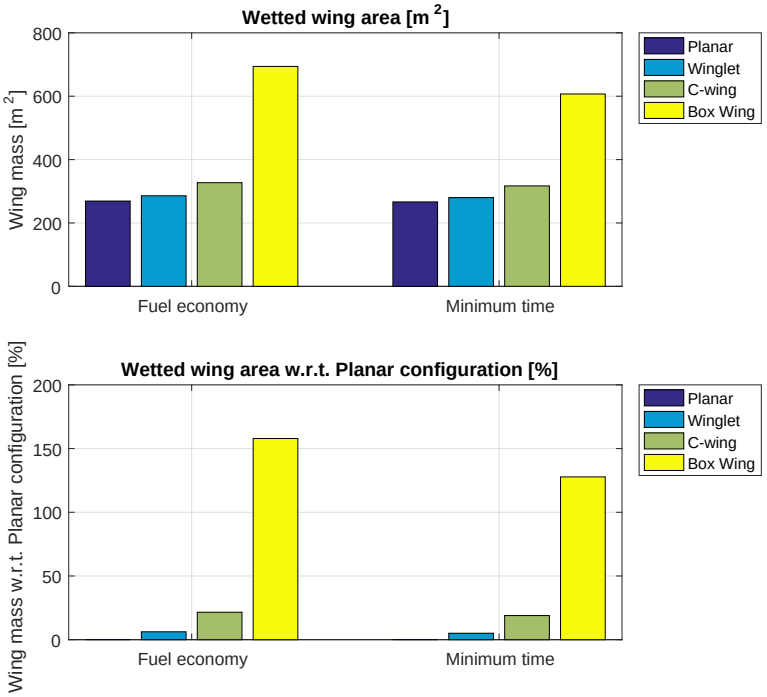

Figure 5.38: Absolute (top) and relative (bottom) comparison of the wetted wing area for both mission profiles

Figures 5.39 and 5.40 show the aerodynamic properties of the configurations during the mission for the fuel economy and minimum time mission profiles respectively. The values shown in these figures for the climb and descent phases, correspond to the values in the second EAS segments, i.e. mission segments 3 and 9 as defined in section 3.8. The three evaluated mission phases are evaluated at the points as indicated in the top figures respectively.

By comparing the aerodynamic properties of all the configurations between the two mission profiles, i.e. comparing the values in the two figures with each other, it can be seen that the main differences are found in the climb and descent segments of the mission. Because the flight speed in these mission segments is higher for the minimum time mission, a lower lift coefficient is required. Since the induced drag is quadratically proportional to the lift coefficient, this drag component is also smaller. The increasing flight speed would also result in an increase in parasitic drag according to figure 2.2. However, as discussed in the previous section, the wetted area of all the configurations is smaller for the minimum time mission, reducing the friction drag. This compensates for the increment in parasitic drag due to the increased flight speed, resulting in approximately equal parasitic drag between the two mission profiles.

By comparing the differences between the four wing configurations, i.e. comparing the values of the different configurations within the figures, it can be concluded that the three non-planar wing configurations offer a reduction in induced drag at the cost of an increment in parasitic drag. This effect is slightly more present for the C-wing configuration compared to the winglet configuration. For the box wing, this effect is quite strong, resulting in a induced drag reduction of approximately 25% at the cost of an large parasitic drag penalty. According to equation 2.1, the induced drag is a function of the lift, wing span, and Oswald factor. As concluded in section 5.2, both the wing span and Oswald factor of a box wing are smaller compared to the C-wing configuration which would result in a higher induced drag. However, the total lift to be produced by the configuration is lower due to the lower wing mass. Because this effect has a stronger effect on the induced drag than the lower wing span and Oswald factor, the resulting induced drag is lower.

Finally, it can be seen in figure 5.39 that the parasitic drag of the planar configuration for the fuel economy mission is remarkably high, while its wetted area is relatively small. This is the result of the smaller sweep angle, resulting in an increment in wave drag at transonic Mach numbers.

When the effect of the differences in drag components on the lift to drag L/D ratio is considered, it can be seen that all the three non-planar wing configurations perform relatively good in the cruise phase. Because the true airspeed in the cruise phase is lower, due to the constant Mach climb at which the true airspeed decreases, a higher lift coefficient is required to satisfy the equations of motion. Therefore the induced drag becomes relatively more important compared to the parasitic drag component. Because the non-planar configurations offer a lower induced drag, this results in a higher L/D ratio in the cruise phase.

The winglet and C-wing configuration can offer an increased L/D ratio in the cruise phase compared to the planar configuration. However, in the climb and descent phases the planar wing configuration performs better due to the relative larger parasitic drag component as described above. Flying the mission profiles with a box wing configuration has a detrimental effect of the L/D ratio, especially during the climb and decent phases. This is the result of the high penalty on the parasitic drag component.

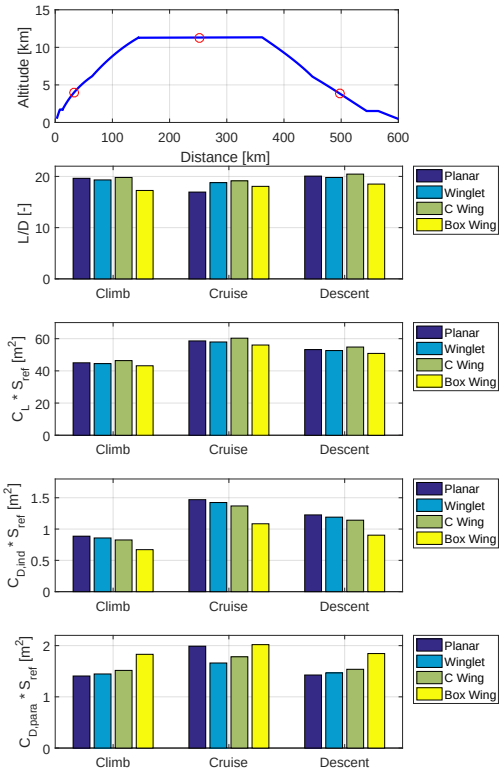

Figure 5.39: Comparison of the L/D ratio between the optimized configurations in the different mission phases for the fuel economy mission profile

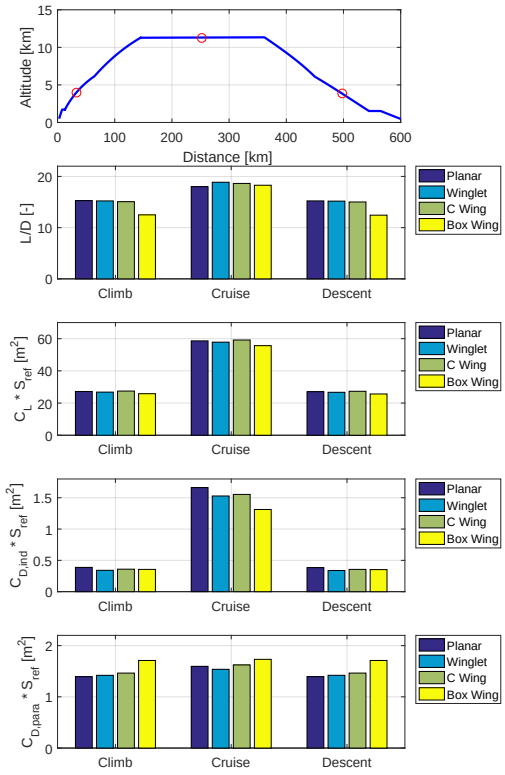

Figure 5.40: Comparison of the L/D ratio between the optimized configurations in the different mission phases for the minimum time mission profile

For the fuel economy mission, the Mach number in the climb and descent points, as evaluated in figure 5.39, equals 0.58. The Mach number of the evaluated cruise point equals 0.78. To provide a better insight in the aerodynamic properties of these fuel economy designs, their lift drag polars are compared at these two Mach numbers respectively, see figure 5.41. The points indicated by the circles correspond to the values as indicated in figure 5.39. At a Mach number of 0.58, the polars of the planar wing and wing with winglet are very comparable. The C-wing shows slightly higher drag at low lift, due to its higher friction drag. However, it shows lower drag at high lift due to the smaller induced dag, which becomes more important at high lift coefficients. The box wing design shows a higher drag at the entire range of considered lift coefficient. However, the differences between the drag of the box wing and the other designs reduce with increasing lift due to its lower induced drag.

The same effects are visible at the cruise Mach number: both the C-wing and box wing designs show relative high drag at low lift, and they become more efficient at high lift coefficients. However, in contrast to the climb and descent Mach number, the planar wing shows a higher drag over the entire range. This is the results of the increased wave drag due its the smaller sweep angle. Finally, from these figures can be concluded that the lower required lift of the box wing design, due to the smaller wing weight, results in lower drag, which partly compensates for its poor aerodynamic performance at low lift coefficients.

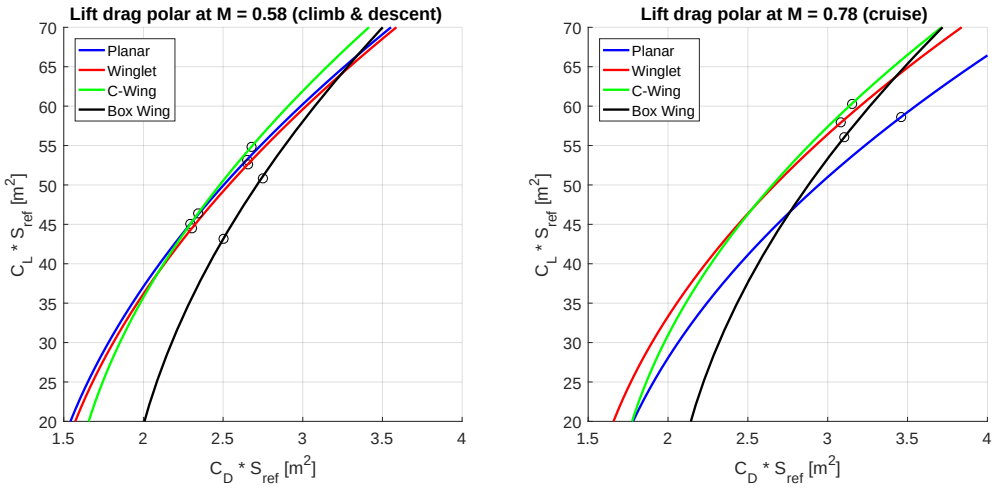

Figure 5.41: Lift drag polars for the fuel economy mission profile designs

For the minimum time mission, the Mach number in the climb and descent points, as evaluated in figure 5.40, equals 0.67. The Mach number of the evaluated cruise point equals 0.78. Also, the lift drag polars at these two Mach numbers are compared for the minimum time designs, see figure 5.42. The points indicated by the circles correspond to the values as indicated in figure 5.40. At a Mach number of 0.67, the polars of the planar wing, wing with winglet, and C-wing are very comparable. The box wing design shows a higher drag at the entire range of considered lift coefficient. However, the differences between the drag of the box wing and the other designs reduce with increasing lift due to its lower induced drag.

At the cruise Mach number, it can be seen that the polar for the planar wing deviates at higher lift coefficients due to an increased wave drag. Also from these figures can be concluded that the lower required lift of the box wing design, due to the smaller wing weight, results in lower drag, which partly compensates for its poor aerodynamic performance at low lift coefficients.

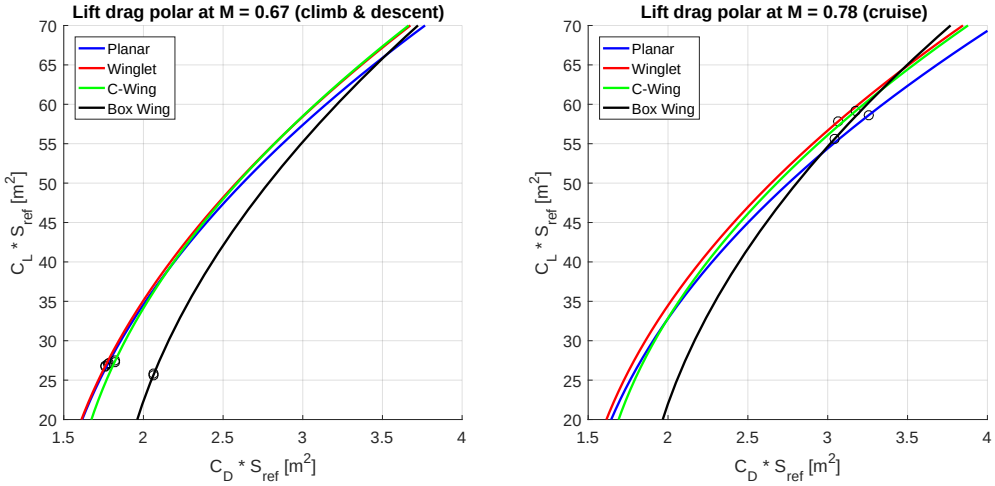

Figure 5.42: Lift drag polars for the minimum time mission profile designs

5.4. EFFECT OF CRUISE CONDITIONS ON THE EFFICIENCY OF NON-PLANAR WING CONFIGURATIONS

As concluded in the previous section, the three non-planar wing configurations offer a higher L/D coefficient in the cruise compared to the planar configuration, while in the climb and descent phases, this latter configuration performs relatively well. This would imply that the non-planar configurations become more efficient for longer mission, as the performance in the cruise phase becomes more dominant. This section discusses the effect of increasing the mission length on the block fuel of the configurations. In addition, the effect of the cruise Mach number is discussed.

In this analysis, the optimized designs for the mission range of 600km and a cruise Mach number of 0.78 are used to evaluate their performance in longer range mission, and mission with a different cruise Mach number. For this purpose, the fuel economy mission profile and its corresponding fuel economy designs are evaluated. Because the wing weight does not change with alternating the mission profile, the differences in fuel consumption are the result of the aerodynamic performance of the configurations.

Figure 5.43 shows the relative fuel consumption of the winglet, C-wing, and box-wing configurations w.r.t. the planar configuration for mission ranges from 600km to 2400km and cruise Mach numbers from Mach 0.66 to Mach 0.78. For all three non-planar configurations can be seen that increasing the mission range results in larger fuel savings compared to the planar wing. This is the direct result of the higher L/D in the cruise phase compared to the planar configuration.

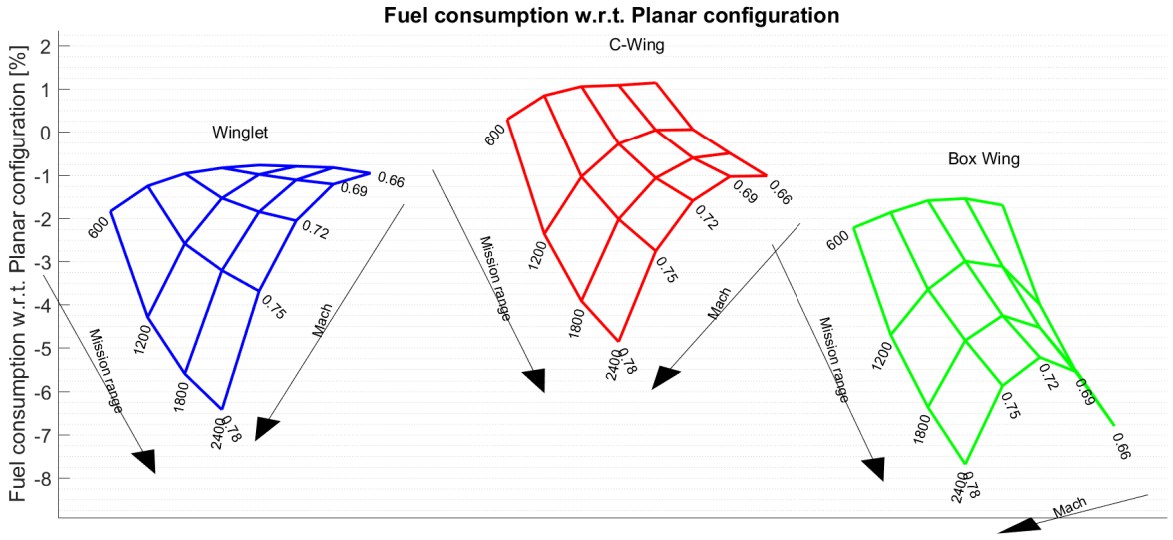

Figure 5.43: Carpet plot of the relative fuel consumption as function of the cruise length and cruise Mach number

However, by lowering the cruise Mach number up to a certain point, the non-planar configurations become relative less efficient. This may contradict the theory as discussed in section 2.1: because by lowering the Mach number, a higher lift coefficient is required to satisfy the equation of motions. Since the induced drag increases quadratically with the lift coefficient, this drag components increases with lowering the flight speed while the parasitic drag decreases. This would imply that the induced drag becomes more important, and so the non-planar configurations (which have a lower induced drag) are expected to perform better.

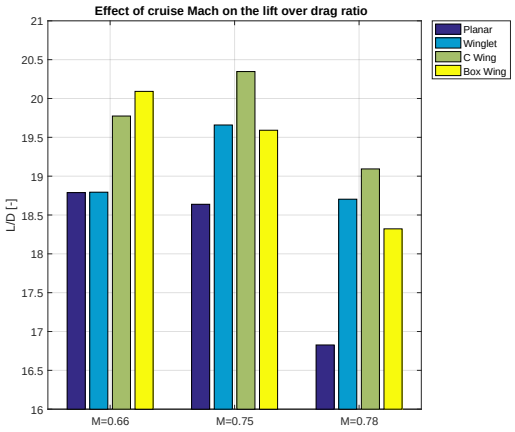

Figure 5.44: Lift over drag ratio as function of cruise Mach

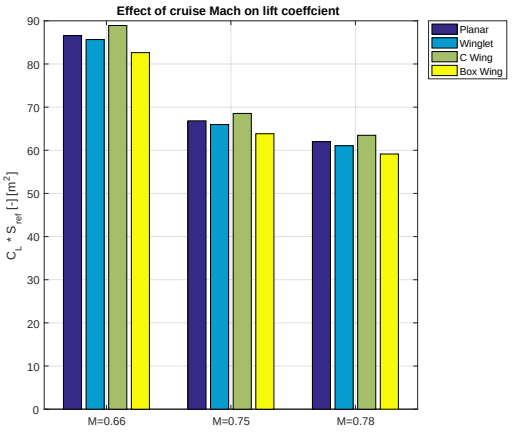

Figure 5.45: Lift coefficient as function of cruise Mach

In order to explain the relative lower efficiency of the non-planar configurations at these low cruise Mach number, a more detailed drag breakdown is given in figures 5.46 and 5.47. As can be seen in figure 5.46, the induced drag indeed increases with lowering the Mach number. When the parasitic drag component is considered, it can be seen that the friction drag remains approximately unaffected by changing the Mach number. However, the wave drag significantly reduces by lowering the cruise Mach number. This effect is the strongest for the planar configuration: reducing the cruise Mach number, results in a large reduction of the wave drag, and therefore a relative large reduction in the total parasitic drag component. This explains why the L/D ratio of the planar configurations increases relatively fast compared to the non-planar configurations.

Because the amount of wave drag strongly depends on the Mach number, the reduction in wave drag is the most significant at high Mach numbers. Further lowering the cruise Mach number has a smaller effect on the relative efficiency. This effect is also visible in the carpet plot: the lines connecting the higher Mach numbers are relatively steep, implying a fast decay in efficiency, and graduate flattens with lower Mach numbers. For the box wing configuration, this effect is also visible down to a cruise Mach number of 0.72. From this point on, further decreasing the cruise Mach number results in an improved relatively efficiency. From this point on, the effect of the increased induced drag, as mentioned above, becomes dominant over the effect of decreasing wave drag. Because the ratio between the induced and parasitic drag components is significantly different for the box wing configuration, this effect is already visible at the considered cruise Mach numbers. For the winglet and C-wing configurations, the same effect is expected for Mach numbers below 0.66.

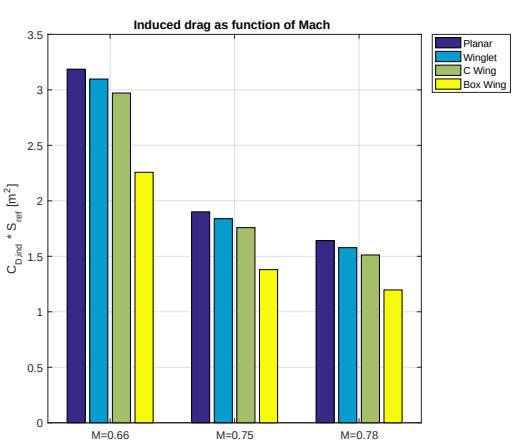

Figure 5.46: Induced drag as function of Mach

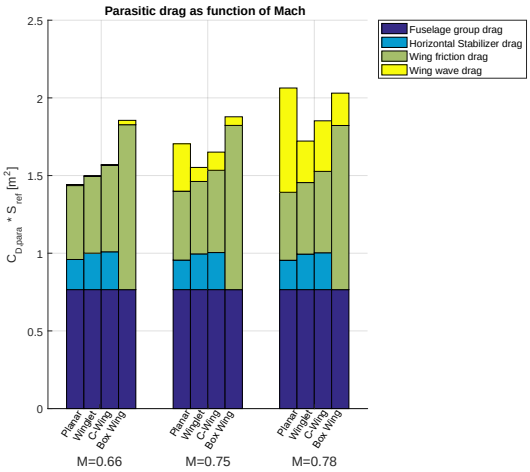

Figure 5.47: Parasitic drag as function of Mach

6

CONCLUSION

The goal of this study was to analyze and evaluate how a full mission analyses affects the fuel consumption of non-planar wing configurations, and which configurations are the most efficient in terms of fuel consumption. For this study, the Airbus A320-200 was used as a baseline aircraft. In order to study these effects, multidisciplinary design studies were performed. The created model consists of four validated modules: aerodynamics, structures, mission, and propulsion modules. Within these modules, the aspects studied in previous studies on the same subject were taken into account to create an accurate model. The developed model takes the aero-structural coupling into account, includes both the induced and parasitic drag components, and minimizes the structural weight at the critical conditions using an detailed finite element model of the wing box. In terms of optimization, a full non-linear constrained optimization study has been performed, in which four wing configurations were evaluated with high design freedom.

Based on the results of a 600km range mission optimization study using a fixed A320 wing planform, it can be concluded that the cost factor has a significant effect on the mission profile, even if the initial climb, cruise, and final decent phases remain unchanged. Based on the 600km mission, the difference in fuel consumption between the most fuel efficient and minimum flight time mission equals 7%, while the differences in block time are 15%. The fuel economy mission climbs and descends at lower airspeeds compared to the minimum time mission profile, therefore the induced drag becomes more important for the fuel economy mission. The largest profits in terms of fuel consumption are obtained due to the early and thus relatively long descent phase at which only a small amount of thrust is required.

The fuel economy and minimum time mission profiles are then used as input in several wing optimization studies. Four wing configurations - planar wing, C-wing, wing with winglet, and box wing - are optimized for the minimum block fuel. Based on the results it can be concluded that using a climb and descent profile with a different cost factor affects the most fuel efficient wing planform configurations. For all the four considered configurations, the minimum time designs shows a smaller wing span, smaller wetted area, and lower aspect ratio wing, which results in a lower wing weight. The difference in fuel consumption between the two mission profiles of the four configurations is around 3%, while the block time differences are approximately 15%.

Out of the four configurations, the winglet and box wing configurations have to highest potential to reduce the fuel consumption by 1.5% to 2% compared to the planar configurations. The C-wing shows a slightly higher fuel consumption. In terms of block time, the differences between the configurations is relative small. Only the box wing configurations shows a 1.5% lower block time for the fuel economy mission compared to the other configurations, due to its lighter wing. Because these two mission characteristics strongly depend on the wing mass and the aerodynamic performance of the aircraft, these aspects are studied in more detail.

By comparing the wing mass of the non-planar designs with the planar designs, it can be seen that the winglet design results in a 5% lower wing mass, the C-wing results in 10% to 25% higher wing mass, and the box wing offers, with a 40% savings, the largest reduction in wing mass. This is due to the lower wing span and increased stiffness because it is attached at the two points to the fuselage.

In terms of the lift over drag ratio, the non-planar configurations show no or very small beneficial effects in the climb and descent phases due to the low lift coefficient, and thus low induced drag, compared to the

planar configuration. However, in the cruise phase the winglet and C-wing configurations show a higher L/D ratio compared to the planar configuration. For the box-wing configuration, these values are more or less equal to the planar configuration. The main advantages of the winglet configuration lie in the slightly lower wing mass combined wing the higher L/D ratio in the cruise phase. The C-wing configuration results in a higher wing mass, but this is partly compensated for due to its higher L/D ratio. For the box wing, this effect is the other way around: it has a detrimental effect on the L/D ratio, especially in the climb and descent phases of a mission. However, the structural weight savings make up for this loss, therefore, when considering the fuel consumption over the entire mission, this configuration performs the best.

Finally, the effect of varying the mission range and cruise Mach number is studied. The fuel consumption of the three optimized non-planar designs is compared to that of the optimized planar design for the fuel economy mission profile. From these results can be concluded that all the non-planar configurations become more efficient with increasing mission length. This is the direct result of the higher L/D ratio in the cruise phase, which becomes more dominant for longer missions. In addition, it is concluded that by lowering the cruise Mach number up to a specific point, the planar configuration becomes more efficient in terms of fuel consumption. This is due to the fast decrease of the wave drag for the planar configuration, while for the non-planar configurations this effect is smaller due to the smaller total amount of wave drag. Further decreasing the Mach number, results in an increased fuel efficiency of the non-planar configurations. This is the direct result of the ratio between the induced and parasitic drag components. Flying at a lower Mach number, results in a higher required lift coefficient, and therefore a higher induced drag. Therefore this drag ratio shifts towards the induced drag, which is lower for the non-planar configurations.

In conclusion, multidisciplinary design optimizations were performed with more accurate and advanced models compared to previous studies on this subject. The results give a good insight into how altering the low speed mission segments affect the most optimal wing design. The results of this study also provide an insight into the structural and aerodynamic performance of the planar, winglet, C-wing, and box wing configurations. From this study, can be concluded that using different climb and descent strategies results in different optimal wing planforms in terms of fuel consumption, therefore it is important to take these low speed mission segments into account when optimizing wing configurations - especially for short range missions.

7

RECOMMENDATIONS

Althrough the current the model tries to model the real acircaft behviour as realistic as possible, it is still limited on several aspects. This chapter discusses the recommendations for future research on this subject.

The developed model does not take aeroelastic effects into account. The aerodynamic charachteristics are determined for the rig shape of the wing. However, the wing will deform under the aerodynamic loads during the flight. This in turn affects the aerodynamic performance of the wing. Because the different wing configurations may show different aeroelastic effects, incorporating this coupling between the aerodynamic module and the structure module may lead to alternate results. Especially the box wing is expected to show different aeroelastic behaviour due to its stiffer wing structure at is attached at two points on the fuselage.

As critical load condition for the structural module, the 2.5g load condition is taken as specified in the CS25 regulations. However, also the -1g load case at landing conditions may affect the optimized wing box, and thereby affect the wing weight. In the current model this -1g load condition is not taken into account. Also, the structural model used in this study consists of boom and skin elements. The accuracy of the structural model can be improved by adding ribs and stringers in the Nastran model.

The fuselage group is modelled as a constant factor in the present model. However, changing the wing configurations will also affect the fuselage design, especially for the box wing configuration. Also, an actual aircraft is the result of a converged design. Changing the wing planform and location will also affect other components in of the aircraft, i.e. the location of the landing gear is affected. Taking these factors into account will give a better representation of the actual aircraft.

The stability and controlabillity of the configurations is only constraint for the longitudinal and static cases. It may be interesting to see how the different configurations perform under dyanmic stability constraints, i.e. how the eigenmodes of the aircraft changes. Also the lateral performance is not considered in the actual model. Including this in the mission analysis may also affect the optimized wing planforms.

Finally, it is recommended to use a non-gradient based optimizer to prevent local minima. The model is created to allow design high freedom, however due to the nature of the gradient based optimizer it may not be able to explore the full design space.

BIBLIOGRAPHY

[1] ICAO Secretariat. Icao environmental report, 2010. Accessed August 2013.

[2] International Energy Agency (IEA). World energy outlook. 2008.

[3] Air Transport Action Group. A sustainable flight path towards reducing emissions. 2012.

[4] P.W. Jansen, R.E. Perez, and J.R.R.A. Martins. Aerostructural optimization of nonplanar lifting surfaces. Sep 2010.

[5] S.N. Skinner and H. Zare-Betash. Aerodynamic optimisation of non-planar lifting surfaces. In *57th AIAA/ASCE/AHS/ASC Structures, Structural Dynamics, and Materials Conference*. American Institute of Aeronautics and Astronautics (AIAA), Jan 2016.

[6] P.W. Jansen. Aerostructural optimization of nonplanar lifting surfaces. Master's thesis, University of Toronto, 2009.

[7] R.P. Liem, G.K.W. Kenway, and J.R.R.A. Martins. Multimission aircraft fuel-burn minimization via multipoint aerostructural optimization. Jan 2015.

[8] R.P. Liem, C.A. Mader, E. Lee, and J.R.R.A. Martins. Aerostructural design optimization of a 100-passenger regional jet with surrogate-based mission analysis. Aug 2013.

[9] J.Y. Kao, J.T. Hwang, J.R.R.A. Martins, J.S. Gray, and K.T. Moore. A modular adjoint approach to aircraft mission analysis and optimization. In *56th AIAA/ASCE/AHS/ASC Structures, Structural Dynamics, and Materials Conference*, 2010.

[10] I. Kroo. Nonplanar wing concepts for increased aircraft efficiency. 2005.

[11] I. Kroo. Drag due to lift: Concepts for prediction and reduction. Technical report, Department of Aeronautics and Astronautics, Stanford University, Stanford, 2001.

[12] FAA. Part 25: Airworthiness standards. Technical report, FAA, 2016.

[13] J.G. Verstraeten and R. Slingerland. Drag characteristics for optimally span-loaded planar, winglетted, and c wings. May 2009.

[14] S.A. Ning and I. Kroo. Multidisciplinary considerations in the design of wings and wing tip devices. Mar 2010.

[15] O. Gur, W.H. Mason, and J.A. Schetz. Full configuration drag estimation. In *27th AIAA Applied Aerodynamics Conference*, 2009.

[16] Anonymous. Aircraft performance. http://ocw.mit.edu/ans7870/16/16.unified/propulsionS04/ UnifiedPropulsion4/UnifiedPropulsion4.htm. Accessed: 11-04-2016.

[17] R. Vos and S. Farokhi. *Introduction to Transonic Aerodynamics*. Springer Dordrecht Heidelberg New York London, 2015.

[18] Anonymous. Lifting line theory. http://www2.esm.vt.edu/dtmook/AOE5104_ONLINE/ClassNotes/23_Class_LLT.pdf. Accessed: 11-04-2016.

[19] F.H.W. Baer. Drag. http://www.woseba.de/03_drag.html. Accessed: 11-04-2016.

[20] M.M. Munk. The minimum induced drag of aerofoils. Technical report, National Advisory Committee for Aeronautics, 1921.

[21] J.M.Riebe and J.M. Watson. The effect of end plates on swept wings at low speed. Technical report, NACA, 1950.

[22] F.A. Khan. Preliminary aerodynamic investigation of box-wing configurations using low fiselity codes. Master's thesis, 2010.

[23] L. Prandtl. Induced drag of multiplanes. Technical report, National Advisory Committee for Aeronautics, 1924.

[24] A. Frediani. The prandtl wing. 2005.

[25] P.D. Gall. An experimental and theoretical analysis of the aerodynamic charateristics of a biplane-winglet configuration. 1984.

[26] P.W. Jansen and R.E. Perez. Effect of size and mission requirements on the design optimization of non-planar aircraft configurations. In *13th AIAA/ISSMO Multidisciplinary Analysis Optimization Conference*, 2010.

[27] D. Simos. Piano-x. http://www.piano.aero/. Accessed: 13-04-2016.

[28] Dr.ir. G. La Rocca. Aerospace design and systems engineering elements ii, 2012.

[29] L. Jenkinson, P. Simpkin, and D. Rhodes. Civil jet aircraft design - airbus aircraft. Accessed: 28-04-2016.

[30] A.A. Trani. Air transportation systems analysis. Virginia Tech - Lecture Slides, 2014.

[31] R. Babikian. The historical fuel efficiency characteristics of regional aircraft from technological, operational, and cost perspectives. Master's thesis, 2001.

[32] CFM International. Cfm56-5b turbofan engine. http://www.cfmaeroengines.com/engines/cfm56-5b. Accessed: 24-04-2016.

[33] Airbus. Aircraft characteristics airport and maintenance planning. Technical report, 2015.

[34] E. Torenbeek. Cruise performance and range prediction reconsidered. 1996.

[35] Eurocontrol. Lto fuel and emissions calculator - tfeip, 2017.

[36] S.A. Andrews, R.E. Perez, and D. Wowk. Wing weight model for conceptual design of nonplanar configurations. Jun 2015.

[37] M. Drela. Xfoil - subsonic airfoil development system. http://web.mit.edu/drela/Public/web/xfoil/. Accessed: 12-04-2016.

[38] A. Elham. *Weight indexing for Multidiciplinairy Design Optimization of Lifting Surfaces.* PhD thesis, TU Delft, 2013.

[39] IHS ESDU. Vgk method for two-dimensional aerofoil sections. Accessed: 12-04-2016.

[40] M. Drela. Mses. http://raphael.mit.edu/research.html. Accessed: 12-04-2016.

[41] MSC Software. Msc nastran - multidisciplinary structural analysis. Accessed: 13-04-2016.

[42] ASM Aerospace Specification Metals Inc. Aluminum 7075-t6; 7075-t651, 2017.

[43] S.A. Andrews and R.E. Perez. Parametric study of box-wing aerodynamics for minimum drag under stability and maneuverability constraints. Jun 2015.

[44] D. Howe and G. Rorie. *Aircraft conceptual design synthesis.* Professional Engineering Pub., 2000.

[45] Netherlands Aerospace Centre. Gsp - gas turbine simulation program. http://www.gspteam.com/. Accessed: 22-04-2016.

[46] European Aviation Safety Agency. Easa type-certificate data sheet. Technical report, EASA, 2008.

[47] M. Voskuijl. Flight and orbital mechanics - unsteady climb. TU Delft - Lecture Slides, 2012.

[48] Airbus Customer Service. Getting to grips with aircraft performance. Technical report, Airbus, 2002.

[49] X. Zhao, W.J.C. Verhagen, and R. Curran. Aircraft bi-level life cycle cost estimation. 2015.

[50] International Civil Aviation Organization. Annex 16 - environmental protection volume ii aircraft engine emissions. Technical report, ICAO, 2008.

[51] I. Kroo, J. McMasters, and S.C. Smith. Highly nonplanar lifting systems. Technical report, NASA, 1995.

[52] C.N. Zohlandt. Conceptual design of high subsonic prandtl planes. Master's thesis, TU Delft, 2016.